CONCEPTUAL MODELING AND ANALYSIS OF DRAG-AUGMENTED SUPERSONIC RETROPROPULSION FOR APPLICATION IN MARS ENTRY, DESCENT, AND LANDING VEHICLES

by

Michael A. Skeen

A thesis submitted to the

Faculty of the Graduate School of the

University of Colorado in partial fulfillment

of the requirement for the degree of

Master of Science

Department of Aerospace Engineering Sciences

2013

This thesis entitled:

Conceptual Modeling and Analysis of Drag-Augmented Supersonic Retropropulsion for Application in Mars Entry, Descent, and Landing Vehicles

written by Michael Anthony Skeen
has been approved for the Department Aerospace Engineering Sciences

_____

Dr. Ryan P. Starkey

_____

Dr. Kenneth E. Jansen

_____

Dr. David M. Klaus

Date_____

The final copy of this thesis has been examined by the signatories, and we
Find that both the content and the form meet acceptable presentation standards
Of scholarly work in the above mentioned discipline.

ABSTRACT

Skeen, Michael Anthony (M.S., Department of Aerospace Engineering Sciences)

Conceptual Modeling and Analysis of Drag-Augmented Supersonic Retropropulsion for Application in Mars Entry, Descent, and Landing Vehicles

Thesis Directed by Assistant Professor Ryan P. Starkey

The development of new decelerator technologies will be required as the desired payload mass for future Mars landing missions increases beyond the current state-of-the-art architecture capability. This thesis examines the potential for supersonic retropropulsion applied on entry, descent, and landing vehicles to increase the landed payload mass. Supersonic retropropulsion systems use rocket thrust directed into the free stream flow to decelerate the vehicle during descent. Under certain conditions the aerodynamic drag on the entry vehicle can be preserved or augmented using supersonic retropropulsion.

The development of a model characterizing the drag augmentation capabilities of supersonic retropropulsion flow interactions is described. The model combines results from computational fluid dynamic simulations available in literature and analytic techniques to estimate the drag coefficient of a 70° sphere-cone aeroshell. The model is designed to capture the dominant flow physics of pressure conservation through various shock cascade structures more quickly than computational fluid dynamic simulations. This allows conceptual systems analysis to be performed across a wide range of input values beyond the current parameter space evaluated in experiments or computational simulations. The drag coefficient model developed is validated against available results from wind tunnel tests and computational

simulations to within 10%. In addition, the sensitivity of the computed drag coefficient to inputs estimated from computational simulation results in literature is analyzed.

A study of drag-augmented supersonic retropropulsion operation concepts for use in Mars entry, descent, and landing is presented. The feasible entry and payload masses for ballistic entries are determined for a range of supersonic retropropulsion operation intervals to illustrate the flight regimes where supersonic retropropulsion is most effective. The use of supersonic retropropulsion is shown to reduce the required propellant mass by 65% when the operation interval is focused in the region of maximum dynamic pressure. In addition, the feasibility of two concepts combining supersonic decelerator concepts is investigated: a combination of drag-augmented and high-thrust supersonic retropropulsion, and a combination of drag-augmented supersonic retropropulsion and inflatable aerodynamic decelerators. The potential for these hybrid solutions to increase the payload mass capability by up to 708% using each technology in the appropriate flight regime is demonstrated.

ACKNOWLEDGEMENTS

There are countless people who have aided me throughout my time at the University of Colorado at Boulder. I would like to thank Dr. Ryan Starkey for his consistently prudent guidance. Dr. Starkey has provided invaluable guidance in selecting and researching my topic. He has always steered me towards practical solutions and aided in clarifying complex problems. Dr. Starkey's has gone to great lengths to support me in my academic and professional career, as he does with all his students. I am exceptionally grateful for Dr. Starkey's mentorship.

I also thank my other committee members, Dr. David Klaus and Dr. Kenneth Jansen, for their feedback and advice. I have enjoyed spending time with Dr. Klaus teaching ASEN 2004 and many enlightening discussions on the engineering design process. I have appreciated Dr. Jansen's courses for their rigor in approaching the complex world of fluid mechanics. Thank you both for your insight into solving challenging engineering problems.

I would also like to thank the Aerospace Engineering Sciences department for providing funding assistance during my graduate studies through the Course Assistant and Teaching Assistant programs.

I thank the many friends, classmates, and coworkers whom I have worked with over the past 5 years. I have truly enjoyed their companionship, both in and out of the classroom. I have been lucky to work with some extraordinarily talented people, and I have learned as much from them as from any class. Finally, I cannot thank my family enough for their unflinching support and encouragement in helping me achieve my goals.

TABLE OF CONTENTS

LIST OF TABLES

LIST OF FIGURES

ACRONYMS AND NOMENCLATURE

CFD = Computational Fluid Dynamics

CO_2 = Carbon dioxide

DOF = Degrees of Freedom

EDL = Entry, Descent, and Landing

GRAM = Global Reference Atmospheric Model

IAD = Inflatable Aerodynamic Decelerator

MSL = Mars Science Laboratory

NASA = National Aeronautics and Space Administration

NS = Normal Shock

ONS = Oblique-Normal Shock cascade

OONS = Oblique-Oblique-Normal Shock cascade

SRP = Supersonic Retropropulsion

A = area (m^2)

β = ballistic coefficient (kg/m^2)

β_w = shock wave angle (deg)

C_D = drag coefficient

C_p = coefficient of pressure

C_T = thrust coefficient

γ = specific heat ratio

γ_f = fight path angle

D = drag force (N)

e = exponential function

F_A = axial force (N)

F_N = normal force (N)

g = local gravitational acceleration (m/s^2)

g_0 = gravitational acceleration at Earth's surface, 9.81 m/s^2

h = altitude (km)

∞ = free stream property

I_{sp} = specific impulse (sec)

M = Mach number

m = mass (kg)

μ = gravitational parameter (km^3/s^2)

P = pressure (Pa)

q = dynamic pressure (Pa)

R = radius (km)

ρ = density (kg/m^3)

s = arc length

T = temperature (K)

t = time (sec)

Th = thrust force (N)

θ = local azimuth angle (deg)

θ_d = flow deflection angle (deg)

V = velocity (m/s)

1 INTRODUCTION

1.1 Mars Entry, Descent, and Landing Overview

The series of maneuvers and events required to land a vehicle on a planet is referred to as entry, descent, and landing (EDL). The performance of the EDL system is focused in two areas: the amount of payload mass that can be landed and how accurately the payload can be landed at a given location. The duration of the EDL sequence for Mars landing vehicles historically lasts on the order of minutes. A sample progression of EDL events from the Mars Science Laboratory mission [1] is provided below in Figure 1.1.

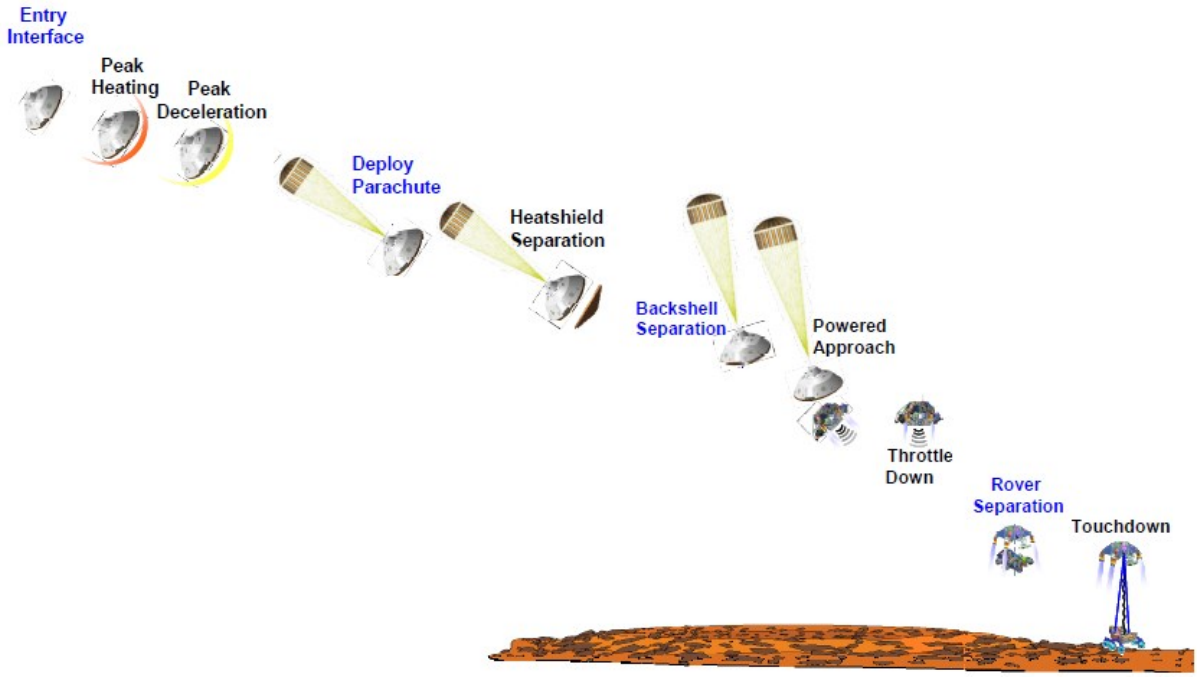

Figure 1.1: Mars Science Laboratory EDL sequence (adapted from Ref. [1])

Atmospheric entry is defined as an initial set of conditions where the vehicle enters the planet's atmosphere. Typically, the entry altitude for Mars EDL is approximately 120 km,

where the atmospheric density is nearly negligible. The vehicle has a flight path angle below the horizon, and is travelling hypersonically (on the order of 5-8 km/s with Mach numbers up to 30).

As the vehicle descends and the atmosphere thickens, the drag on the vehicle increases, slowing it until the parachute can be deployed. During descent, the compression of the oncoming flow on front of the vehicle's leading face causes significant aerodynamic heating. A heat shield is required to protect the vehicle's payload from the high peak heating rate as well as the large total heat load over the flight duration. Some vehicles have maneuvering capability during this phase to more accurately target the landing site using lift generated by varying the vehicle's angle of attack. The entry and descent phases for Mars vehicles are conceptually similar to the entry and descent phases of Earth re-entry vehicles, such as the Apollo capsule or the Space Shuttle.

In the landing phase, the vehicle performs final maneuvers to reach its landing site and reduces its speed to safely touch down on the surface. The landing systems for EDL vehicles have varied widely based on mission requirements. Mars landers have all used subsonic retrorockets for final maneuvering to the landing site. Some vehicles continued to use retrorockets for flight control all the way to the surface, while other missions used airbags to protect the payload during the landing impact.

1.2 Mars Entry, Descent, and Landing History

Atmospheric entry system development originated in ballistic missile programs during the Cold War. However, these designs were slender bodies focused on descending through the atmosphere quickly to avoid defensive countermeasures. When the USA and Soviet Union began developing orbital spacecraft, new re-entry systems had to be developed to slow

the payload for a safe landing. These vehicles dissipated their kinetic energy through the use of blunt geometries resulting in high drag and heat dissipation on the body. The Soviet Vostok spacecraft employed a spherical re-entry capsule and the American Mercury spacecraft (followed by the Gemini and Apollo spacecraft) featured a truncated cone shaped vehicle capped with a spherical heat shield. All of these vehicles (both manned and unmanned) utilized ablative heat shields. Ablative heat shields increase the total heat load a vehicle can survive by pyrolysis of the heat shield materials. As the heat shield layers pyrolyze, they carry away high amounts of thermal energy to reduce the heat soak through the heat shield and into the vehicle. The pyrolysis gases also inject cooler gases into the boundary layer, reducing the heat flux incident on the heat shield face.

1.2.1 Early Mars Landing Systems

The first attempted landing of a vehicle on Mars' surface was the Soviet Mars 2 spacecraft in 1971, which resulted in a crash landing. The Mars 3 spacecraft landed softly on Mars shortly thereafter, but stopped communicating 20 seconds after landing. The Mars 2 and 3 spacecraft featured orbital spacecraft with an attached lander. The landers, shown in Figure 1.2, had a mass of approximately 1,210 kg, with the 1.2 m diameter spherical lander weighing 368 kg. The Mars 6 and Mars 7 missions also unsuccessfully

Figure 1.2: Mockup of the Soviet Mars 2 lander [2]

attempted landing on the Martian surface. Mars 6 is thought to have landed at too large a speed, destroying the lander. The Mars 7 lander was released early from the orbiter and missed the entry interface.

The first US lander to reach Mars was Viking 1, landing in 1976. It was followed shortly thereafter by the Viking 2 mission. Both vehicles landed successfully and operated on the surface for several Martian years. The Viking landers utilized ablative heat shields to slow the vehicles until supersonic disk-gap band parachutes could be deployed. The vehicle then used retrorockets to slow itself for a soft landing. Viking was passively controlled on descent, resulting in large uncertainties in landing location.

Figure 1.3: Viking lander mockup [3]

The heat shield used for the Viking missions was not spherical like those of the manned Earth re-entry missions. Instead a 70° cone with a blunted spherical nose was used to increase the drag coefficient to compensate for the relatively thinner atmosphere of Mars.

1.2.2 Advances in Mars Entry, Descent, and Landing Technologies

The following lander missions attempted by the US have used the same vehicle architecture as the Viking missions. This design choice is often driven by the need to minimize cost coupled with the fact that the Viking architecture has been successful in landing the small payload masses considered. The only variations in US Mars landers have

been in the design of the final landing system, which completes the subsonic portion of flight. The supersonic and hypersonic technologies have remained fundamentally unchanged dating back to the 1970's. The Mars Pathfinder (MPF) and Mars Exploration Rover (MER) missions used a smaller diameter heat shield with the same geometry and materials as Viking with the same parachute. However, the retrorockets were replaced with an airbag system providing 4π steradian protection for landing orientation. The Phoenix mission used the same size heat shield as MPF and MER. The aeroshell designs for all U.S. Mars landers are compared in Figure 1.4.

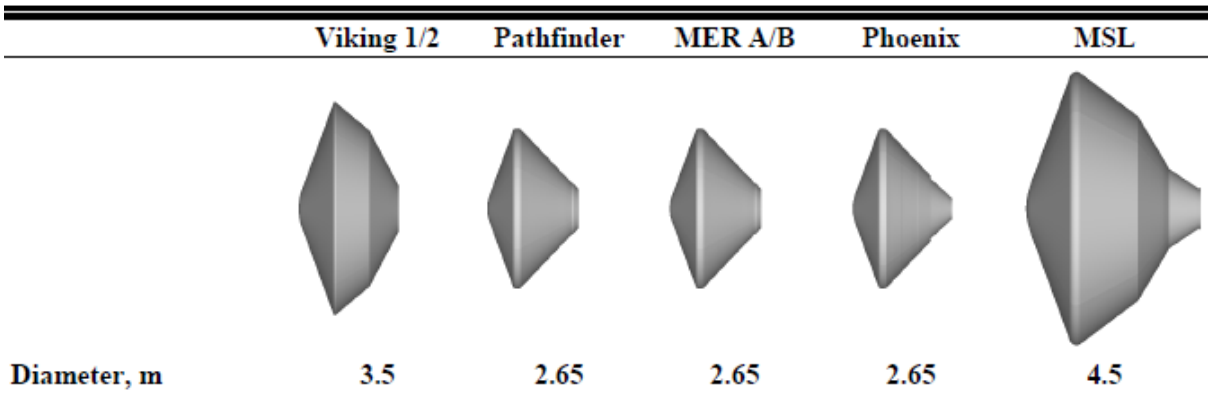

Figure 1.4: Comparison of US aeroshells used in Mars landings [4]

The Mars Science Laboratory (MSL) mission landed on Mars in August of 2012. It landed a much heavier mass on the planet's surface than any previous vehicle. The heat shield was the largest ever used but still used the same 70° sphere-cone geometry and supersonic disk-gap band parachutes as the Viking landers. Active control was added to the hypersonic phase with small hydrazine thrusters to reduce the landing uncertainty ellipse. A new landing system, the 'Skycrane' was used to allow higher throttling of the landing engines at the surface while protecting the Curiosity rover from damage caused by the plume exhaust shooting rocks at the vehicle. This landing system has enabled higher mass payloads

to be landed safely. However, the declarative technologies used in the entry and descent phases are qualitatively the same as the Viking landers, developed some 30 years prior.

1.2.3 Summary of Past Mars Landing Vehicles

Table 1.1 summarizes the design and performance of the past EDL vehicles successfully landed on Mars by the U.S. Data is sourced from references [1, 5, 6, 7, 8, 9].

Table 1.1: Past U.S. Mars landing vehicles [6]

Mission	Viking 1	Viking 2	Mars Pathfinder	MER-A Sprit	MER-B Opportunity	Phoenix	MSL
Landing Year	1976	1976	1997	2004	2004	2008	2012
Entry Velocity (km/s)	4.7	4.7	7.26	5.4	5.5	5.6	5.9
Entry Flight Path Angle (°)	-17	-17	-14.06	-11.49	-11.47	-13.0	-14.5
Entry Mass (kg)	992	992	584	827	832	602	3300
Aeroshell Diameter (m)	3.5	3.5	2.65	2.65	2.65	2.65	4.5
Ballistic Coefficient (kg/m^2)	64	64	63	94	94	65	135
Entry Angle of Attack (°)	11	11	0	0	0	0	18°
Parachute Deploy Mach	1.1	1.1	1.57	1.77	1.77	1.65	1.7
Touchdown Mass (kg)	590	590	360	539	539	364	1665
Payload Mass (kg)	244	244	92	173	173	167	899
Landing Site Elevation (km)	-3.5	-3.5	-2.5	-1.9	-1.4	-4.1	1.0
3σ Landing Ellipse, Major Axis (km)	280	280	200	80	80	55	20
3σ Landing Ellipse, Minor Axis (km)	100	100	100	12	12	20	10

In an effort to reduce the program costs, the landed and payload masses decreased after the Viking missions until the Mars Science Laboratory (MSL). However, the ballistic coefficient has generally increased as the understanding of the EDL systems and environment advanced. In addition, the landing uncertainty ellipse sizes have decreased as a result of better entry interface targeting and landing site maneuvering, as well as active guidance in the hypersonic descent phase in the case of MSL.

1.3 Problem Statement

1.3.1 Need for Larger Landed Masses

Future Mars missions such as a sample return system or crewed surface landings will require significantly larger payload masses than have been landed previously. Robotic sample return missions may require 2-10 tons of payload, while crewed missions may require 40-80 tons [5]. These payload masses are out of the realm of possibility for the Viking-era entry vehicles. For a landing at average Mars elevation, a 4.5 diameter aeroshell without lift is limited at landing payload masses of about 850 kg or less [5]. For larger masses, the aeroshell cannot provide sufficient deceleration due to drag to sufficiently reduce the vehicle's velocity to a safe level before landing. There are two main options to land larger masses: split up the payload into multiple landing missions, or increase the deceleration force during part or all of the EDL timeline.

It is possible to split up the surface payloads into multiple EDL vehicles with smaller mass payloads; however this results in duplicate sets of hardware and a higher overall mass that must be launched to Mars. More critically, these payloads would have to be landed very close to one another if they are to be feasibly re-combined. The state of the art landing

uncertainty at present is that achieved by MSL, which has a landing uncertainty ellipse of 10 km [10] in the major axis. While this distance is within the capability of past Mars rovers, travelling that distance would take months or years to achieve. This would create a significant risk of failure during travel before the primary mission could continue. Similarly, for crewed landings, a trek of several kilometers is unacceptable to reach cargo supplies given the significant consequences of any failures along the way. Therefore, for this multiple-landing scenario to be feasible, the landing uncertainty must be decreased by an order of magnitude. Even so, the cost of landing multiple vehicles for a single mission may prove to be prohibitive.

1.3.2 Limitations of Viking EDL Technologies

As the desire for increased scientific return increases, resulting in larger landed payload mass requirements, the deceleration capability of the Viking-era 70° sphere-cone geometry will be surpassed. The diameters of these heat shields are limited by the fairing size of the launch vehicles available. MSL has used the largest heat shield of any lander at 4.5 m diameter. The Martian atmosphere is thin compared to Earth's, as shown in Figure 1.5, which decreases its effectiveness at decelerating landing vehicles safely. However, the drag during entry is substantial enough to cause significant heating on the vehicle during descent, and therefore cannot be completely neglected.

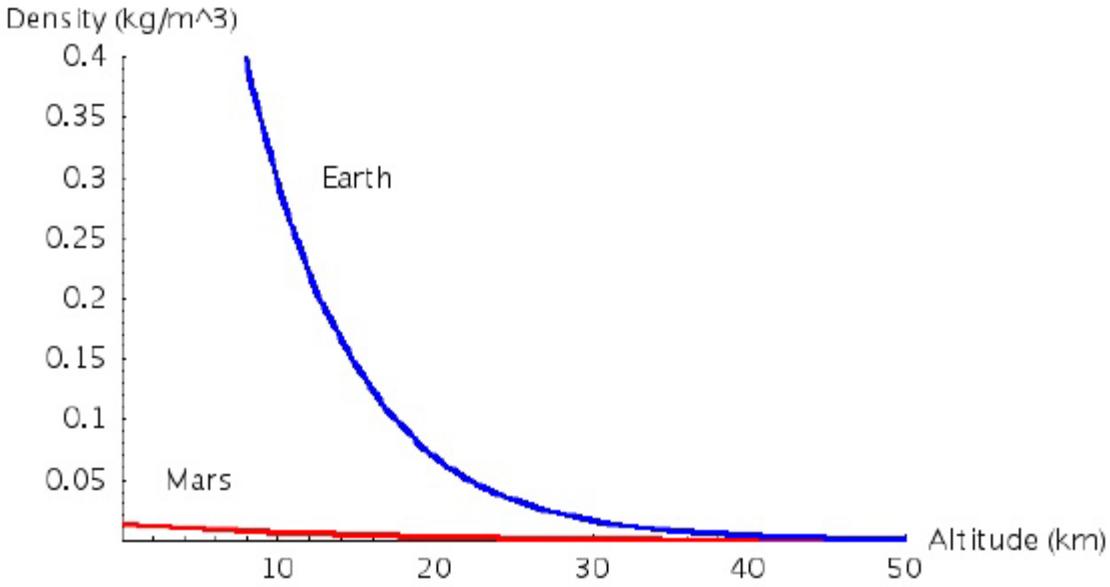

Figure 1.5: Atmospheric density of Mars and Earth [5]

The ability of a given passive vehicle to decelerate during atmospheric entry is dictated by the ballistic coefficient β:

$$\beta = \frac{m}{C_D A} \tag{1.1}$$

The ballistic coefficient describes the vehicle's inertia compared to its ability to decelerate due to atmospheric drag. A lower ballistic coefficient allows a vehicle to decelerate earlier in the descent phase and higher in the atmosphere, which reduces the heat load on the vehicle and allows for more time in subsequent events in the landing sequence. The maximum ballistic coefficient for a 70° sphere-cone geometry heat shield is approximately 135 kg/m^2 [5]. If the desired payload mass is to be increased, the area of the heat shield must be increased proportionally to allow for a safe landing. Since the area of a rigid heat shield is fixed by the launch vehicle, there is an upper limit on the entry mass that can be landed using Viking-era technology. For a 40-ton entry vehicle mass (the usable payload mass has been on the order of 15%-30% of the entry mass [5]), the aeroshell would

have to be on the order of 15 m in diameter to maintain the same ballistic coefficient. Similarly, a 100-ton entry vehicle would require a 25 m diameter. This size aeroshell is clearly impractical to be launched intact and in-space assembly presents another set of complex problems and increased cost.

In order to address the issue of landing larger payloads on Mars than current capabilities allow, the use of additional decelerator systems during the supersonic phase of flight has been proposed. Cianciolo et al. provide an overview of a NASA study of entry, descent, and landing systems required for future robotic and manned missions to Mars [11]. For the human class payload sizes, 8 architectures were examined across the entire entry, descent, and landing timeline, as shown in Figure 1.6. Several recently developed concepts were analyzed in the supersonic and hypersonic descent regimes. The main decelerator options common in current research and development are deployable decelerators and propulsive systems. The deployable decelerators examined in the NASA study are hypersonic inflatable aerodynamic decelerators (HIAD), supersonic inflatable aerodynamic decelerators (SIAD), lifting variants of these two options (LHIAD and LSIAD), and rigid aeroshells configured with mid- lift-to-drag values (L/D AS).

	Aerocapture	Hypersonic	Supersonic	Subsonic
Architecture 1	Rigid Mid-L/D AS	Rigid Mid-L/D AS	Propulsion	Propulsion
Architecture 2	Lifting HIAD	Lifting HIAD	Propulsion	Propulsion
Architecture 3	N/A	Propulsion	Propulsion	Propulsion
Architecture 4	Rigid Mid-L/D AS	Lifting HIAD	Propulsion	Propulsion
Architecture 5	Rigid Mid-L/D AS	Lifting HIAD	Same LHIAD	Propulsion
Architecture 6	Lifting HIAD	Lifting HIAD	Same LHIAD	Propulsion
Architecture 7	Rigid Mid-L/D AS	Rigid Mid-L/D AS	Drag SIAD	Propulsion
Architecture 8	Lifting HIAD	Lifting HIAD	LSIAD–Skirt	Propulsion

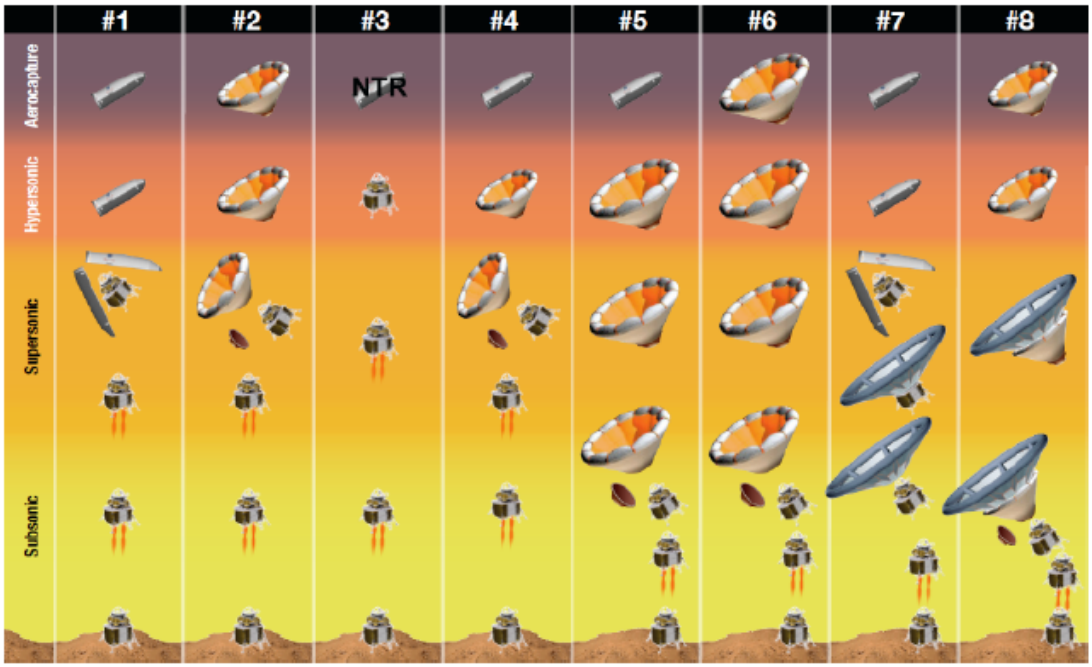

Figure 1.6: NASA EDL systems study architecture options [11]

The deployable decelerator solutions are summarized in Section 1.4 and discussed further in Section 2.1.2. The use of rocket propulsion in the descent phase is discussed in Sections 1.5 and 2.1.1.

1.4 Deployable Decelerator Systems

1.4.1 Parachutes

Parachute systems for previous Mars landing missions have used 10-20 meter diameter disk-gap band parachutes following the designs for the Viking missions. These parachutes have been deployed at conditions below Mach 2.1. It is possible to increase the

size of these parachutes or to use parachute clusters; however some issues do arise with scaling such a design. At higher deployment Mach numbers, the thermal environment becomes excessive for the parachute materials. As the vehicle mass becomes larger, the parachute size must also increase, which results in opening time penalties. For a 100 ton entry vehicle (payload plus EDL hardware), a 130 m diameter parachute would be required [5], which is an order of magnitude larger than current parachutes. Due to their size and associated timeline risks, new developments of parachutes are impractical as a single solution to increasing landed vehicle mass.

1.4.2 Inflatable Aerodynamic Decelerators

Inflatable Aerodynamic Decelerators, or IADs, are conceptually simple devices to increase the area of the vehicle's aeroshell by deploying a larger, flexible structure. Variants intended for supersonic deployment and hypersonic deployment exist, with the thermal environment being the driving difference between the two options. The larger drag area results in a proportionally larger drag force and smaller ballistic coefficient. Both attached and trailing IADs have been proposed. Attached IADs have been shown to be preferable because they are placed at the leading edge of the vehicle in free stream flow, whereas trailing IADs are located in the separated flow wake of the entry vehicle and are thus less effective at creating drag.

IADs consist of flexible membrane structures that are stored inside the entry vehicle until the appropriate point in the descent profile. They are then deployed through the use of gas generators or pressure tanks. Some types of IADs are kept pressurized through the use of ram-air inlets which use the free stream flow total pressure to keep the structure inflated. With careful design, the IAD stress field can be optimized to allow for lightweight flexible

materials to be used, resulting in a low-mass solution to increase the drag area of Mars EDL vehicles.

1.4.2.1 Tension Cone IADs

The tension cone design consists of a single flexible membrane, which is designed to only contain tensile stresses. It is attached to the edge of the vehicle's rigid aeroshell, and restrained by an inflatable compressive torus. A diagram of the tension cone is shown in Figure 1.7.

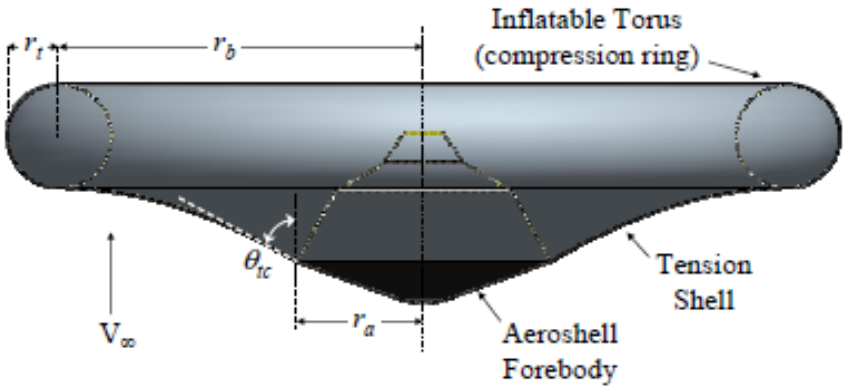

Figure 1.7: Tension cone IAD [12]

The IAD half-angle, θ_{tc}, is not the same as the aeroshell half angle. The final geometry of the tension cone can be obtained through iteratively solving the pressure distribution from the flow on the IAD and solving for the resulting IAD shape [12]. Since they are similarly blunt objects, the tension cone IAD preserves most of the drag coefficient of the sphere-cone aeroshell.

1.4.2.2 Isotensoid IADs

The isotensiod design was developed by Goodyear Aerospace Corporation in the 1960's [12]. The design features uniform fabric stress along the entire surface with

constant tension in the support cords. The design also includes a 'burble fence' to aid stability in transonic and subsonic flow. Air-ram inlets are used to pressurize the interior of the IAD. A diagram of the isotensiod IAD is shown in Figure 1.8 below.

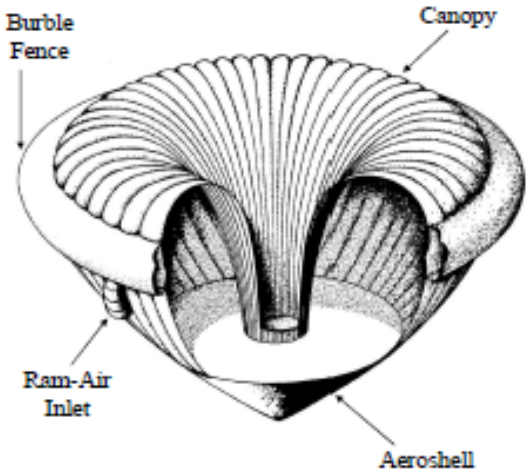

Figure 1.8: Isotensoid IAD [12]

As with the tension cone, the half angle of the isotensoid geometry is not the same as the aeroshell half angle. The tension cone construction uses less fabric material is required to achieve a given IAD diameter and thus is a lower mass system than the isotensoid. However, the isotensoid design allows for uniform fabric stress, which is preferable from fabrication and fluid-structure interaction standpoints [12].

1.4.3 Rigid Deployable Decelerators

Rigid deployable systems have not seen the same amount of research and development as inflatable options [13]. This is potentially due to perceived mass increases over IADs, as well as scaling issues for very large vehicle masses. However, in systems studies, rigid deployable decelerators have been shown to perform similarly to IAD concepts for large robotic-class missions and are estimated to carry lower risk and development

cost [14]. In addition, rigid deployable structures have the potential to be non-symmetrically configured (to create additional lift, for example), or can even be actuated as control surfaces to change the aerodynamic properties of the vehicle in flight.

1.5 Retropropulsion Systems

1.5.1 Subsonic Retrorockets

Subsonic retrorockets have been successfully used on multiple Mars landing vehicles to slow the vehicle from the terminal velocity of the parachute stage to a safe landing at the surface. This has been achieved with hydrazine engines, both off-pulsed (Phoenix) and throttled (Viking, MSL). The initiation of these systems has only been in the subsonic regime, and they also perform the task of navigating the vehicle to a safe landing site. In the past, retrorockets have been primarily utilized in the 'landing' phase of the EDL timeline where the vast majority of the vehicle's kinetic energy has already been dissipated.

1.5.2 Supersonic Retropropulsion

NASA first investigated supersonic retropropulsion (SRP) in the 1960s and 1970s as a way to decrease drag and vehicle body heating on supersonic vehicles, with Ref. [15] providing a parametric overview of analytic and experimental aerodynamics for SRP flows. A high-thrust nozzle located at the center of a blunt body face was found to significantly reduce or even eliminate the drag force on the body with the resulting axial force dominated by the thrust of the nozzle. More importantly, the resulting flow field redirects the oncoming flow with a high total temperature around the vehicle, reducing the heat flux that the body experiences.

An alternate configuration for supersonic retropropulsion is to place multiple nozzles near the edge of the aeroshell. At high thrust levels, the multiple jet plumes merge into a flow

structure similar to the central nozzle configuration. At low thrust levels however, the flow field around each jet is independent. The peripheral nozzle configuration also permits asymmetric thrusting, which could potentially be used to control the vehicle's attitude during flight.

Both the central and peripheral nozzle configurations have been studied for use in Mars EDL vehicles. SRP studies have generally focused on landing very high-mass payloads with correspondingly high-thrust and low-drag parameters. This concept is less favored for lower payload mass missions as compared to IADs because the SRP systems must carry and consume extra mass to reduce the vehicle's kinetic energy rather than using the atmosphere for a similar purpose. The current research in SRP technology is discussed further in Section 2.1.1.

1.6 Objectives

The objective of this thesis is to perform a systems architecture study of peripheral nozzle supersonic retropropulsion technology for use in Mars entry, descent, and landing vehicles. Peripheral nozzle SRP currently lacks simple analytical tools suitable for a systems level study to determine whether its drag preservation characteristics can be utilized to make SRP more efficient. This research focuses upon the following analysis areas:

1. Compare the ballistic coefficient of peripheral-nozzle SRP to other EDL technologies to determine potential benefits and flight regimes that merit further study.
2. Create an analytic drag model to describe the major parameters of the SRP flow field. This model combines analytic flow relations with results estimated from CFD simulations to describe the pressures acting on the vehicle.

3. Perform simplified trajectory simulations using the SRP drag model to determine the best operation regimes operational timeline to land the highest mass payloads with the least amount of SRP subsystem mass.

4. Evaluate potential combinations of SRP and other supersonic decelerator systems to increase the landed vehicle mass.

1.6.1 Importance of Research

This research is a preliminary systems-level study of a less prevalent EDL technology for use in future high-mass Mars lander missions. This research will identify the flight regimes and mission classifications that may benefit from peripheral nozzle SRP during EDL. The benefits and costs of SRP will be identified to facilitate further systems architecture trade studies that are geared towards end-to-end Mars EDL analysis, which often study combinations of several technologies combined over the course of the EDL sequence. This research also serves to identify further areas for more focused research into SRP technologies.

NASA has continued ambitions to land larger and more capable scientific payloads on the Martian surface, leading up to eventual crewed missions to the red planet. The Mars Science Laboratory currently represents the largest landed mass capability with a payload of 900 kg. As the payload mass requirements for these missions continue to grow (by over an order of magnitude for crewed missions), new technologies must be developed to safely decelerate the payloads during entry, descent, and landing. Mars landing missions have had low success rates in the past with most of these failures occurring in the EDL phase. As Mars landing payloads continue to advance in capability and size, the reliability of the entry, descent, and landing systems must continue to improve. The development of supersonic

retropropulsion technology, including flow field modulation using SRP, has been identified as a recommended area of technology development in NASA's Entry, Descent, and Landing Roadmap [13].

Previous research in the use of SRP systems has been predominantly focused in two areas: computational modeling and validation, and systems level studies of SRP applications on large mass vehicles with high thrust levels. Aerodynamic-propulsive interactions have been noted for a moderate subset of the relevant parameter space in both computational models and wind tunnel testing. The systems level studies have incorporated the aerodynamic-propulsive interaction by assuming the systems behave similarly across the relevant parameter space. Recently, there have been some efforts focused on understanding the driving flow mechanisms for drag-preservation SRP flows. However, there exists a lack of aerodynamic-propulsive modeling (computational or analytical) for the range of potential flight conditions. Lastly, the recent developments in understanding the drag-preserved SRP flow structures has not been thoroughly analyzed from a systems level perspective to assess its potential merits for implementation in Mars EDL.

1.6.2 Scope of Research

Entry vehicle mass is the primary driver for these studies, as it is directly related to launch and development costs. For peripheral nozzle SRP technology to be cost-effective in a given regime, it must be competitive in terms of total vehicle mass. This work will focus on the rapid, low-fidelity modeling of SRP aerodynamics as a function of free stream Mach number and the resulting prime regimes of SRP applicability for future Mars landing missions. A systems-level analysis will compare the efficiency of SRP in decelerating large vehicle masses to other deployable decelerators. In addition, the optimal operation timeline

during decent will be studied. Finally, hybrid supersonic decelerator concepts will be examined.

There are numerous other criteria to be evaluated when designing EDL vehicles such as reliability; guidance, navigation, and control accuracy; and development complexity and cost. While these criteria are important to evaluate, they are out of the limited scope of this thesis. This study is limited to study of the axial force components of the symmetric peripheral nozzle SRP configuration at various Mach numbers. Alternate flow structures such as asymmetric thrust profiles, angle of attack flight, or lifting configurations will not be examined though they do merit further study to full understand the SRP design space. Specific focus areas for further study in these criteria will be discussed at the conclusion of the thesis.

2 BACKGROUND

2.1 Current Research in Mars Entry, Descent, and Landing Technologies

2.1.1 Supersonic Retropropulsion

Supersonic retropropulsion describes the use of rocket engines to decelerate entry, descent, and landing vehicles during the supersonic phase of flight. Many recent systems level studies [5, 11, 14, 16, 17, 18] on the topic of supersonic retropropulsion focus on landing high mass payloads primarily using high thrust levels. At these high thrust levels, the drag force is diminished or effectively eliminated for both the central and peripheral nozzle configurations. The main deceleration force acting on the vehicle in this configuration is the rocket thrust alone. This requires that large fuel masses are carried along to sufficiently slow the vehicle for a safe landing, which in turn significantly decreases the payload mass fraction of the EDL vehicle.

Braun and Manning [5] explored the use of high thrust retropropulsion initiated towards the end of the descent phase (at Mach 3) and continued until landing (including allocation for cross-range maneuvers for final landing site approach). This system replaces parachutes for high mass payloads, as the parachute diameters become impractically large. The propellant alone in this retropropulsion approach varies between 20-35% for vehicle entry masses between 20 and 100 tons, as shown in Figure 2.1. This results in the need for 7 to 20 metric tons of propellant for the retropropulsion system.

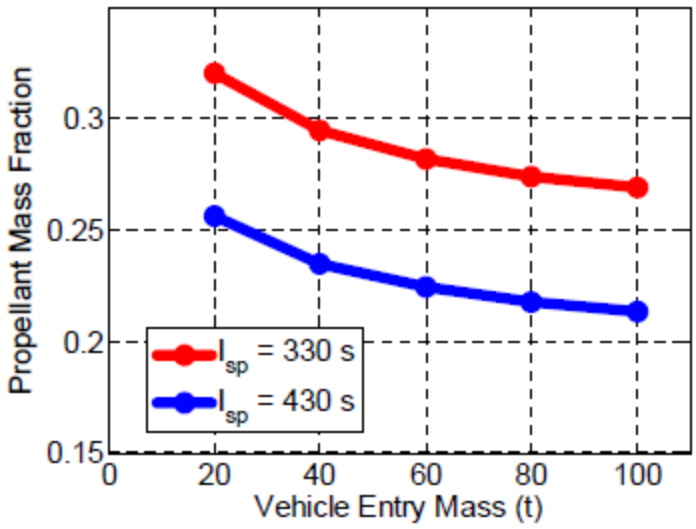

Figure 2.1: Propellant mass fraction for fully a propulsive landing [5]

Braun and Manning also identified a potential parachute-assisted retropropulsion approach. In this concept, a parachute is deployed at Mach 3 in addition to the initiation of retropropulsion as before. The decelerator combination must slow the vehicle to Mach 0.8 at 2 km altitude, where the parachute and aeroshell are separated for the final landing sequence. This approach reduces the propellant mass fraction to 12-18%, but can require parachute diameters in excess of 50 m for a 100 ton entry mass.

Marsh and Braun [18] described the fully-propulsive Mars entry trajectories using heat-rate constrained trajectories designed to eliminate the need for a thermal protection system. The propulsion system is assumed to be continuously throttleable between 0-100%. The heat-rate constrained trajectories require early initiation of retropropulsion at altitude of up to 80 km for entry from orbit and 140 km for direct entry. For a 60 ton vehicle, the resulting propellant mass fraction ranges from approximately 50-70% for entry from orbit and 65-85% for direct entry. These propellant mass fractions make this heat-rate constrained approach clearly inefficient, because the vehicle's kinetic energy that would otherwise be

dissipated using the atmosphere must instead be dissipated by the use of retropropulsion. This illustrates the massive mass penalties that can occur using retropropulsion systems, and the desire to utilize as much of the atmosphere's ability to decelerate the EDL vehicle as possible.

Korzun and Braun [16] further studied the use of supersonic retropropulsion taking into account the aerodynamic-propulsive interactions and drag preservation at certain thrust configurations. Drag preservation refers to scenarios when some aerodynamic drag acts on the vehicle in addition to the rocket thrust. When the drag preservation effects are neglected, it is desirable to minimize the amount of time that SRP is activated, as gravity losses are proportional to operation time. Korzun and Braun used the aerodynamic interaction model shown in Figure 2.2 which is based upon the Jarvinen and Adams data [15].

The thrust levels in supersonic retropropulsion analysis are commonly described by the thrust coefficient, C_T. This parameter nondimensionalizes the thrust force by the free stream dynamic pressure and the reference area, similar to other aerodynamic coefficients.

$$C_T = \frac{Th}{q_\infty A} \tag{2.1}$$

The relation between thrust coefficient and drag preservation is assumed to be independent of the free stream Mach number in the model shown in Figure 2.2.

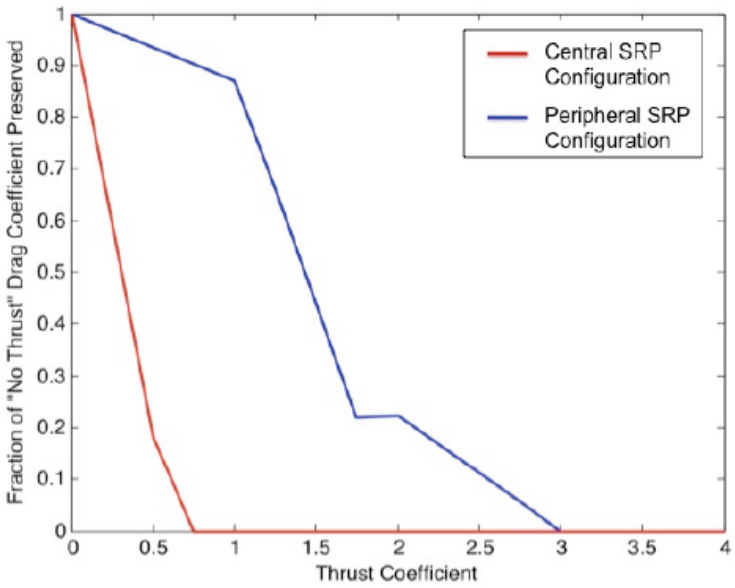

Figure 2.2: Drag preservation model from Ref. [16]

The results of this study showed that for ballistic coefficients less than 300 kg/m^3 there is some mass benefit to utilizing the drag preservation capability of peripheral nozzle SRP. For ballistic coefficients in excess of 300 kg/m^3, the thrust levels required are too high to benefit from drag preservation, as shown in Figure 2.3.

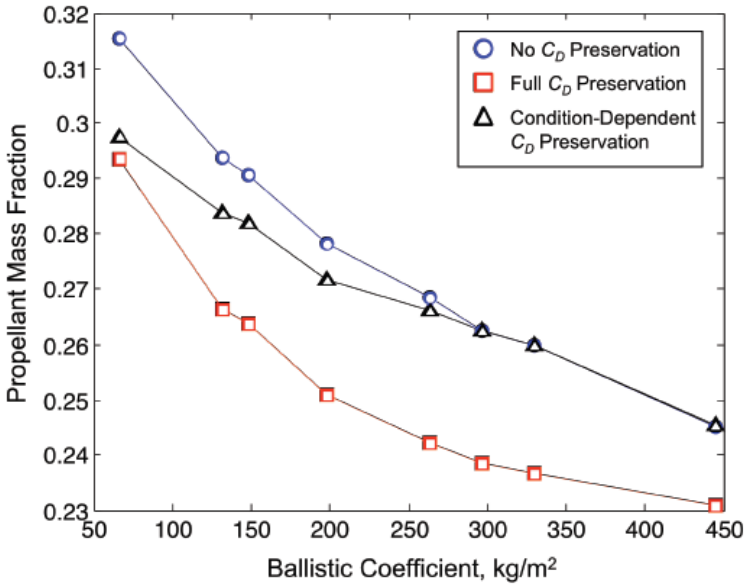

Figure 2.3: Propellant mass fraction for various drag preservation assumptions [16]

The full drag preservation curve indicates this assumption is poor and a more accurate and conservative assumption would be no drag preservation. The propellant mass fraction savings for the 'condition-dependent' drag preservation curve are larger for lower ballistic coefficients; however the propellant mass fraction decreases for all curves as the ballistic coefficient increases. The trajectories analyzed by Korzun and Braun preclude the possibility that the drag preservation effects change with Mach number or variables other than the thrust coefficient.

Bakhtian and Aftosmis [19] performed a parametric study of nozzle location, number, and orientation to assess their drag preservation properties. CFD simulations using the Cart3D solver were computed for all parametric nozzle variations. For the majority of cases simulated, the previous results of partial drag preservation or drag elimination were also observed. However, at higher Mach numbers and with peripheral nozzle configurations, drag augmentation of up to 20% was observed. The authors noted that this drag augmentation occurs when the SRP exhaust plumes penetrate the bow shock. This occurs at higher Mach numbers because the bow shock standoff distance is lower. The SRP exhaust plumes form shocks with portions of their geometry more inclined to the free stream, which act as oblique shocks are recover total pressure better than normal shocks. This theorized phenomenon results in higher pressures on the aeroshell front face, increasing the drag. A CFD visualization of the SRP shock structure for peripheral nozzles is shown in Figure 2.4.

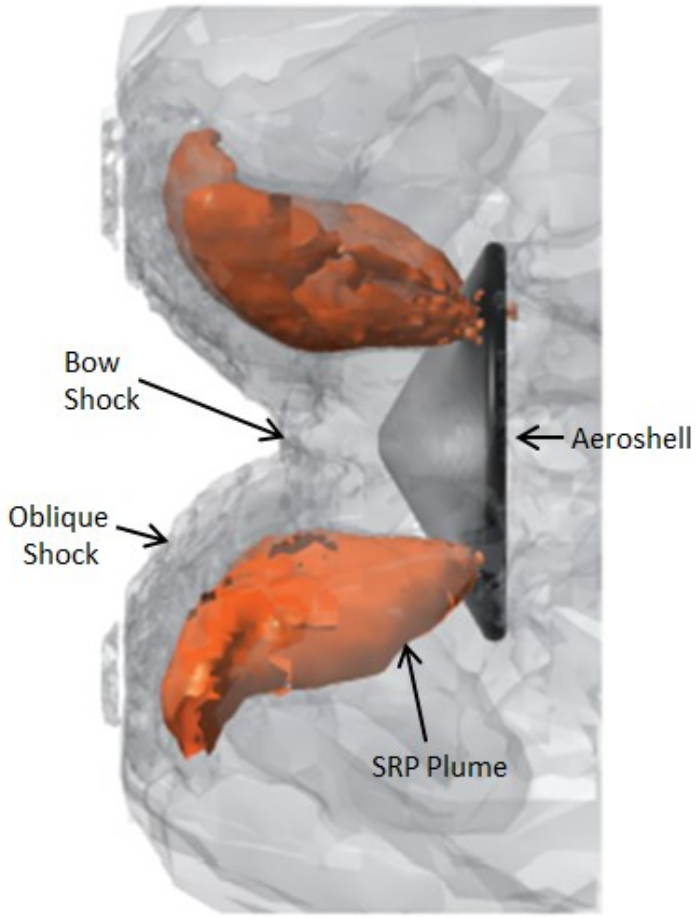

Figure 2.4: Peripheral nozzle SRP shock structure [19]

A further paper by Bakhtian and Aftosmis [20] outlines a simple quasi-one-dimensional flow model that calculates the drag coefficient based off the stagnation pressure of a flow passing through various combinations of normal and oblique shock cascades. These calculations assume an angle $\beta_w = 31°$ for the oblique shocks. The resulting stagnation pressures are applied across the entire aeroshell front face, and assuming ambient atmospheric pressure on the backshell, the coefficient of drag is calculated. In addition, a 'blend' model drag coefficient is calculated, which assumes the pressure on the aeroshell front face results from equal parts of flow passed through 3 different shock structures: normal, oblique-normal, oblique-oblique-normal. The performance of this drag-augmented

SRP model is assessed using the Mars Pathfinder mission as a baseline. The entry trajectories resulting from the various drag profiles calculated based on SRP shock structures are calculated, and the maximum vehicle mass that meets the end parachute deployment conditions is compared to the Mars Pathfinder vehicle mass. The mass model assumes a constant vehicle mass and does not directly examine the propulsion system required. SRP is assumed to be activated for the entire trajectory. Under these assumptions, the entry vehicle mass can be increased by a factor of 2.22 over the original Mars Pathfinder entry vehicle using the 'blend' drag augmentation model. A delayed activation tactic was also examined where the SRP was not activated until 15 km altitude. This increased the dynamic pressure at SRP activation, which correspondingly increases the drag force, and the drag augmentation attributed to SRP. This operation methodology increases the entry vehicle mass feasible by a factor of 3.04 (using the oblique-oblique-normal shock cascade).

Significant effort has also been recently focused on computational fluid dynamics (CFD) model validation of SRP flows. This includes both comparing CFD models using various solvers and comparing CFD results to wind tunnel testing. This validation has occurred at few discrete points over a wide range of flow parameters, including nozzle number and placement, thrust coefficient, nozzle exit conditions, free stream Mach number, and angle of attack. The CFD modeling has focused on the flow structure in front of the vehicle and pressure distributions on the aeroshell front face, without significant attention as to the flow aft of the vehicle.

The CFD analyses have been performed at various levels of fidelity. Since this thesis is focused on systems-level analysis, only a cursory overview of CFD studies has been included. Comparisons have recently been performed between various CFD codes [21, 22]

and have combined wind tunnel testing and CFD analysis [23, 24, 25, 26]. Bakhtian and Aftosmis [21] present comparisons of four CFD codes (Cart3D, DPLR, FUN3D, and OVERFLOW). The SRP flows considered range from Mach 3.48 to 4.6, thrust coefficients from 0.4 to 3, and include both central and peripheral nozzle configurations. Good agreement was shown between CFD codes in terms of surface pressure distribution and shock structure. Kleb et al. performed a comparison of four CFD codes [22] (DPLR, FUN3D, OVERFLOW, and US3D) and described the relative differences created by unsteady flow features. These differences are linked to the turbulence models utilized. In addition, Kleb et al. noted that due to the complexity of SRP flows, particularly due to the time-dependent shock structure, vortex shedding, and other unsteady effects, the mesh requirements and design order of accuracy are not apparent.

The unsteady flow features of the SRP flows have been noted across testing conditions and CFD modeling efforts [21, 22, 23, 24, 25, 26]. The dominant unsteadiness is attributed to vortex shedding of the SRP exhaust and has been measured experimentally and using CFD analysis to have a frequency of 1.7 to 2.3 kHz [21]. The measurement of the flow unsteadiness has been shown to be dependent on instrumentation in wind tunnel tests, turbulence models, and mesh definition [22, 25, 26]. This unsteadiness varies with the free steam Mach number and the thrust coefficient of the SRP, and its effect on vehicle stability is not clear.

Recent wind tunnel testing has been performed in the NASA Langley 4×4' Unitary Plan Wind Tunnel and the NASA Ames 9'×7' Unitary Plan Wind Tunnel. Both tests were designed as code-to-test of CFD analyses. The NASA Langley wind tunnel [25] performed tests at a free stream Mach number of 4.6 and varied the number of nozzles (0-4), thrust

coefficient (2, 3), angle of attack (0°, 12°, 16°, 20°), and roll angle (0°, 180°). The performance of three different CFD codes (DPLR, FUN3D, and OVERFLOW) was compared to the experimental results. The results of the study focused primarily on the unsteadiness inherent in the SRP flows. The wind-tunnel data was sampled at too slow of a rate to effectively capture all unsteady flow features, but some lower frequency unsteadiness was observed. The time-averaged pressure distributions resulted in significant errors between the CFD codes and wind tunnel results for some of the more unsteady test conditions.

Figure 2.5: 5-inch diameter aeroshell and mounting sting [26]

The NASA Ames wind tunnel testing [26] used the same model (Figure 2.5) as the NASA Langley testing, but was able to test higher thrust coefficients (up to 10) because the larger test section eliminated the tunnel blockage effects seen in the NASA Langley testing. However, this necessitated lower free steam Mach numbers (1.8 and 2.4). The one and three nozzle test configurations were observed to be more stable at the higher thrust coefficients tested. The largest difference between the CFD codes were once again the frequencies and magnitudes of the unsteady flow features.

A wind tunnel test was performed at the University of Virginia continuous-flow hypersonic wind tunnel on a scale model of the MSL aeroshell with 4-nozzle peripheral SRP at Mach 12 [23]. This series of tests are unique due to the high free stream Mach number, whereas the majority of wind tunnel testing and CFD analyses are at Mach 6 or lower. The wind tunnel tests at the University of Virginia were compared to CFD analyses performed by the University of Michigan using the LeMANS code. The CFD predictions of the shock structure were found to compare well with the test results. A relationship was established for the distance the SRP exhaust plumes penetrated the normal bow shock, shown in Figure 2.6. The jet penetration past the bow shock may play a significant role in drag preservation or augmentation.

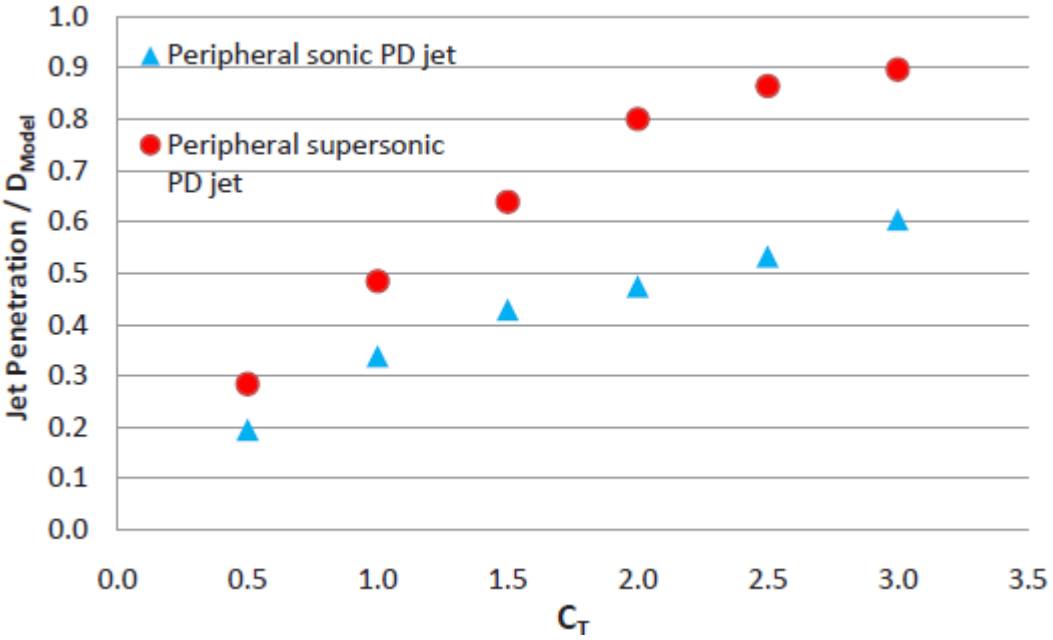

Figure 2.6: SRP shock penetration past bow shock [23]

However, the aeroshell model tested in this series of experiments placed the SRP nozzles approximately halfway between the centerline and the outer edge of the aeroshell. This decreased the drag preservation effects observed when compared with nozzles placed

more towards the periphery of the aeroshell as noted by Bakhtian [19]. This is due to the recirculation regions created between the SRP exhaust and the aeroshell periphery.

2.1.2 Deployable Aerodynamic Decelerators

A significant amount of research and technology development for deployable aerodynamic decelerators occurred in advance of the Viking missions. This technology has recently been revisited for use in EDL systems for planetary missions to Mars and other locations. The majority of recent work is focused on the preliminary designs of inflatable systems. Of these, the tension cone and the isotensoid designs have been the main focus. A comparison of their drag characteristics is shown in Figure 2.7.

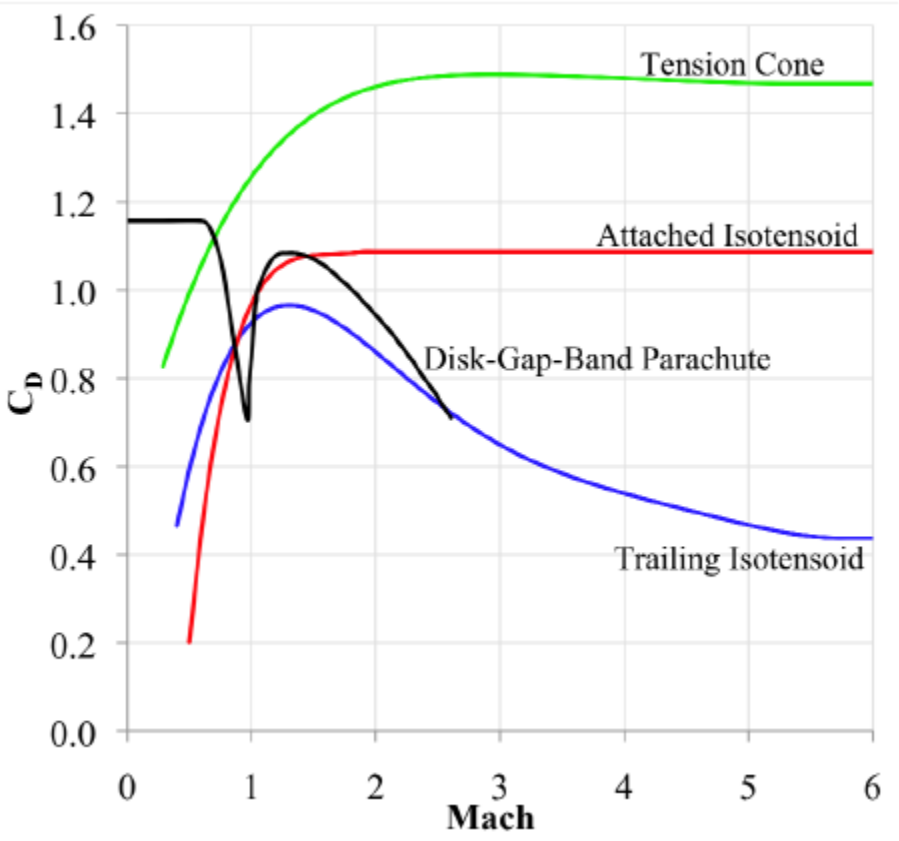

Figure 2.7: IAD drag coefficient comparison [27]

The tension cone IAD performs the best at all supersonic Mach numbers, while the traditional disk-gap-band parachute has a preferable drag coefficient at subsonic velocities.

The use of both isotensoid and tension cone IADs has been shown to result in statically stable aerodynamic configurations [27, 28] in wind tunnel testing. However, dynamic stability has not been assessed. Assessments of control authority for an IAD system or of landing uncertainty ellipse size are also limited. The dynamic stability and control authority properties of the IAD configurations will have significant impacts on their implementation. Dynamically unstable configurations present high mission risk and would require active control systems with significant authority. Active control for inflatable decelerators faces challenges with controlling large, flexible membranes and understanding the fluid-structure interactions of the deformable structure. Even dynamically stable configurations with large settling times may significantly hinder the landing accuracy of the vehicle. While IADs are an appealing technology for potential Mars EDL applications, a significant amount of technology development remains to fully characterize these systems.

As designs for IADs progress, the use of computational tools has been increasingly used to predict both aerodynamic and structural performance. Embedded shocks in the tension cone have been observed under some configurations, which alter the pressure distribution on the IAD and increases heating downwind of the shock [29]. Clark showed low error in CFD computations using the NASCART-GT code when compared to wind tunnel test data taken in the 10'×10' supersonic wind tunnel at the NASA Glenn Research Center [28]. The largest discrepancies arise in the pressure distribution on the aft surface of the IAD, which consists of separated flow and is turbulent.

In addition, detailed structural analysis is required to ensure the structural strength of IAD systems under off-nominal conditions. IADs are intended to have simple structural loading to enable the use of flexible fabric materials. This allows for the simple parametric design of the IAD structural properties and mass [30]. However, the use of fabrics introduces additional structural concerns, as fabrics must be in tension in both local principal directions to prevent bucking and wrinkling [27].

The use of flexible materials in IADs necessitates fluid-structure interaction (FSI) codes to analyze the aeroelastic effects and to understand the fluid and structural dynamics of the IAD system. Recently, FSI codes have been developed to couple flow fields with strong shocks and membrane structures or deformable solid structures, including aerodynamic heat flux and the resulting changes in material properties [31]. However, current FSI modeling efforts are limited by a lack of IAD testing data beyond qualitative comparison to images taken during testing. The use of in-situ sensors attached to the IAD surface can significantly affect the material response and so other quantitative data collection methods are required [27].

IAD systems can be extended to the hypersonic flight range (such a system is a HIAD) through the use of a flexible thermal protection system. HIAD systems commonly are a stacked toroid construction. A stacked toroid is similar to the tension cone supersonic IAD, except that toroids are stacked from the nose of the cone to the tail (instead of a single toroid at the tail). A HIAD test program, the Inflatable Re-entry Vehicle Experiment (IRVE), has successfully launched 3-meter diameter HIADs on sounding rockets and tested their performance during atmospheric re-entry. A CAD image of the IRVE-3 payload is shown in Figure 2.8.

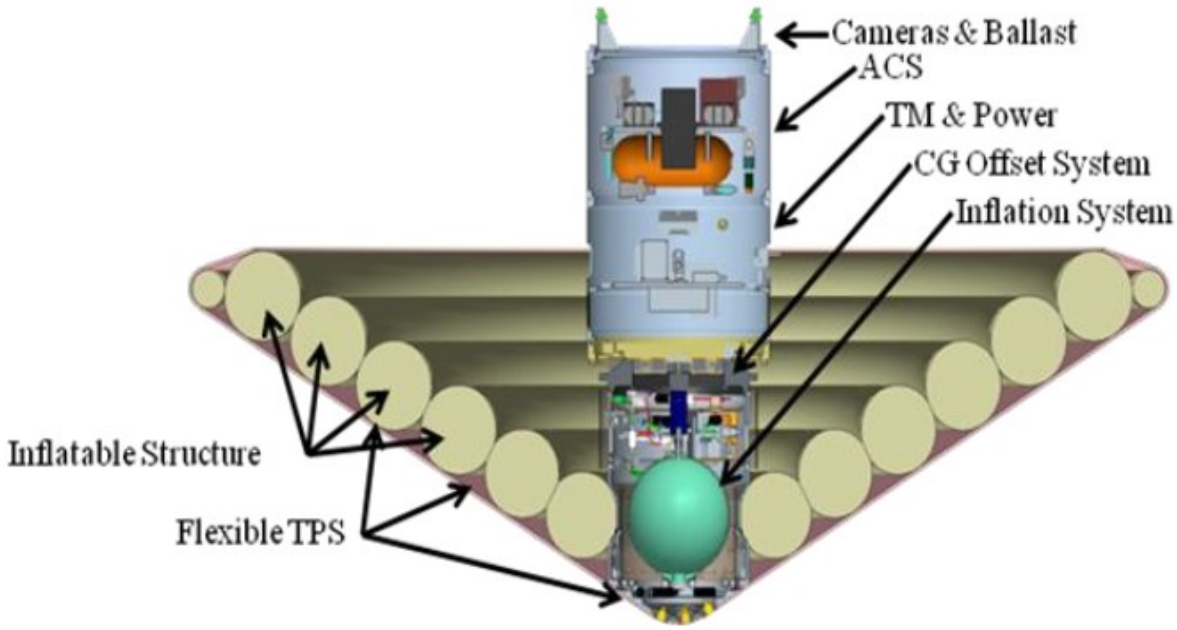

Figure 2.8: IRVE-3 payload cross section [32]

The thermal protection system may also function during an aerocapture maneuver, resulting in two heat loads. The materials science research for both flexible and ablative thermal protection materials is still active, but studies suggest that such materials can be created with reasonable masses [33].

Recent tests of IADs have been performed both in wind tunnel tests at small scale and large scale, as well as flight testing. These tests have both provided data on the aerodynamic and structural performance of IADs, but they have also allowed for development in detailed design issues such as stowage and deployment. IADs are typically deployed through the use of gas generators and/or ram air inlets. The required inflation pressure for deployment and to withstand aerodynamic loading determines the size of the deployment system. This pressure has been calculated both numerically [34], and demonstrated in wind tunnel testing, [28] as well as flight testing [32].

2.2 Supersonic Retropropulsion Flow Structure

The flow fields about blunt bodies when supersonic retropropulsion is added departs significantly from the nominal flow field structure. The retrorockets inject significant amounts of mass flow into the flow in front of the vehicle, which can distort the shock shape and location. The flow field characteristics depend on the thrust level, number of nozzles, and nozzle configurations. Analysis of these flows is generally limited to wind-tunnel experiments and CFD simulations.

2.2.1.1 Central Nozzle Configurations

The central nozzle configuration consists of a single nozzle located on the centerline of an axisymmetric body. The general flow field characteristics are shown in Figure 2.9.

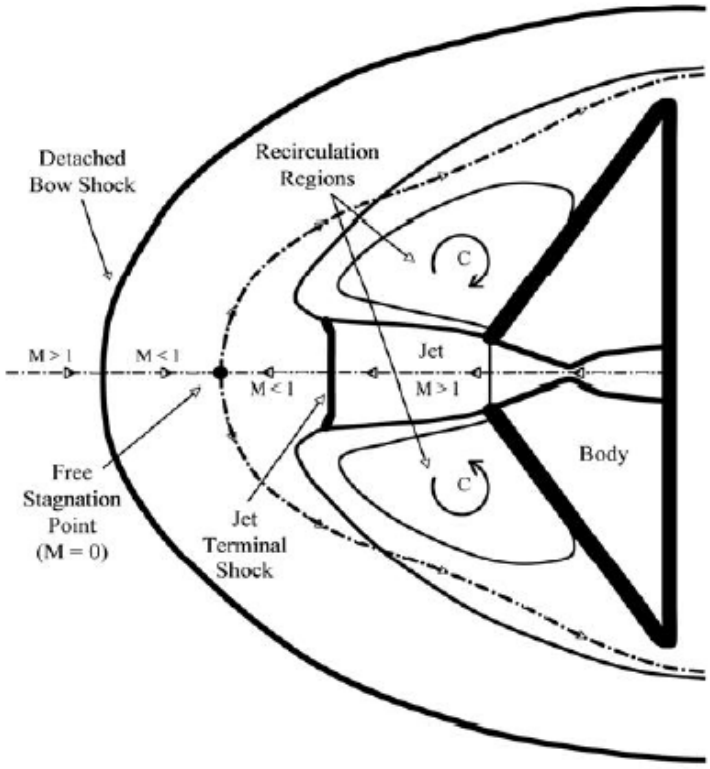

Figure 2.9: Central nozzle notional flow field [17]

The jet flow exits the nozzle at supersonic velocity, where it goes through a normal termination shock. The atmospheric flow passes through a bow shock, where it stagnates along the centerline against the jet flow. Two recirculation regions are formed adjacent to the jet flow against the aeroshell, which are turbulent regions of low pressure.

2.2.1.2 Peripheral Nozzle Configurations

An alternate configuration for supersonic retropropulsion is the use of multiple nozzles places radially away from the entry vehicle's centerline. As opposed to centerline nozzle configurations, peripheral nozzle configurations have been shown to better preserve drag forces on the capsule face, and even to augment the atmospheric drag.

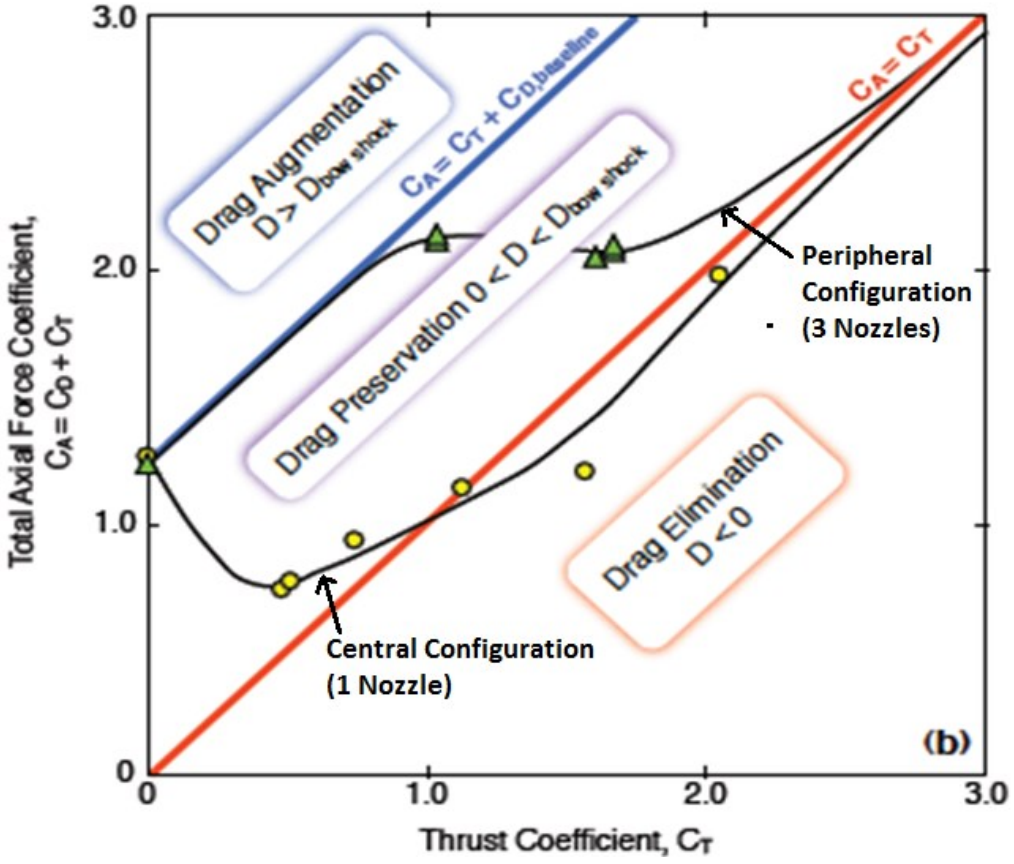

Figure 2.10: Drag characteristics of supersonic retropropulsion configurations [20]

Figure 2.10 shows performance trends for 1 and 3 nozzle configurations. For even very small thrust coefficients for the centerline nozzle configuration, the drag force on the capsule is essentially eliminated, leaving the axial propulsive force alone to decelerate the vehicle. Peripheral nozzle configurations preserve the drag force until a thrust coefficient of approximately 1.0. However, above a thrust coefficient of about 1.5, the peripheral configuration plumes merge, creating an aerospike similar to the central nozzle configuration, and all drag preservation is lost.

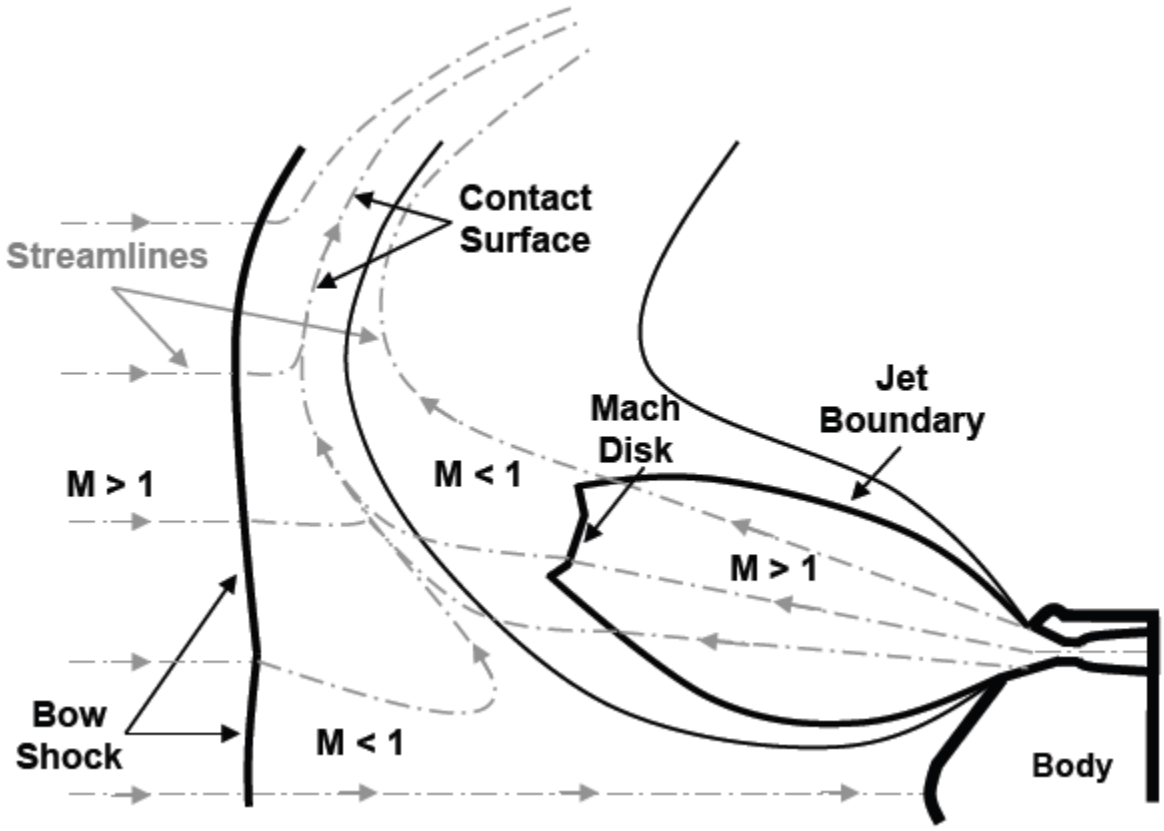

Figure 2.11: Peripheral nozzle notional flow field [24]

Figure 2.11 shows the major flow field characteristics of the peripheral nozzle configuration. The peripheral nozzle jet flow exits at supersonic velocity before passing through a normal shock. It is turned by the oncoming free stream flow, forming a contact surface. If the thrust coefficient is sufficiently large, the jet flow can significantly deform the

free stream flow bow shock, as shown in Figure 2.12. Small recirculation regions (not shown in Figure 2.11) are also formed between the nozzle and the edge of the aeroshell. The free stream flow near the centerline passes through the bow shock and is turned towards the jet, where it slows, compresses, and turns around the jet.

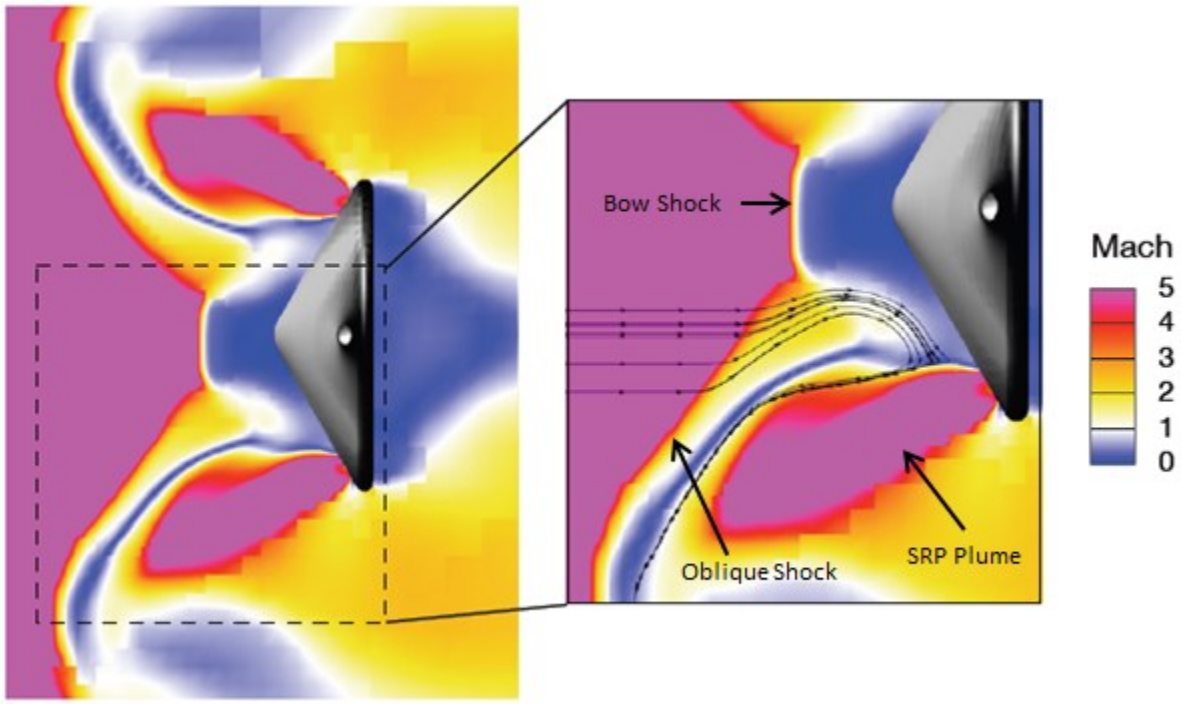

Figure 2.12: CFD flow field visualization of peripheral configuration SRP [19]

A set of parametric CFD studies performed in [19] investigated the use of 3 and 4 peripheral nozzle configurations, with various tilt angles of the nozzle with respect to the vehicle's centerline axis. The study was performed at M_∞ values of 2, 4, and 6. This study found the most efficient configuration to be 4 peripheral nozzles at low tilt angles.

The drag preservation and augmentation effects are theorized to be caused by the better total pressure recovery of oblique shocks compared to normal bow shocks. If plumes from the SRP engines are sufficiently strong to penetrate the bow shock in front of the entry capsule, the resulting shock structure has a much smaller radius of curvature, exposing some

of the flow to oblique shocks. These shocks also reflect, resulting in multiple shock-shock interactions that incrementally decelerate the flow, which results in better total pressure conservation and higher pressures on the aeroshell surface [20].

2.3 Summary

The Mars Science Laboratory (MSL) landing in August of 2012 represents the state-of-the-art in Mars entry, descent, and landing technologies. Since the first successful Mars landing by the Viking missions, the primary technological improvements on subsequent missions have been focused on improving the accuracy in landing at the targeted location. MSL also significantly advanced the amount of payload mass that can be landed on the surface. However, the mission also has approached the upper limit of the amount of payload that can be landed on Mars using current technologies. Future robotic missions to Mars as well as future crewed landings will require larger payload masses to be placed on the surface which necessitates the addition of new methods to the current state of the art in EDL.

In order to land larger payload masses, the deceleration during the supersonic and/or hypersonic phases of flight must be increased. The two leading supersonic decelerator options in recent studies are supersonic retropropulsion (SRP) and inflatable aerodynamic decelerators (IADs). IAD structures have been designed and modeled to have static shapes during aerodynamic loading and to have reproducible aerodynamic properties. These structures are deployed either using ram-air from the flow around the vehicle, or with an internal generator. IADs have been designed with a large diameter, which significantly increases the drag area of the vehicle on entry and thus lowering the ballistic coefficient. The current research thrusts in IADs are working to characterize the fluid-structure interaction between the flow and IAD membrane, dynamic stability, and control authority during flight.

These problems are challenging and may have significant effects on the implementation of IADs. However, IAD systems have been tested in full scale wind tunnels and flight (the IREVE mission) and present a promising future option in Mars EDL applications.

Supersonic retropropulsion (SRP) has typically been examined in high-thrust operation conditions for very large mass payloads. This methodology eliminates the assistance of atmospheric drag in decelerating the vehicle during EDL, which is an inefficient option. However, such operation schemes have been shown to be feasible for use in Mars EDL in recent systems studies. Much of the current focus in SRP research is detailed CFD modeling of the complex flow fields and validation with wind tunnel testing. The purpose of this modeling is to develop the tools to evaluate the aerodynamic-propulsive interactions inherent in SRP flows for analysis of a given SRP concept. However, the results generated by recent CFD modeling and wind tunnel testing is generally not intended for use in the conceptual design of an EDL vehicle, as the aerodynamic-propulsive interactions are generally assumed to be of secondary influence at this stage in the design.

Since the testing and modeling of SRP flows has not been adequately performed over the full range of the relevant flow parameter space, the design implications of the aerodynamics of SRP flows is not well formulated. There is evidence that, given proper operating conditions and vehicle design, the aerodynamic drag force acting on the vehicle can increase with the use of SRP which would improve the efficiency of the technology from a mass standpoint. By manipulating the shock structure using the flow exiting the SRP nozzles, oblique shock wave cascades can be generated to better recover the total pressure of the flow. This thesis will investigate the extent to which SRP systems can increase the vehicle drag and the implications on the amount of payload mass that can be landed on Mars.

3 AERODYNAMIC MODELING

3.1 Motivation

The flow fields for atmospheric entry vehicles, particularly with the addition of SRP, outlined in Section 2.2 are highly complex and cannot readily be solved analytically. These configurations have been tested in wind tunnels dating back to the 1960's and CFD simulations of SRP flows have been studied and validated more recently. However, both wind tunnel testing and CFD simulations require significant amounts of resources and time to evaluate even a single SRP configuration. While these investigations are necessary tasks in understanding SRP flows they are not well served for rapid, high-level design studies. Performing parametric studies of SRP flows for a sufficient range and resolutions of relevant flight parameters would require a significant effort, simply due to the large number of relevant flight parameters. Much of the recent detailed modeling of SRP flows has been focused on comparing the results between CFD solvers and wind tunnel data. However, these comparisons are few in number and have focused on a limited number of flow parameter sets. As a result, the available data for evaluating the drag augmentation capability of SRP flows is sparse.

To perform a systems level design and explore the trade space, a simplified model is required that can capture the most dominant aspects of SRP flow and give a sufficiently accurate prediction of SRP and vehicle behavior and can be run quickly. This allows for trends in the parametric space of SRP behavior to be broadly evaluated across the relevant conditions and direct a systems level study towards configurations of greatest interest. The

cost of creating this type of model is a loss in accuracy. The model uncertainty must be understood when analyzing the results; however a large model uncertainty is not necessarily prohibitive for conceptual systems studies. Such studies simply define the parameter space of interest to be solved in more detail and with lower uncertainties in future work.

There have been limited aerodynamic models for peripheral nozzle SRP configurations. Jarvinen and Adams developed the most commonly referenced empirical model for SRP flows [15], which relates the vehicle thrust coefficient to the total axial force on the aeroshell. However, this model was calculated for a free stream Mach number of 2, which exhibits minimal jet penetration past the bow shock. The model neglects the effects of Mach number on the shock structure and resulting flow structures, and is thus not sufficient for evaluating the full SRP design space. Bakhtian and Aftosmis developed an analytic quasi-1D flow model [20] calculating the total pressure behind a predetermined series of shock waves. This model is also insufficient for SRP parametric studies, as it neglects the various flow regimes in the aeroshell vicinity and simply assumes a constant pressure across the face of the vehicle.

This chapter will outline the development a drag augmentation model for peripheral nozzle SRP flows. The model is intended to capture the pressure distribution on the face of a 70° sphere-cone aeroshell as a function of free stream Mach number. This is done through estimating the size and types of the various flow regimes in the region ahead of the aeroshell using CFD results from previous studies and then computing analytic surface pressures using quasi-1D flow relations. The analytic techniques employed in the drag model are described in Section 3.2. The methodology for combining the analytical results and results estimated from CFD simulations into the full pressure model is presented in Section 3.3.

3.1.1 SRP and IAD Ballistic Coefficient Comparison

It is prudent to compare SRP system performance to other options for Mars EDL to establish relative performance and define a benchmark for the desired performance of SRP use. In this study, the primary parameter of concern is the maximum landed mass capability. As described in Section 1.3.2, the deceleration capability of a vehicle can be simply expressed by the ballistic coefficient β. By equating the ballistic coefficient for a theoretical SRP system and an IAD system, the necessary drag coefficient for SRP systems to match the ballistic coefficient of a given IAD system can be assessed. This comparison is not meant to indicate that a SRP system must be capable of the same ballistic coefficients as IAD concepts to be worth consideration. There are many elements beyond ballistic coefficient or landed mass capability in the systems trade space for supersonic decelerators. Rather, this comparison illustrates the relative comparison of the two technologies as a benchmark.

The ballistic coefficient is typically defined for passive vehicles, i.e. vehicles with aerodynamic forces alone acting to slow the body. However, for SRP systems the thrust produces by the rockets must be taken into account as well to quantify the total axial force on the vehicle. The thrust coefficient C_T (defined in Section 2.2) normalizes the thrust produced by the SRP system as a whole by the dynamic pressure and vehicle area, in the same way the drag force is normalized to create the coefficient of drag. This thrust coefficient is not equivalent to the thrust coefficient used in rocket propulsion analysis to characterize nozzle performance. Assuming that the SRP thrust is directed perpendicular to the drag vector, the equivalent ballistic coefficient is:

$$\beta_{SRP} = \frac{m}{(C_D + C_T)A} \tag{3.1}$$

To approximate relative performance between SRP and IAD systems, the ballistic coefficient expressions for the two systems are set to be equal to each other, $\beta_{SRP} = \beta_{IAD}$. The mass of each vehicle is broken down into the original vehicle mass (m_0) and the additional mass required for the decelerator system. The subscript *0* indicates parameters for the reference vehicle (Mars Science Laboratory).

$$\frac{m_0 + m_{SRP}}{(C_{D,SRP} + C_T)A_0} = \frac{m_0 + m_{IAD}}{C_{D,IAD}\, A_{IAD}} \tag{3.2}$$

This comparison essentially breaks down into the increased drag and thrust produced by the SRP system to the increased area of the IAD system (assuming the mass of each system is similar). Rearranging Eqn. 3.2 to solve for the required increase in drag coefficient for SRP systems to match a given IAD system yields:

$$\frac{C_{D,SRP}}{C_{D,0}} = \left(\frac{m_0 + m_{SRP}}{m_0 + m_{IAD}}\right)\frac{C_{D,IAD}}{C_{D,0}}\frac{A_{IAD}}{A_0} - \frac{C_T}{C_{D,0}} \tag{3.3}$$

Data for 4 tension cone IAD designs was used from Ref. [28] and is shown in Table 3.1 below.

Table 3.1: IAD reference value set [28]

Parameter	Value
Mass (kg)	104, 194, 326, 505
Diameter (m)	14, 17, 20, 23
Drag Coefficient	1.45

The baseline value of the thrust coefficient was 1.5. The SRP mass was determined using a nominal I_{sp} value of 220 seconds, which corresponds to a methane and liquid oxygen bipropellant engine. This configuration is popular for Mars landing system studies as methane can be produced from the carbon dioxide in the Martian atmosphere [35]. The mass

of the SRP system is calculated from the maximum flow rate required by the thrust coefficient and the maximum dynamic pressure from the Mars Pathfinder entry trajectory. The propellant mass can be varied by changing the operation duration to study the effect on the ballistic coefficient.

$$m_{SRP} = \frac{C_T q_\infty A_0}{I_{sp} g_0} t \tag{3.4}$$

The SRP mass can be varied by changing the operation duration to analyze the impact of changing the thrust level or operation time. The SRP mass was varied along with the IAD parameters, the thrust coefficient, and the reference vehicle mass. The resulting sensitivity plots are shown in Figure 3.1 - Figure 3.4.

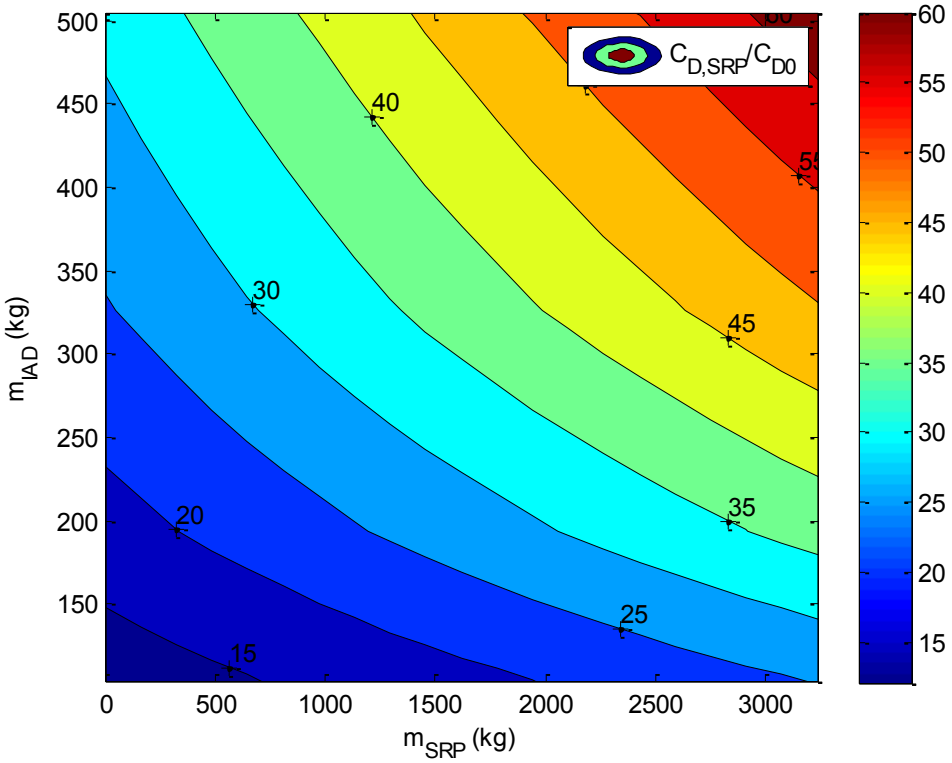

Figure 3.1: Required drag augmentation for SRP and IAD system masses

Figure 3.1 shows the required drag coefficient augmentation $\frac{C_{D,SRP}}{C_{D,0}}$ to match the IAD tension cone ballistic coefficient as a function of the mass of the SRP and IAD systems. The

drag area of the IAD system was incremented to match the corresponding IAD mass as defined in Table 3.1. The resulting data shows that SRP systems would need to create drag coefficients that are an order of magnitude larger than the current drag coefficient of the 70° sphere-cone aeroshell. This is true even if the mass of the SRP system is negligible, which is a consequence of the significantly increased drag area of the tension cone IAD. As would be expected, the required drag coefficient augmentation increases for a given IAD mass as the mass of the SRP system increases. It is interesting to note that the required drag coefficient augmentation also increases as the IAD mass increases when the SRP mass increases. This is because as the IAD mass increases, the drag area of the tension cone increases at a greater rate, making the ballistic coefficient smaller.

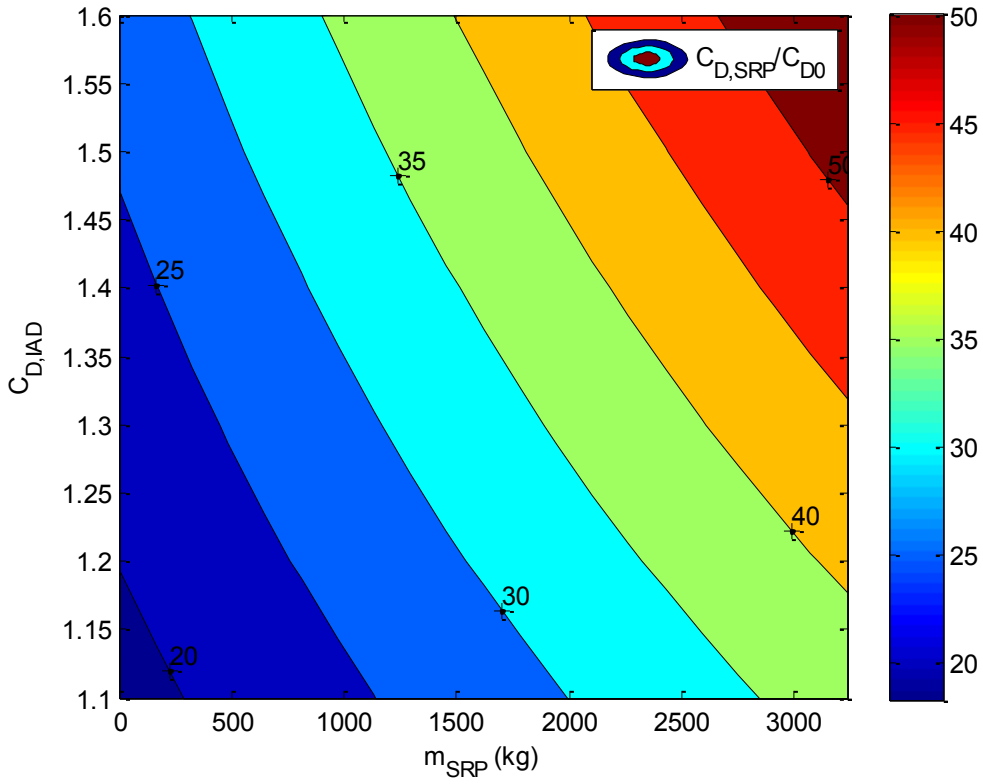

Figure 3.2: Required drag augmentation for SRP mass and IAD drag coefficient

Figure 3.2 shows the required drag coefficient augmentation for a range of IAD drag coefficients and SRP masses. The drag coefficient of a tension cone IAD is lower than that of the 70° sphere-cone aeroshell, but is also somewhat variable based on configuration [28]. Once again, the required drag coefficient for an SRP system to have an equivalent ballistic coefficient to an IAD system is an order of magnitude larger than the baseline. The change in IAD drag coefficient has less of an impact on the corresponding SRP drag coefficient for equal ballistic coefficients than the IAD system mass shown in Figure 3.1.

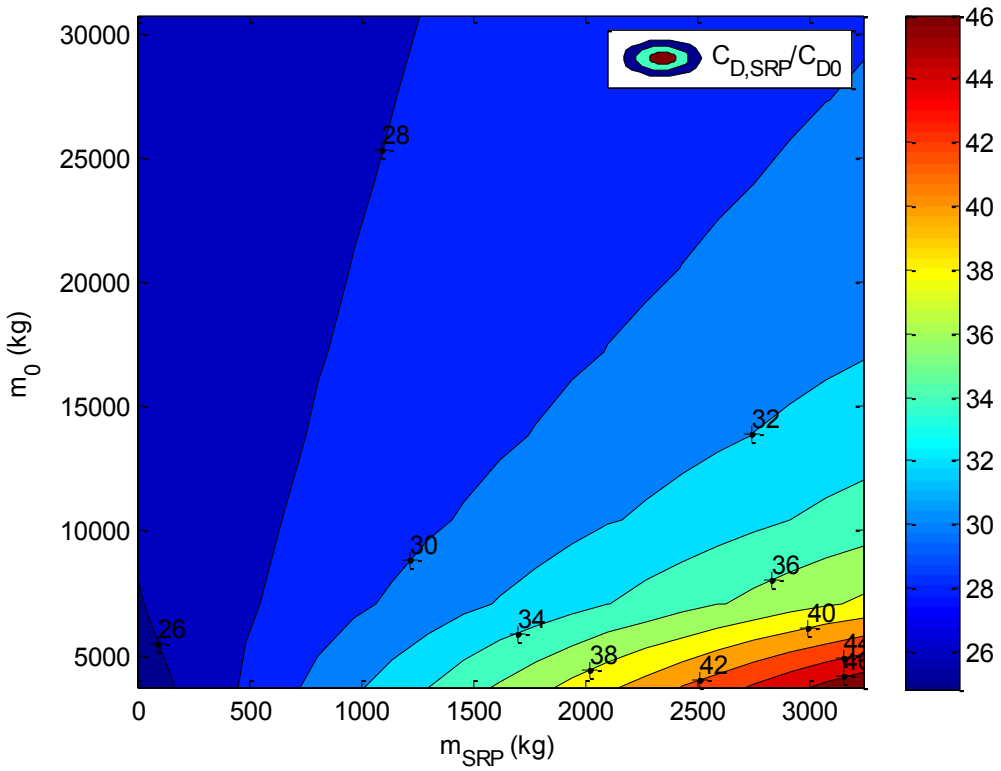

Figure 3.3: Required drag augmentation for SRP and reference vehicle masses

Figure 3.3 shows the required drag coefficient augmentation for SRP given various reference vehicle masses (i.e. the mass of the EDL vehicle before the addition of the SRP system). For low values of m_0, the required drag coefficient augmentation is very sensitive to changes in the SRP system mass. This is to be expected, as in this case the total mass would be primarily a function of the SRP system mass. As m_0 increases, the contribution of the

SRP system mass on the overall ballistic coefficient decreases. This conclusion is important to consider when assessing the utility of SRP for a given mission. Since the required thrust and thus mass for drag augmented SRP is independent of vehicle mass, it is a smaller impact to add an SRP system to a larger entry mass vehicle. However, as with all cases in this comparison with IADs, the required SRP drag coefficient augmentation values for the two technologies to have the same ballistic coefficient are large. This indicates that SRP systems may not be able to decelerate large entry vehicle masses as well as IADs.

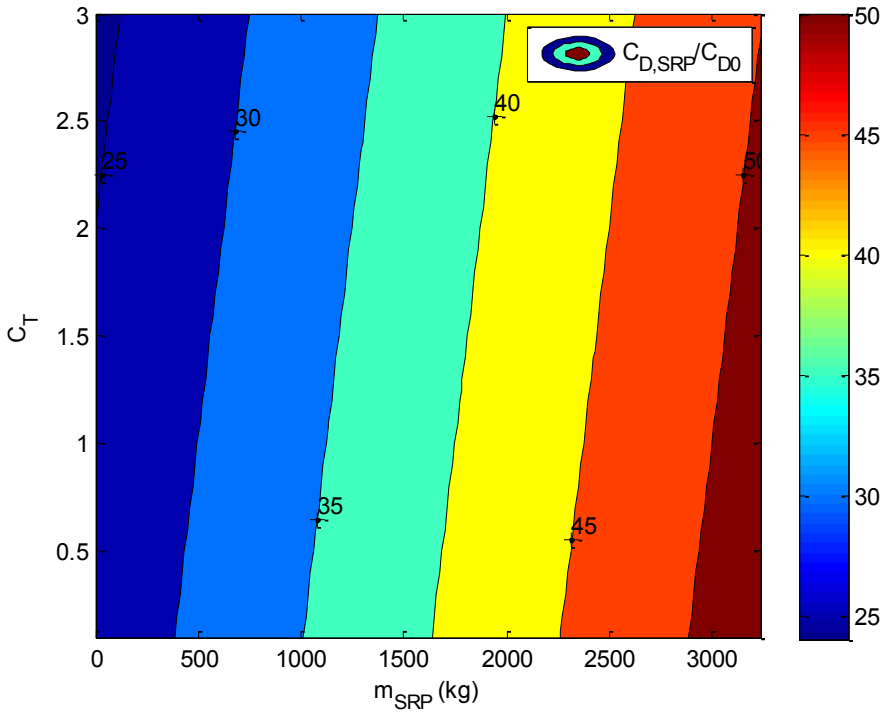

Figure 3.4: Required drag augmentation for SRP mass and thrust coefficient

Figure 3.4 shows the variation in drag coefficient augmentation required as the thrust coefficient is varied. The thrust coefficient is seen to have only a minor influence in this scenario relative to the mass of the SRP system. It is therefore more important for designers to focus on reducing the mass of the SRP system (for example, using higher specific impulse propellants) than operating the vehicle at higher or lower thrust levels.

For all studies in this section, the drag coefficient augmentation required for SRP systems to match the ballistic coefficient of IADs was on the order of 15 or greater. Assuming the SRP drag model based on the stagnation pressure from oblique shock cascades proposed by Bakhtian and Aftosmis [19], a simple indication of the possibility of such high drag coefficients can be examined. Figure 3.5 shows the increase in pressure coefficient for three different shock structures with free stream Mach numbers. The pressure coefficient is equal to the drag coefficient provided that the pressure is constant across front face of the aeroshell and the pressure on the back face of the vehicle is equal to static atmospheric pressure. These assumptions obviously sacrifice a significant amount of accuracy, but they do allow a simple illustration of the high speed flow behavior and order-of-magnitude comparison of trends.

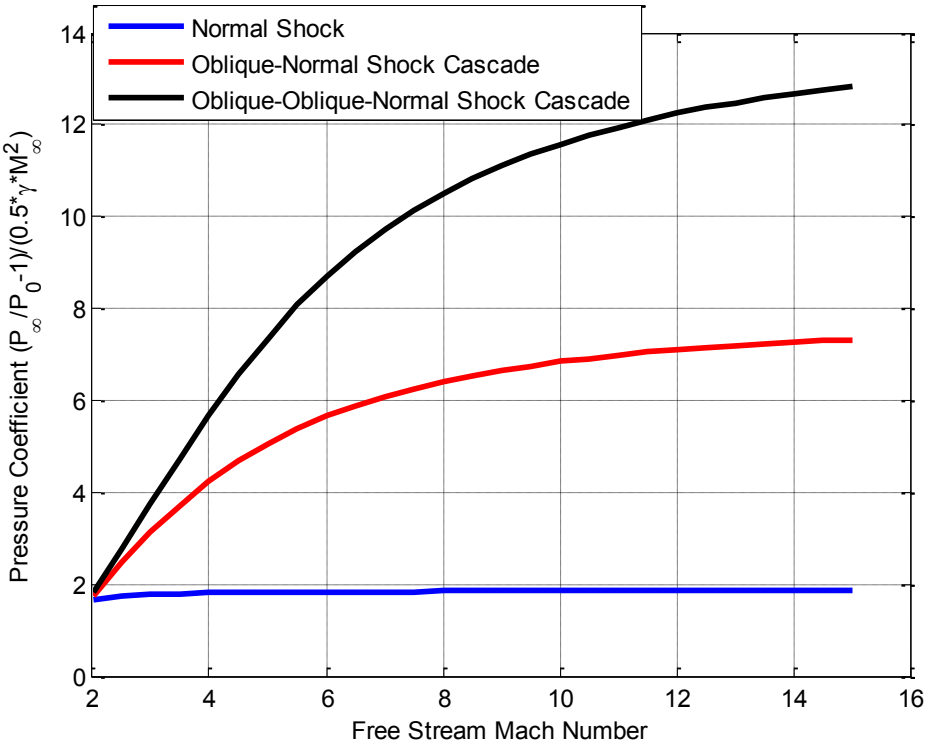

Figure 3.5: Pressure coefficient variation with free stream Mach number

Figure 3.5 shows that the increase in pressure is a factor of approximately 4.0 for an oblique-normal shock cascade, and 6.9 for an oblique-oblique-normal shock cascade. For the increase in drag coefficient values to be as large as the pressure coefficient, the shock cascade would have to extend over the entire front face of the aeroshell, which is not feasible using SRP as seen in Section 2.2. Even if this were possible, the increase in drag is still not significant enough to match the deceleration capability of IAD systems. Therefore, it is concluded that purely from a landed mass capability standpoint, IAD systems are superior to drag-augmented SRP systems. This does not preclude SRP systems from being useful, however. SRP can be operated at higher thrust levels to provide enough axial force to decelerate large masses (though they lose the aerodynamic drag force in doing so). In addition, there are many other system parameters to be examined for supersonic decelerator systems such as stability, variable operation modes, redundancy, landing site accuracy, downwind and cross range capability, etc. that must be considered in the preliminary design of a Mars landing vehicle. These additional considerations (which are not a focus of this thesis) may cause drag-augmented SRP to be an advantageous choice despite the decreased landing mass capability. As such, it is important to gain a better understanding of the deceleration capability of SRP systems and the types of vehicles and trajectories the technology is most applicable to.

3.2 Components of Entry and Descent Flow Fields

In order to analyze SRP flow fields over a wide range of relevant parameters, a model with a reduced level complexity is required that still captures the dominant behavior and flow physics for SRP flows that have been previously observed. The basic flow structure for

peripheral nozzle SRP flows was outlined in Section 2.2.1.2. While these flows are highly complex, there are some dominant physical mechanisms which can be modeled analytically. This section will outline the flow theory components relevant in SRP flows that will be combined to create the drag model in Section 3.3.

3.2.1 Isentropic Flow

The isentropic flow relations are commonly used to describe both incompressible and compressible fluid properties at any point in a flow in reference to some other value, such as the stagnation point properties. The isentropic flow relations are valid for all adiabatic and reversible flows. That is, the flow can have no heat addition from external sources, must be non-reacting, and must be inviscid. In addition, the fluid is assumed to be a perfect gas. The isentropic flow relations are derived by the energy equation, which is satisfied at every point in an isentropic flow [36].

The relations are also typically given in reference to the stagnation conditions since the total temperature, density, pressure, and enthalpy are constant in isentropic flow. These isentropic relations only apply between two points on a given streamline. Using the perfect gas relations and the stagnation enthalpy, the isentropic temperature relation can be derived [37]. The isentropic relations are provided in Appendix A.

These isentropic flow relations can be used to greatly simplify the flow field properties around a reentry vehicle. However, the isentropic assumption is not valid at several areas of the flow:

- Discrete shock waves are non-isentropic flow structures, and are discussed in Section 3.2.2.

- The flow diverges from the calorically perfect gas assumption at high temperatures.
- The flow near the boundary layer is subject to mass injection and reacting flow phenomena due to the heat shield ablation.
- The flow in the rocket exhaust may be chemically reacting.

While the isentropic assumption is not strictly an accurate assumption, the simplification it allows in the flow analysis is critical for this top-level systems architecture study. More accurate analysis would be required to assess the errors introduced by the isentropic assumption. This would likely have to be a high-fidelity CFD simulation or experimental testing. This is a separate area of study on its own and not discussed further in this research.

The pressure model created for this thesis uses the above isentropic relations. However, it is also an observation-based model, with the size and properties of each flow region based off data from numerical CFD simulations of SRP flows. Therefore, some of the non-isentropic effects mentioned above will be minimized by comparison of the model to numerical simulations that take into account these effects.

One non-ideal gas behavior that can be examined is the effect of changing specific heat ratio (γ) as a function of temperature for a gas. The specific heat ratio also changes as a function of pressure, but the effect is not as significant as the temperature dependence. Mars' atmosphere is approximately 95% carbon dioxide, and so the value of γ for the atmosphere is assumed to behave in the same manner as for CO_2, which has been tabulated in Ref. [38]. The behavior of γ for CO_2 is variable at low temperatures, but is less variable at high temperatures, as shown in Figure 3.6.

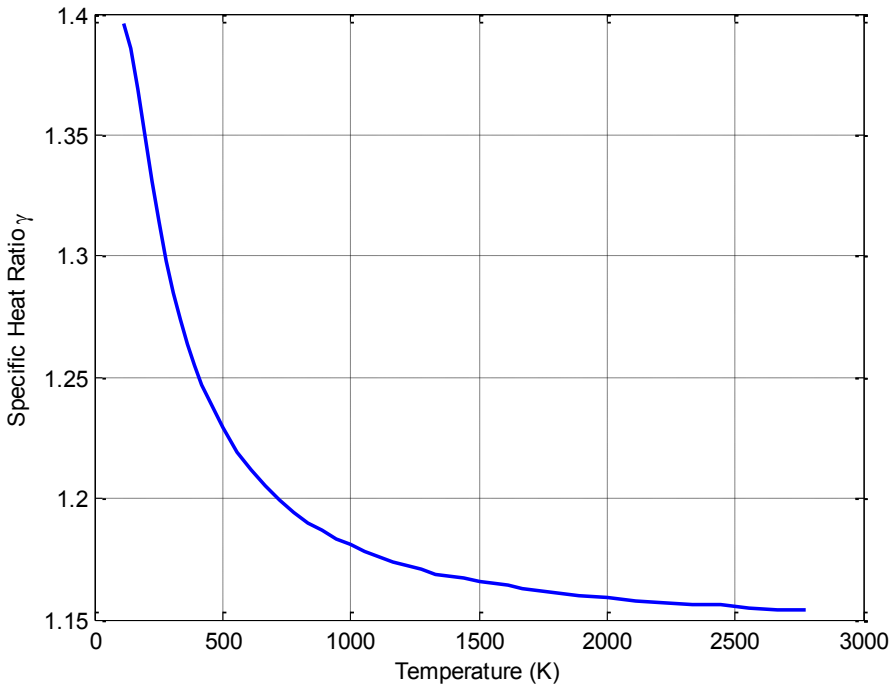

Figure 3.6: Variation of specific heat ratio with temperature for CO_2 [38]

Since the value of γ is dependent on temperature which increases sharply across shock waves, a higher fidelity model will take into account the changed value of γ behind the shock wave. The importance of this effect for the flow structures observed in SRP flows will be discussed further in Section 3.3.1

3.2.2 Shock Waves

Shock waves appear as discontinuities in supersonic flow around a body which compresses and decelerates the fluid flow. They are thin (assumed discontinuous) regions of strong viscous dissipation, which increase the static temperature of the flow and decrease its total pressure. Shock waves are not isentropic phenomena, and alternate relations are required to relate static flow properties on either side of the shock. The isentropic relations

can be combined with the shock wave equations to obtain the stagnation point properties behind the shock wave.

A bow shock wave occurs ahead of blunt objects in supersonic flow. The region in front of the stagnation point can be modeled as a normal shock as the shock wave is normal to the oncoming supersonic flow at this point. The entire flow is normal to the shock, and the flow must be subsonic on the other side. The continuity equation and velocity component relations can be used to derive the static pressure and density ratios across any normal shock [36]. The equation of state can then be used to calculate the static temperature ratio across the shock.

The normal shock equations can be generalized to oblique shock waves, in which the shock wave is inclined by some amount β_w to the oncoming supersonic free stream flow. Across any shock, the tangential velocity component remains unchanged while the normal velocity component decreases in the same manner as a normal shock [36]. The resulting flow deflection angle θ_d describing the amount the flow is turned across the shock can be determined by the normal and tangential flow velocities. The shock wave equations are provided in Appendix B.

3.2.2.1 Shock-Shock Interactions

There are several types of flow interactions relevant to SRP flows caused by intersecting shock waves. The simplest interaction type occurs when two shock waves intersect at a point where the flow downstream of each shock wave is supersonic. Two oblique shock waves are reflected from the original shock waves. Their wave angles are required to make the pressure and flow direction uniform [39] past the shock interaction structure (regions 4 and 5), as shown in Figure 3.7.

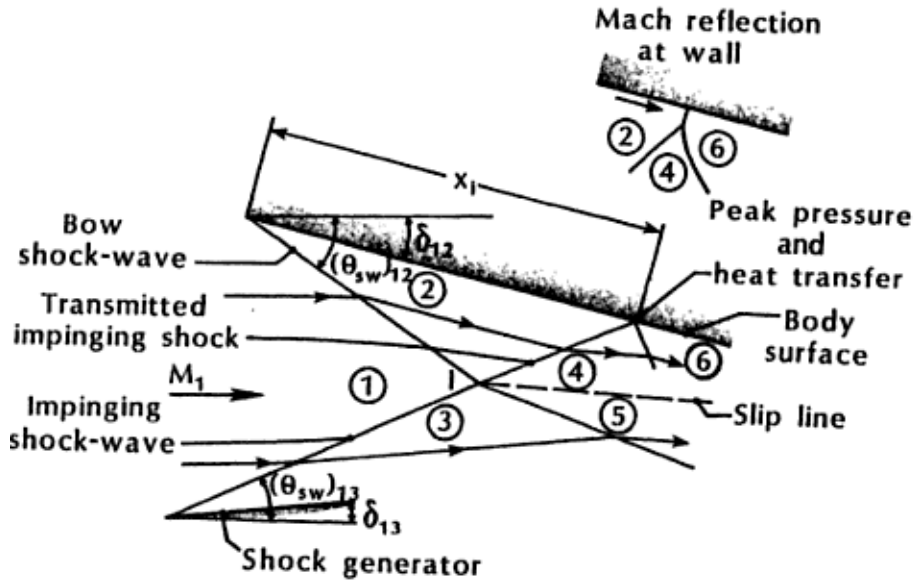

Figure 3.7: Oblique shock-shock interaction [40]

If the initial shocks have the same wave angle, then problem is symmetric and the flow angle in regions 4 and 5 are aligned with the free stream flow. If the initial shocks have different wave angles, the flow direction and pressure in regions 4 and 5 can be obtained based upon the known flow properties of regions 2 and 3. The required flow deflections to create parallel flow can be solved to determine the wave angles (β_w), which then permits the flow properties behind the shock structure to be solved by applying the shock relations.

The other types of shock-shock interactions that may be relevant to SRP flows consist of an oblique shock impinging on a bow shock where the flow downstream of the bow shock is subsonic. The behavior of the flow structures behind these interactions is dependent on the effects of the nozzle exit flow and pressure boundary conditions present near the aeroshell surface. Modeling these shock interactions is out of the scope of this work, but future work in this area may yield further insight into the behavior of the aerodynamic-propulsive interactions for SRP flows.

3.2.3 Nominal Capsule Flow Structure

The supersonic and hypersonic flows about blunt re-entry bodies like those used for Mars EDL are characterized by detached bow shocks, which are normal or nearly normal in the region in front of the vehicle. At zero angle of attack, the flow is axisymmetric about the vehicle's centerline (assuming an axisymmetric aeroshell). The flow aft of the vehicle is separated and turbulent. The pressure distribution on the backshell of the vehicle is highly complex and a current area of significant research and modeling.

3.2.3.1 Large Angle Sphere-Cone Pressure Distribution

For large angle cones in supersonic flows, attached shock waves are not possible and the entire shock structure becomes detached. The nose of the cone is generally blunted on the front of EDL aeroshells to decrease the peak convective heat transfer [40]. The flow over these aeroshells is subsonic over the entire face, with the sonic line occurring near the corner. For this velocity distribution to occur, the flow must accelerate radially towards the edge of the aeroshell. Modified Newtonian theory applied to large angle cones is not accurate due to the large flow deflection angles and detached shock waves, and does not predict the radial velocity gradient. The "sine squared deficiency" method was developed to alter the modified Newtonian method for the subsonic flow on the aeroshell face [41]. Anderson, Dahm, and Moyer [42] later improved the accuracy of the model and extended the validity to lower Mach numbers by modifying the expressions for the sonic point pressure and the pressure for a flat disc. Figure 3.8 shows the performance of this model along with test data for a 60° sphere-cone at zero angle of attack in a Mach 4.63 flow. The local static pressure to nose stagnation pressure ratio is plotted as a function of the ratio of the arc length (s) to the arc length from the nose of the aeroshell to the sonic point (s^*).

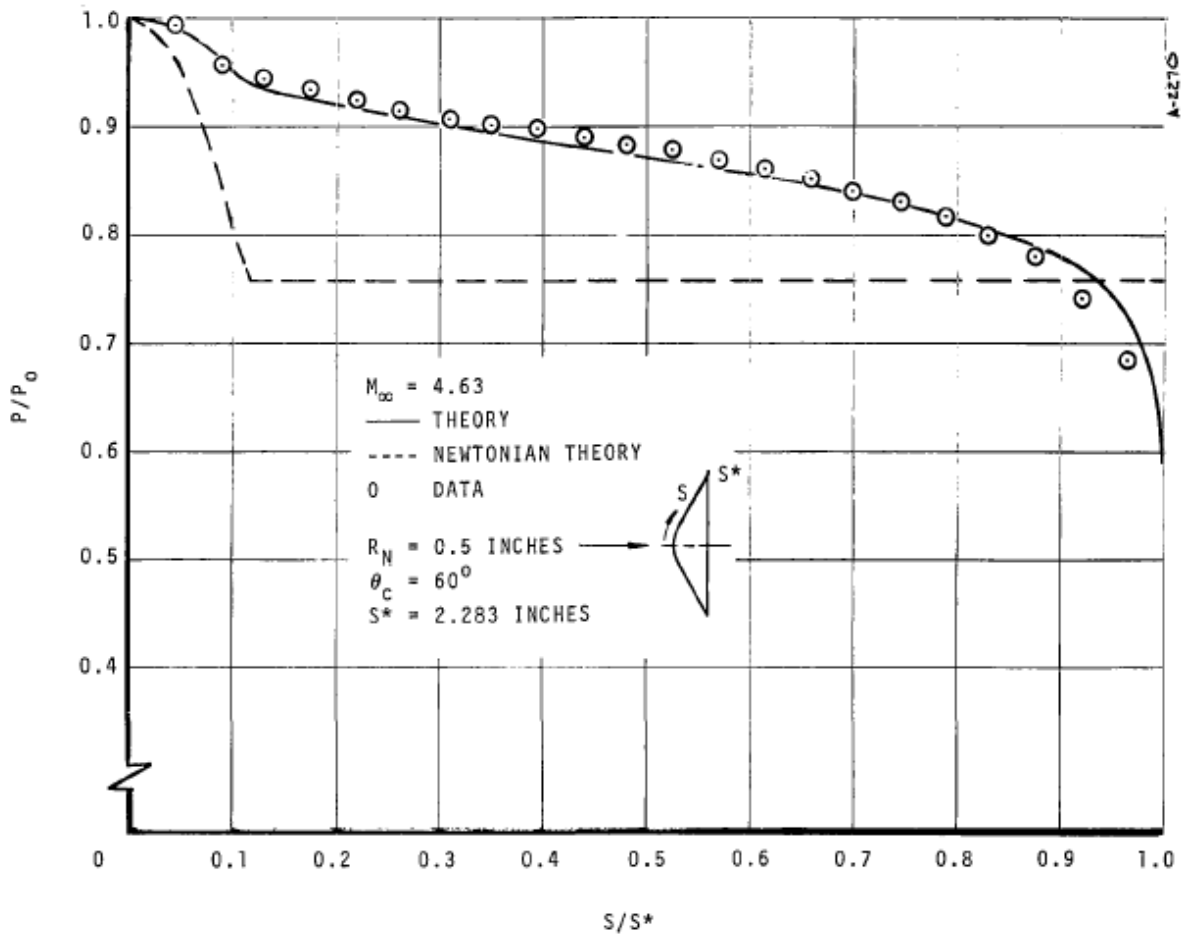

Figure 3.8: Static pressure distribution on aeroshell face [42]

The model is constructed by taking modified Newtonian theory and adding on several correction terms. The properties at the sonic point are noted with a star (*), and barred quantities have been normalized by the stagnation pressure at the nose. Figure 3.9 shows the geometry nomenclature used in this model.

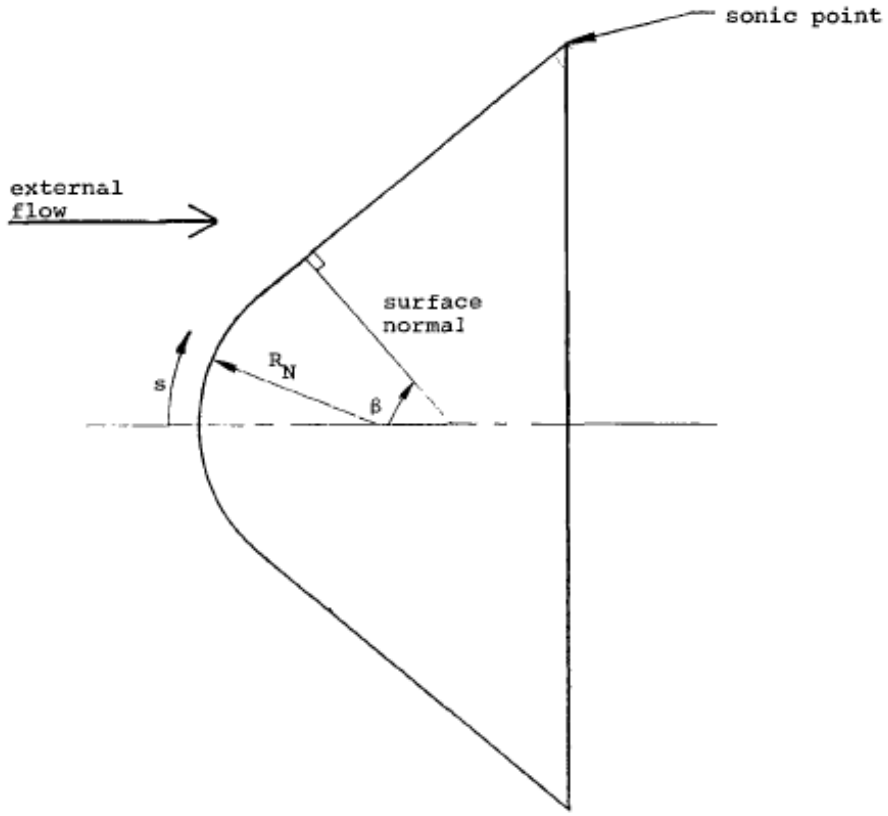

Figure 3.9: Reference geometry for sphere cone pressure distribution [42]

The full expression for the pressure distribution on a large angle sphere cone is provided in [42] as:

$$\begin{aligned}\bar{P} = \bar{P}_\infty + (1-\bar{P}_\infty)\cos^2\beta - (1-\bar{P}_{FD})\left(\frac{\cos^2\beta - \bar{P}^*}{1-\bar{P}^*}\right) \\ + \left(1-\frac{R_N}{R_{max}}\right)\left[\sin^2\beta\left(1-\frac{s}{s^*}\right)\right. \\ \left. + \frac{1}{2}\frac{s}{s^*}\left\{\bar{P}_{FD} - 1 + \frac{s}{s^*}\sin^2\beta + (1-\bar{P}_{FD})\left(\frac{\cos^2\beta - \bar{P}^*}{1-\bar{P}^*}\right)\right\}\right]\end{aligned} \tag{3.5}$$

where R_{max} is the maximum radius to the centerline perpendicular to the surface. The first two terms of Eqn. 3.5 represent the modified Newtonian pressure distribution when $\bar{P}_\infty$ is calculated from the stagnation coefficient of pressure, given by:

$$\bar{P}_{\infty} = \frac{1}{1 + \frac{\gamma}{2} M_{\infty}^2 C_{p,0}} \tag{3.6}$$

The value of the pressure coefficient at this location is calculated using the isentropic and shock wave relations.

The flow at the aeroshell corner is assumed to be sonic and so the pressure at the corner is known to be the sonic pressure. Assuming isentropic flow between the nose stagnation point and the aeroshell corner, the sonic pressure ratio is simply:

$$\bar{P}^* = \left(\frac{2}{\gamma + 1}\right)^{\frac{\gamma}{\gamma - 1}} \tag{3.7}$$

The flat plate pressure distribution is updated in [42] to more accurately predict the pressure based on energy considerations.

$$\begin{gathered} \bar{P}_{FD} = 1 - e^{-\lambda}(1 - \bar{P}^*) - \frac{1}{16}\left[\left(\frac{S}{S^*}\right)^2 - e^{-\lambda}\right] \\ \lambda = 5\sqrt{\ln\left(\frac{S}{S^*}\right)} \end{gathered} \tag{3.8}$$

This model has been demonstrated in [41] for sphere-cone geometries with varying nose radii and cone half angles, for free stream flow as low as Mach 2. Since the geometry of the aeroshell is axisymmetric and the capsule is not at an angle of attack, this model provides the pressure ratio at every location on the aeroshell surface.

3.2.3.2 Coefficient of Drag

The coefficient of drag is a critical component of the ballistic coefficient, and thus the EDL vehicle's trajectory. The coefficient of drag is defined as:

$$C_D = \frac{D}{q_{\infty} A} \tag{3.9}$$

The drag force on the vehicle can be obtained through a surface integral of the aerodynamic pressures on the projected area of the vehicle along the x-axis, assuming inviscid flow (and thus no shear stresses acting on the vehicle face). The drag force can be expressed as the following integral:

$$D = \int P(\hat{n} \cdot \hat{x}) dA \tag{3.10}$$

Applying the projection to the surface area and splitting the integration domain over the front and the back side of the capsule results in:

$$D = \int P dA_{x,front} + \int P dA_{x,back} \tag{3.11}$$

where $A_{front} = A_{back}$

If the backshell pressure distribution is simplified to an average value applied across the entire surface, the coefficient of drag can be expressed as:

$$C_D = \frac{\int P_{front} dA_x}{q_\infty A_x} + \frac{P_{back}}{q_\infty} \tag{3.12}$$

By expressing the free stream dynamic pressure in terms of Mach number, Eqn. 3.12 can be rearranged to express the drag coefficient as a function of the pressure ratio P/P_∞.

$$C_D = \frac{\int (P_{front}/P_\infty) dA_x}{\frac{1}{2}\gamma M_\infty^2 A_x} + \frac{P_{back}/P_\infty}{\frac{1}{2}\gamma M_\infty^2} \tag{3.13}$$

A conservative assumption is that the pressure on the back-face of a vehicle can be approximated by the atmospheric static pressure. However, due to flow separation, the pressure on the backshell will likely fall somewhere in between vacuum and atmospheric static pressure.

3.3 Drag Model

3.3.1 Flow Regions

The drag model created for this thesis breaks down the SRP structure into six basic flow field regions:

1. Flow through the normal bow shock.
2. Accelerated flow near the capsule periphery.
3. Flow through an oblique-normal shock cascade.
4. Flow through an oblique-oblique normal shock cascade.
5. Separated flow.
6. Nozzle exit flow.

The model calculates the flow pressures in each region in the aeroshell, and then integrates across the surface to determine the drag coefficient. The flow regions are shown in Figure 3.10 and compared to CFD results from [19].

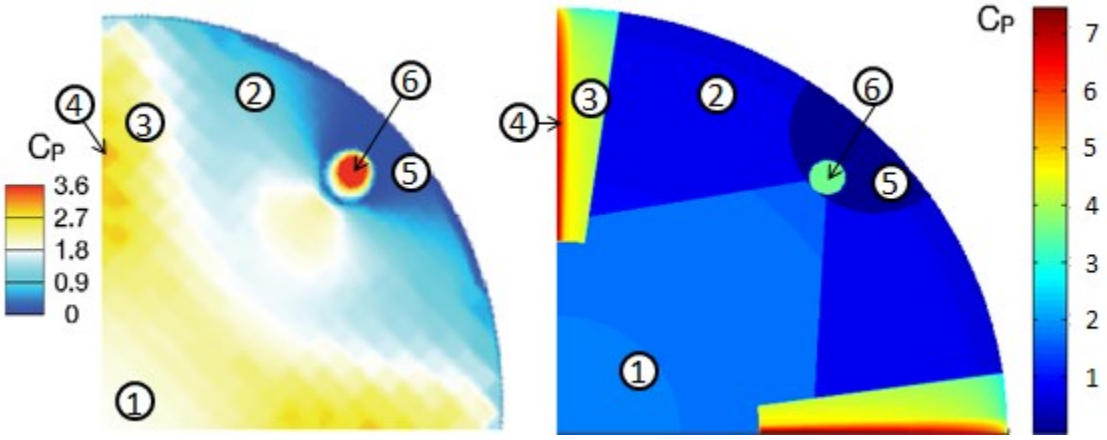

(a) CFD [19] (b) Drag Model

Figure 3.10: Definition of flow regions for drag coefficient model

While the flow in SRP systems is defined primarily by the rocket plumes, free stream Mach number, angle of attack, and the resulting shock structure, accurately modeling these phenomena requires detailed computational techniques. However, based upon images from past CFD studies, the pressure distribution on the surface of the aeroshell exhibits similar

patterns of pressure at zero angle of attack due to the six flow regions listed above. This pattern exists for similar shock structures, which in turn are due to thrust coefficients between 1 and 1.5, and free stream Mach numbers greater than 2. By calculating the flow pressures expected in each region of the aeroshell for a given Mach number and estimating the relative size of each region of flow from CFD results in literature, a simple pressure (and thus inviscid drag) model has been created for peripheral nozzle SRP flows.

For each of the flow regions (besides the nozzle exit and separated flow regions), the stagnation pressure to atmospheric pressure ratio is calculated as a function of the appropriate shock type and interactions. The analytic methods for finding the pressure ratios are given in Section 3.2.2. The nozzle flow exit pressure is dependent on thrust level, mass flow rate, and nozzle design, which is not considered in this work. The nozzle exit pressure ratio was chosen to be the same as the pressure used in the reference CFD pressure distribution (Figure 3.10) to enable simple comparisons between the two models. However, since the nozzle exit area is small and the pressure ratio is on the same order of magnitude as the other flow regions, the exact pressure distribution of the nozzle exit does not have a large impact on the capsule drag. The separated region (region 5) occurs due to the nozzle shielding that area of the aeroshell from the free stream flow. The flow pressure in region 5 is assumed to be equal to static atmospheric pressure. The effect of regions will be discussed in Section 3.3.5.

During model development, it was noticed that there the region near the aeroshell periphery (region 2 in Figure 3.10) where the pressure shown in CFD results from literature was significantly less than expected based on the nominal capsule flow structure based on a single normal bow shock. This decrease in pressure is theorized to be the result of an increase in velocity arising from the flow accelerating around the nozzle flow (which acts as a

blockage). This effect could be tested by applying mass conservation to the flow field; however this requires knowledge of the shock structure which is out of the scope of this work. In the absence of an analytic model for the flow acceleration in this region, an empirical factor was applied to the expected pressure distribution to estimate of the pressure in this region (region 2).

The back face pressure is not calculated as a function of position. Previous SRP modeling and test efforts have generally neglected detailed modeling or flight vehicle-like geometry for the backshell. This region is low-pressure, separated flow. For this model, the average pressure on the back face is user-defined to be somewhere between vacuum and equal to atmospheric pressure. This choice is a result of commonly observed pressures on nominal 70° sphere-cone aeroshells, and the pressures are assumed to be similar for SRP systems. The effect of the average pressure chosen in this region on the capsule drag is discussed in Section 3.3.5.

The value of the specific heat ratio γ used for the flow calculations in each region can affect the accuracy of the model results. The value of the stagnation pressure to free stream pressure ratio for two different shock structures is shown in Figure 3.11 for 3 different scenarios. The dotted and dashed lines indicate pressure ratios where the specific heat ratio has been calculated as a function of temperature using the minimum and maximum temperatures in the Martian atmosphere as initial conditions. The solid lines show the use of specified values of γ in calculating the pressure ratios. The difference in pressure ratio between the different curves becomes more pronounced at higher Mach numbers, and so subsections of the plot are shown for clarity.

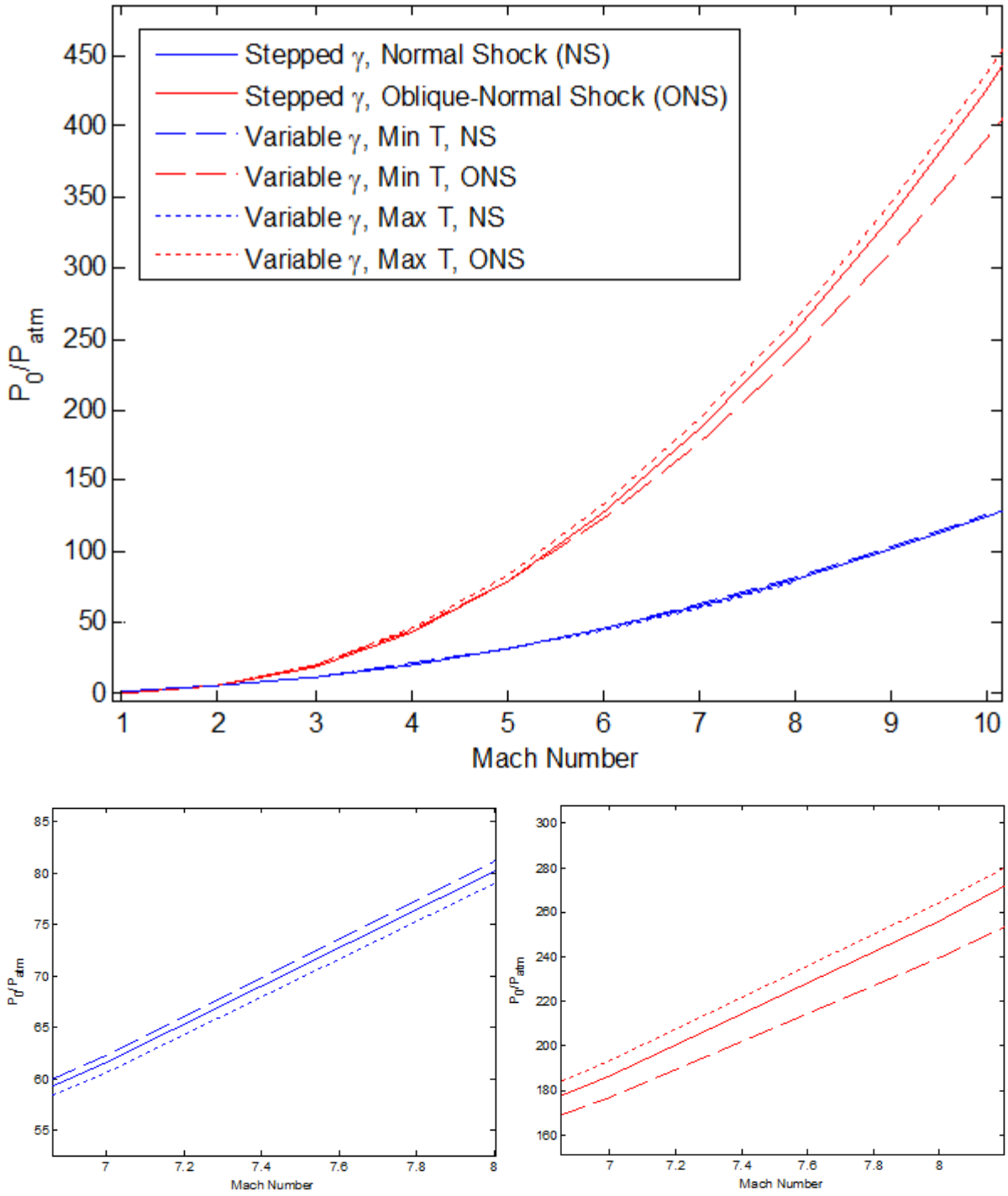

Figure 3.11: Effect of specific heat ratio on shock cascade pressure ratios

Since the flow is subsonic behind a normal shock wave, the stagnation pressure is similar order of magnitude as the static pressure, and the value of γ does not significantly alter the isentropic pressure ratio. The free stream temperature will alter the pressure ratio

across the normal shock, but this effect is limited to approximately 3% for the temperature range used. These factors allow a single value of $\gamma = 1.35$ to be used for both the shock and isentropic relations for a normal shock cascade. This value of γ matches the dotted and dashed line curves in Figure 3.11 well, and reduces the computation time of the drag model as the value of γ does not have to be computed.

For multiple shock cascades, the value of γ has a more significant effect on the pressure ratio across the final normal shock. The flow across the first normal shock increases the local static temperature, which decreases γ. This in turn has a significant effect on the pressure ratio across the normal shock. Using a single value of γ across the entire shock introduces more significant errors in computing the pressure ratio across the shock structure. To remedy this, a predefined 'stepped' function for γ through the shock structure can be applied to the problem. Two values for the specific heat ratio are prescribed, one for the first oblique shock ($\gamma = 1.35$) and a second for the normal shock and isentropic relations ($\gamma=1.17$). This method captures the most significant change in γ for the shock structure without the need for directly computing γ at the expense of computation time. The same approach is used for the oblique-oblique-normal shock cascade, where the second value of γ is used for the second oblique shock, the normal shock and the isentropic flow. Three values of the specific heat ratio are unnecessary for this case, since γ does not increase significantly at higher temperatures past the second value.

The free stream temperature has a larger effect on the pressure ratio range for the oblique-normal shock cascade than for the normal shock (approximately 10% at $M_\infty = 8$). The two stepped γ approach is shown to fall within these bounds in Figure 3.11. While the effect of the free stream temperature is larger for this shock cascade, the overall contribution

to the drag coefficient of the aeroshell is not as drastically affected, since the oblique-normal shock cascade flow only appears on a smaller portion of the aeroshell face. The sensitivity of the pressure model to the chosen values of γ is discussed in Section 3.3.5. In addition, while the variability in the calculated pressure ratios increases with the free stream Mach number. However, at very high Mach numbers, the dynamic pressure of the flow around the capsule is very small due to low atmospheric density. As a result, the overall drag force is low for all reasonable values of γ, and so the trajectory is minimally altered by this effect. This sensitivity will be discussed in Section 4.2.

3.3.2 Model Assembly

After the flow pressure ratio in each region P_0/P_{atm} has been calculated, the local pressure ratio P/P_{atm} must be calculated, since the flow is not full stagnated (except at the nose). The velocity and pressure behavior between the shock structures and capsule surface are complex due to turbulence and mixing of flows between different flow regions. This prevents simplistic analysis of the pressure distribution as a function of radius or angle within a given flow region. In the absence of such a model, the pressure variation as a function of radius is assumed to follow the same distribution as the nominal capsule flow structure described in Section 3.2.3. The standard geometry used for all 4-nozzle peripheral SRP configurations in this thesis is shown in Table 3.2 below, where the length scales have been normalized by the aeroshell radius. However, the geometry can be altered to accommodate alternate geometry configurations in the drag model, without changing the method in which the flow pressures are computed.

Table 3.2: Standard model geometry

Parameter	Value
Aeroshell Radius	1
Cone Half Angle	70°
Nose Radius	0.25
Nozzle Exit Radius	0.04
Nozzle Placement Radius	0.85

Once the pressure ratio for all flow regions has been calculated, the pressure is assigned at each location on a grid. The grid is a projection of the aeroshell face onto the plane normal to the axis of symmetry, resulting in a circular domain. A polar coordinate system is used, with the origin at the center of the capsule face. The capsule radius has been normalized to 1. Since a 4-nozzle peripheral SRP system is the primary model focus, the model is assumed to be symmetric in each quadrant. To reduce computation time, the pressures are only calculated for one quadrant of the aeroshell (for angles between 0° and 90°). To aid in comparing results of the pressure model to data in literature, the pressure coefficient is also calculated at each point.

The resulting grid of pressure ratio data is integrated according to Eqn. 3.13 to obtain the coefficient of drag. This integration is performed using the trapezoidal method over the domain of one quadrant of the aeroshell. The grid on which the pressure model is evaluated uses equally spaced points in the angular direction. The radial points are linearly spaced, broken up into 3 sections with the spacing adjusted so that the area in between grid points is similar across the entire domain.

3.3.3 Model Results

The completed drag model was evaluated for a range of Mach numbers from 2 to 20, for both the standard SRP flow configuration and the expected pressure distribution when the SRP thrusters are not operating. The computed data is shown in Figure 3.12.

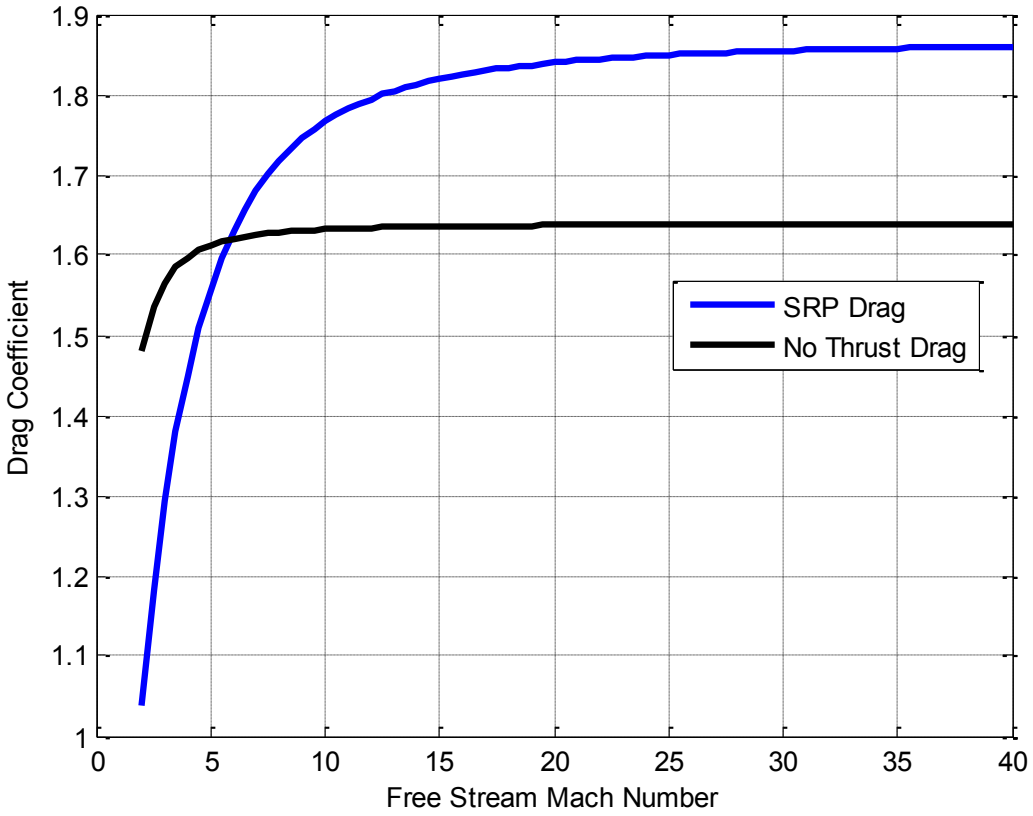

Figure 3.12: Drag coefficient modeling results

As expected, the model shows an increasing drag coefficient as free stream Mach number increases. There is a 'break-even' point at approximately $M_\infty = 6$ where the drag coefficient with SRP activated is equal to the drag coefficient of the aeroshell without thrust. However, Figure 3.12 only shows the drag coefficient, and does not take into account the thrust force applied by the SRP. The total axial force coefficient for the SRP case is the sum of the drag coefficient and the thrust coefficient (nominally assumed to be 1.0). Therefore,

the total axial coefficient for the SRP case is higher than the no-thrust axial coefficient (which is equal to the no-thrust drag coefficient) at all Mach numbers computed.

The SRP drag coefficient increases sharply with Mach number until approximately Mach 8 – 10. This drastic effect has not been captured by many previous studies, which assume that the drag coefficient for peripheral-nozzle SRP is predominantly a function of the thrust coefficient and is constant with free stream Mach number. However, Figure 3.12 shows that this drag coefficient can increase by 14% when operated at hypersonic Mach numbers.

A sample of the drag model pressure coefficient distribution for 4 free stream Mach numbers is shown in Figure 3.13.

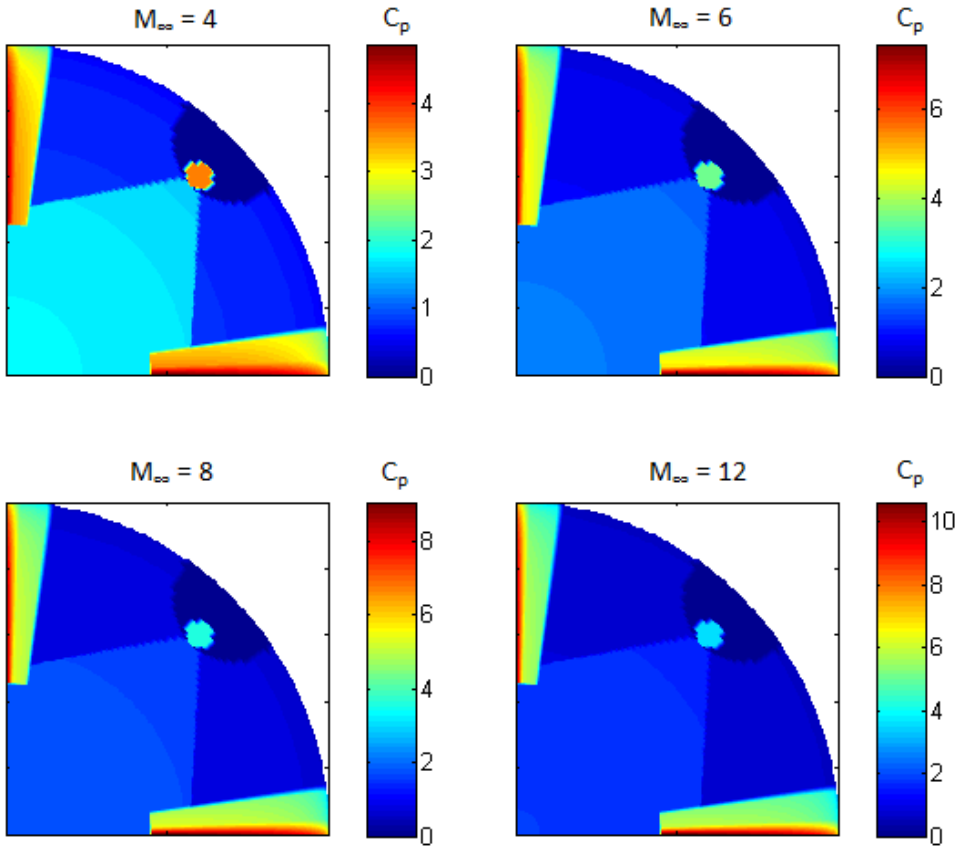

Figure 3.13: Drag model representative results

The geometry of the six flow regions are kept constant with Mach number. Therefore, the only changes that occur in the model with a change in Mach number are the pressures in the flow regions. Figure 3.13 shows that as the free stream Mach number, the pressure in the shock cascade regions (regions 3 and 4) increases at a higher rate than the flow that passes only through the normal shock. This is the dominant behavior of the surface pressure distribution that this drag model was developed to capture.

3.3.4 Data Validation

Two data validation studies were performed on the completed drag model. The first was a grid resolution study to establish the density of integration points for evaluating the pressure coefficient for sufficient accuracy without resulting in an unnecessarily long computation time. The second study compares the results of the drag model to the available data sources on peripheral-nozzle SRP. While not an absolute indicator of accuracy, this validation demonstrates the similar performance to CFD simulations and wind tunnel data.

To evaluate the grid resolution required, a grid sensitivity test was performed. This test calculated the drag coefficient for the vehicle for two extremely fine grid spacings which defined the reference drag coefficient value. The grid size was then decreased incrementally to a very coarse grid size and the drag coefficient was calculated for each grid. The resulting difference to the fine grid drag coefficient provides a reasonable estimate of the integration error. The results of this test performed for a free stream Mach number of 6 and standard geometry are shown in Figure 3.14.

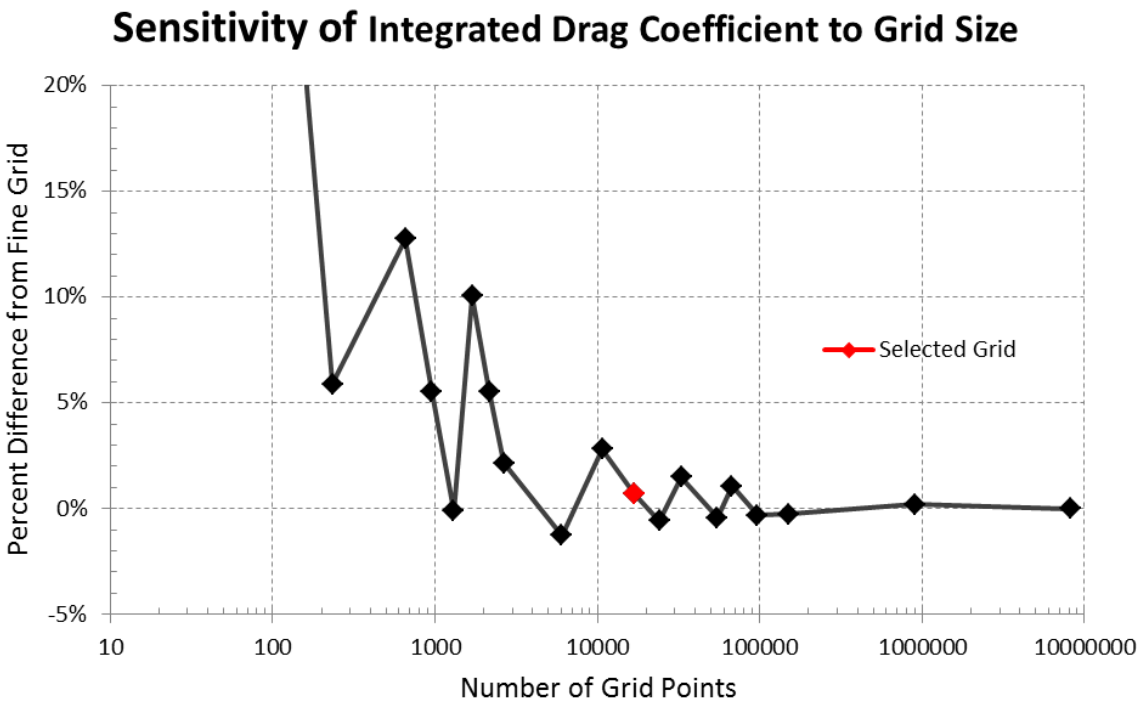

Figure 3.14: Grid sensitivity test

The percentage difference shows some erratic behavior, often changing slope and jumping significantly between grids of similar size. Since the pressure distribution in the model jumps discontinuously at several locations, this behavior is likely a result of how well the grid points align with the discontinuities between pressure regions. However, for grid sizes greater than approximately 15,000 points, the error does not exceed a relative difference of 1.5%. This level of error is acceptable for this simplified drag model, as the uncertainties in the model parameters and assumptions will result in larger errors. As a result, this grid size was chosen to minimize the computation time for the model while still providing sufficient accuracy. Since the size and location of each flow region is defined and assumed to be independent of Mach number, the alignment of the grid with the location of the discontinuities will not change for the chose grid resolution, and so no increase in integration error is expected for other Mach numbers.

To validate the coefficient of drag values calculated by the drag model, a list of C_D values from previous wind tunnel testing and CFD simulations was assembled. A large number of previous studies into peripheral nozzle flow structures do not compute the drag coefficient as their main focus is validating the flow structure in front of the aeroshell between CFD codes or with test data. The drag model developed in this work does not predict the flow structure; it only calculates the resulting pressure distribution from an assumed flow structure. Even fewer studies have mapped the aeroshell pressure distribution, and so direct comparison of the flow regions outside of the original data source [19] is not feasible.

The data sources listed below use either 3 or 4 nozzles in a peripheral nozzle configuration. The flow regions in the pressure model are matched to a 4-nozzle SRP configuration. These flow regions are not altered, except in the case of moving the nozzle location (the default nozzle location is at a radius of 80% of the aeroshell radius). The drag model automatically resizes the recirculation zone to match the nozzle location. The model is also altered to match the cone angle (for the 60° cone tested by Jarvinen and Adams [15]). The value of the drag coefficient is otherwise only a function of free stream Mach number. The pressure model is not calculated as a function of the thrust coefficient, even though the shock structure is a function of the thrust coefficient. At present, the flow structure is assumed to be caused by the given thrust coefficient; although as the data shows the thrust coefficient will largely impact the drag coefficient of the vehicle. Unless otherwise indicated, the test data used a thrust coefficient of 1.0.

While the pressure distribution on the back shell of the vehicle is significant in measuring the drag coefficient, the pressure on this region is generally not known because it

was not simulated in detail with CFD, or because of the wind tunnel test equipment attached to the aeroshell in this region. The pressure model assumes 25% of the ambient atmospheric pressure for the backshell pressure, which is chosen to approximate the available data. Finally, the comparisons to these data sources occur for a constant specific heat ratio of 1.4 (for calorically perfect air). Table 3.3 provides the test data conditions and results and the predicted drag coefficient from the pressure model outlined in this chapter.

Table 3.3: Modeled drag coefficient comparison to test data

M_∞	Method	Source	Source C_D	Predicted C_D	% Difference
4-Nozzle Configurations					
2	CFD	[19]	1.092	1.295	18.59%
4	CFD	[19]	1.561	1.494	-4.30%
6	CFD	[19]	1.630	1.628	-0.12%
12	CFD / Tunnel	[23]	1.450 * †	1.327	-8.47%
3-Nozzle Configurations					
2	Wind Tunnel	[15]	1.2 ⌂	0.993	-17.23%
2	Wind Tunnel	[15]	0.7 ⌂ †	0.993	41.89%
2	CFD	[19]	1.345	1.295	-3.71%
4	CFD	[19]	1.633	1.494	-8.56%
6	CFD	[19]	1.625	1.628	0.22%
8	CFD	[19]	1.543	1.700	10.17%

* Nozzles placed at a radius of 55% of the aeroshell diameter.
⌂ Nozzles places at a radius of 80% of the aeroshell diameter, cone half angle of 60°.
† Thrust coefficient of 1.5.

The data in Table 3.3 does not follow a clear, single trend, and so the accuracy of the model cannot be immediately determined. However, there are several key points to note. The most prevalent data source occurs for a free stream Mach number of 2. However, the operation of SRP in this regime has been shown to produce highly variable results in the drag coefficient and aeroshell pressure distribution. This is due to the large bow shock standoff

distance and small SRP jet shock penetration. The resulting shock structure is inconsistent between the available data sources, and so the flow region sizes and thus the resulting drag coefficient is difficult to determine. The thrust coefficient also plays a significant role in determining the drag coefficient for these flows, as illustrated by the 3-nozzle wind tunnel tests at Mach 2. Since the data for a Mach number of 2 is inconclusive, the pressure model will not be utilized for Mach numbers below 4.

Excluding the Mach 2 data, the pressure model developed in this thesis matches the available data to within 10% for all Mach numbers and aeroshell geometry configurations. While this is a positive result in establishing the utility of the simplified model presented here, the number of data points available is small and illustrates the need for more rigorous testing and analysis across the relevant parameter space to provide data that models such as this can be calibrated against. It is also important to note that the data sources listed above cannot be used as truth values, since each have errors induced by their test method. For example, the pressure in the separated flow region on the back face of the vehicle can have a significant effect on the drag coefficient of the vehicle; however past research in SRP flows has not investigated this flow region in detail. Since the accuracy of the wind tunnel testing and CFD modeling of SRP flows is still an active area of research, further tuning the drag model developed in this thesis provides diminishing returns in accuracy in the systems-level evaluation of the technology.

3.3.5 Model Sensitivity Analysis

To further characterize the drag model developed in this thesis, a sensitivity analysis was performed to several input parameters which have been estimated from CFD results. These results allow a more detailed understanding of how each input variable affects the

computed drag coefficient. To perform the sensitivity analyses, a single variable was perturbed from the reference value (listed in Table 3.4), and the resulting drag coefficient recorded across a range of Mach numbers. A multivariable sensitivity analysis with two or more empirical parameters was not performed.

Table 3.4: Baseline parameter values for sensitivity studies

Parameter	Value
γ_1 (free stream)	1.35
γ_2 (behind oblique shocks)	1.17
Backshell Pressure	0.25 P_{atm}
Oblique Wave Angle β_w	40°

3.3.5.1 Specific Heat Ratio

As described in Section 3.3.1, two values of the specific ratio were used to better approximate the changing value with the increase in temperature across a shock. Figure 3.15 and shows the variation in drag coefficient for various values of the specific heat ratio.

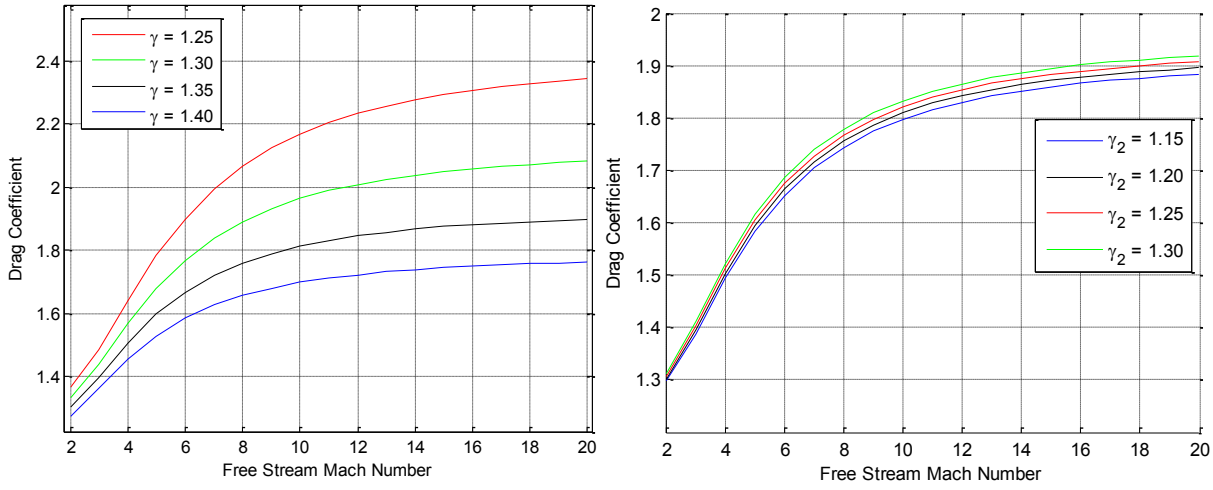

(a) γ_1 sensitivity (b) γ_2 sensitivity

Figure 3.15: C_D sensitivity to γ_1 and γ_2

Figure 3.15 (a) shows that the drag coefficient is sensitive to the value of γ_1, the free stream specific heat ratio. The value of γ_1 is dictated by the free stream temperature. For the Martian atmosphere, the resulting values of γ_1 could be in between 1.3 and 1.4, which results in a 10-15% variance in drag coefficient. The difference in drag coefficient is larger at higher Mach numbers. The atmospheric temperature is not constant, and so an appropriate value of γ_1 was chosen to be in the middle of this range, $\gamma_1 = 1.35$. This represents an average value for the drag coefficient based on the temperature profile in the atmosphere, without requiring the drag coefficient to be recalculated at each time step in the trajectory analysis.

Figure 3.15 (b) shows that the drag coefficient is much less sensitive to the value of γ_2 (the specific heat ratio behind shocks) than γ_1. While Section 3.2.1 shows that it is necessary to add in a second specific heat ratio value for the oblique shock cascades, the value of γ in this region does not have a significant impact on the drag coefficient, so long as it is in the range of γ for CO_2 at high temperatures. The variance in drag coefficient is less than 5% over the range of relevant specific heat values.

3.3.5.2 Backshell Pressure

The flow behind the entry vehicle is a separated flow region with low pressure and velocities. The velocity and pressure distributions are difficult to predict, and this modeling is a current area of research. However, the backshell pressure distribution is simply modeled by an average value for the purposes of this work. The backshell pressure is generally less than the static atmospheric pressure, since the flow is separated.

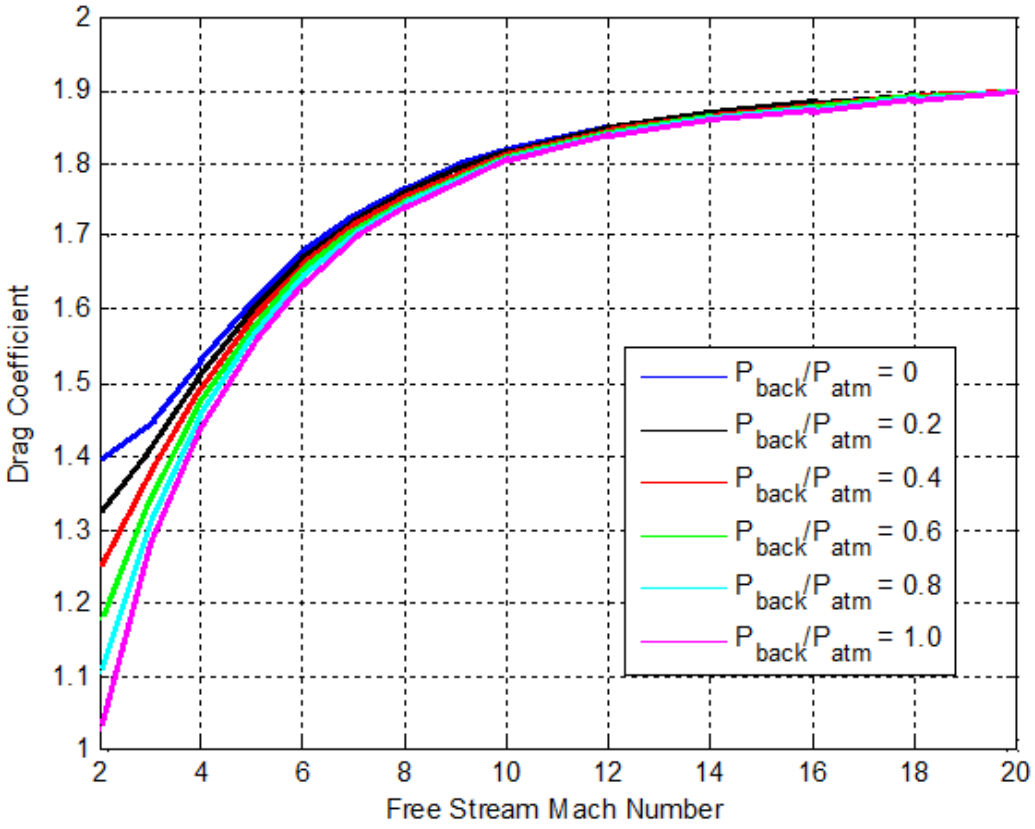

Figure 3.16: C_D sensitivity to backshell pressure ratio

Figure 3.16 shows that the backshell pressure ratio has the largest effect on the drag coefficient at low Mach numbers. At high Mach numbers, the drag coefficient curves converge. This behavior can be explained from the drag coefficient integration, Eqn. 3.13. The backshell pressure ratio is a prescribed constant, and so numerator of the second term is constant. However, the denominator of that term is proportional to M^2, and so at high Mach numbers, the second term (and thus the contribution of the backshell pressure ratio to the drag coefficient) becomes negligible. At low Mach numbers, the drag coefficient can vary by 35%. This effect may also be a contributing factor to the high variability in reported drag coefficients at Mach 2 for the reference data in Table 3.3. At a Mach number of 6 the range in drag coefficients has decreased to approximately 25%.

The large effect of the backshell pressure on the drag coefficient presents an interesting area for further work. The use of flow control mechanisms to decrease the pressure in the separated flow region on the backshell. It may be possible to use the SRP exhaust to add radially directed momentum to the flow to decrease the pressure in the aft separation region. There are likely other flow control technologies that could be better applied to this problem as well.

3.3.5.3 Oblique Shock Wave Angle

The oblique shock wave angle was determined by measuring the approximate linearized angle of the SRP jet plume shocks from Schlieren photography or CFD images of local Mach number. The factors impacting this shock wave angle are not clear, but may include thrust coefficient, nozzle exit pressure, and free stream Mach number. To determine the effect of this uncertainty, the oblique shock angle was varied from 20° to 70°, even though the typical values measured fell in the range of 30°-50°. While the angle of the oblique waves impacts the size of the various flow regions, the flow region sizes were kept constant for this analysis.

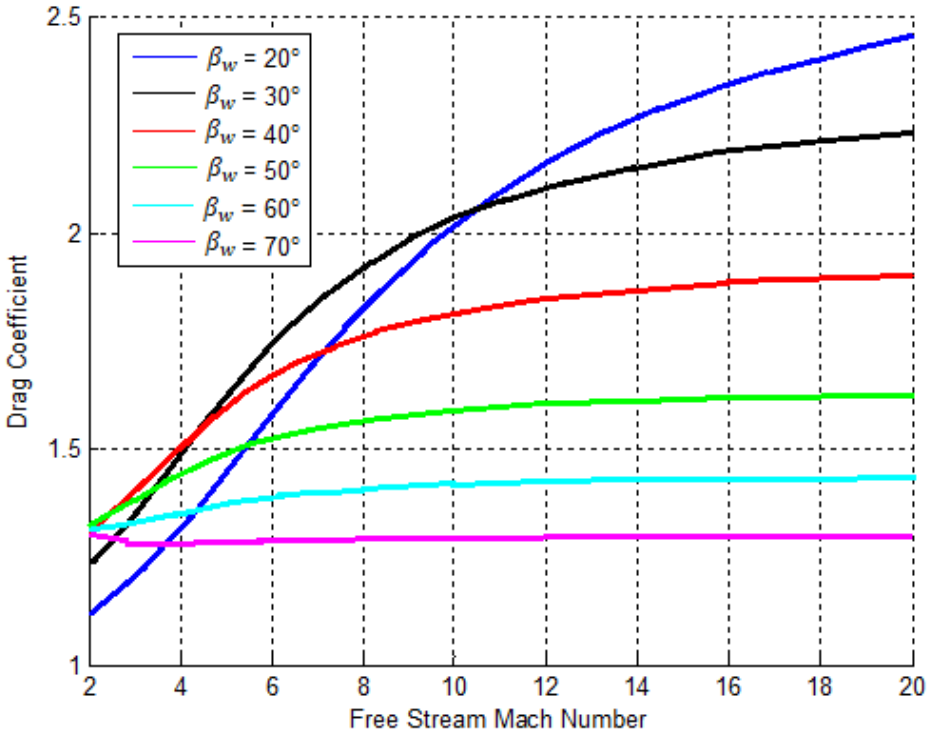

Figure 3.17: C_D sensitivity to oblique shock angle

Figure 3.17 shows the drag coefficient is highly sensitive to the angle of the oblique shocks formed by the SRP plumes, causing over 100% variation at high Mach numbers. Even restricting the shock angle to the range of 30°-50° as measured from literature sources, the drag coefficient can vary by 35% at high Mach numbers. This effect is not as pronounced at lower Mach numbers, but may still contribute to the difference in drag coefficients between data sources between Mach 2 and 12. Based on the available images from literature, a shock wave angle of 40° represents the mean shape of the shock structures formed by the SRP plumes. However, Figure 3.17 clearly illustrates the need for more detailed modeling and understanding of the shape of the peripheral-nozzle SRP shock structure in evaluating the drag coefficient. This information also suggests that the drag coefficient could potentially be increased if the SRP exhaust plumes can be used to control the oblique shock wave angle.

3.3.5.4 Flow Region Sizing

The size of the six flow regions described in Section 3.3.1 were varied in terms of the percentage change in area to determine the relative effect of the flow region sizing on the drag coefficient. The first flow region size varied was the flow through the normal shock (region 1), shown in Figure 3.18.

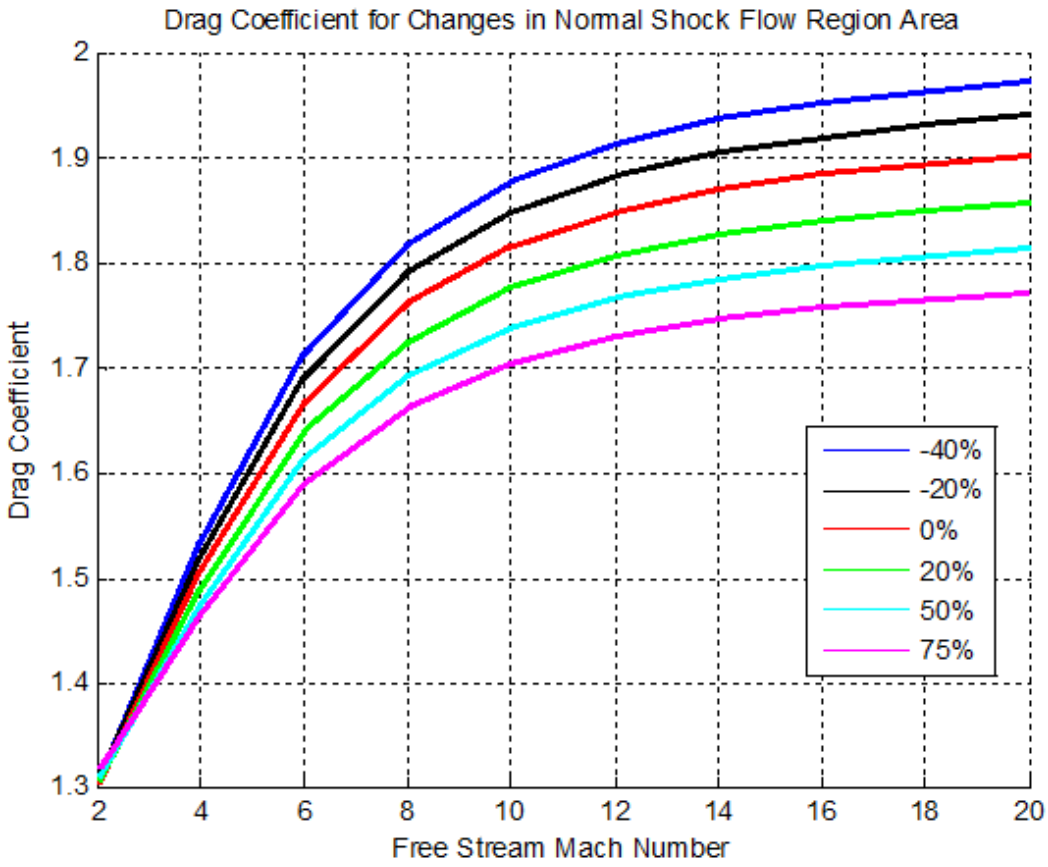

Figure 3.18: C_D sensitivity to flow region 1 size

The change in drag coefficient increases with free stream Mach number. This is to be expected, since increase the area of flow through the normal shock decreases the flow area passing through the oblique shock cascades, which are the regions that increase the drag coefficient the most at high Mach numbers. However, changing the normal flow region size by ± 20° only changes the drag coefficient by a maximum of 2.5%.

The impact of the accelerated flow region around the SRP nozzle exit (region 2) is shown in Figure 3.19.

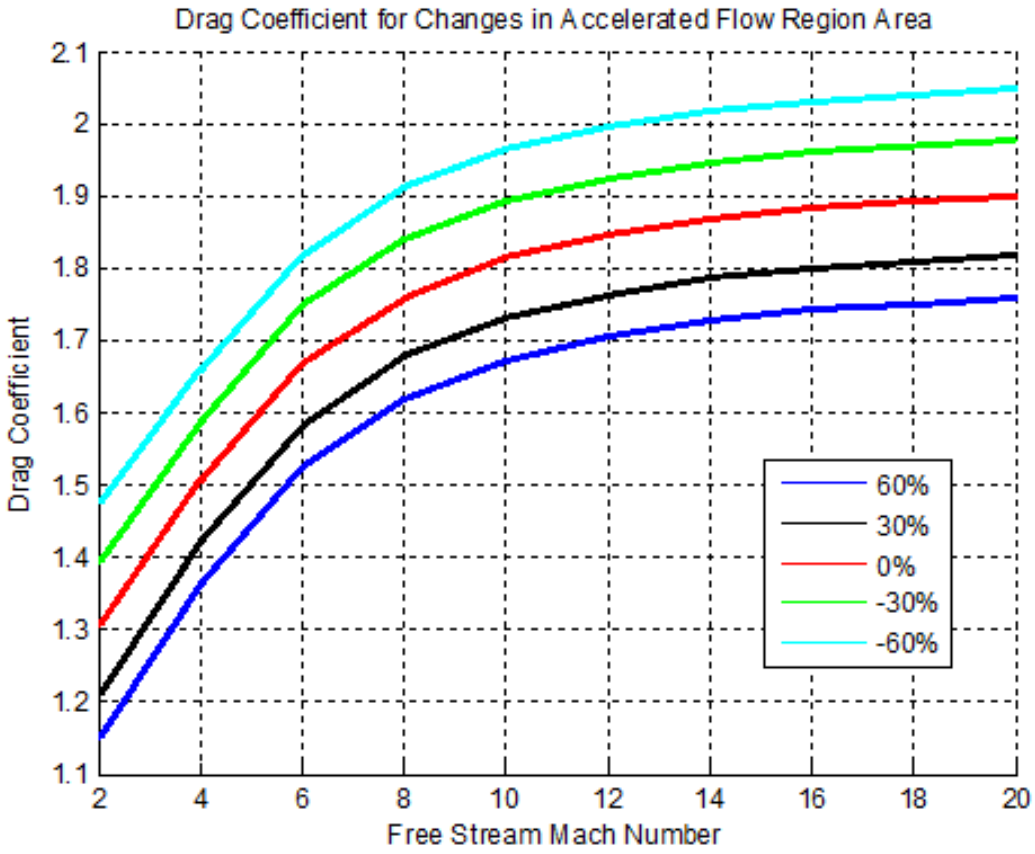

Figure 3.19: C_D sensitivity to flow region 2

Unlike the other sensitivity plots of the drag coefficient to flow region area, the size of flow region 2 is approximately constant with Mach number. The change in drag coefficient can be interpreted either as a change in area for this flow region or the change in assumed pressure as a function of the nominal pressure distribution in this region (for no SRP activation). This is because the pressure in this region was empirically set to be a set percentage (50%) of the pressure in the nominal flow case, as no analytic solution was obtainable. This result indicates that minimizing the flow blockage near the nozzle (through a

smaller nozzle exit diameter, for example) is desired since this would decrease the flow speed and increase the pressure in this region.

The sensitivity of the drag coefficient to the size of the flow region passing through an oblique-normal (ON) shock cascade is shown in Figure 3.20.

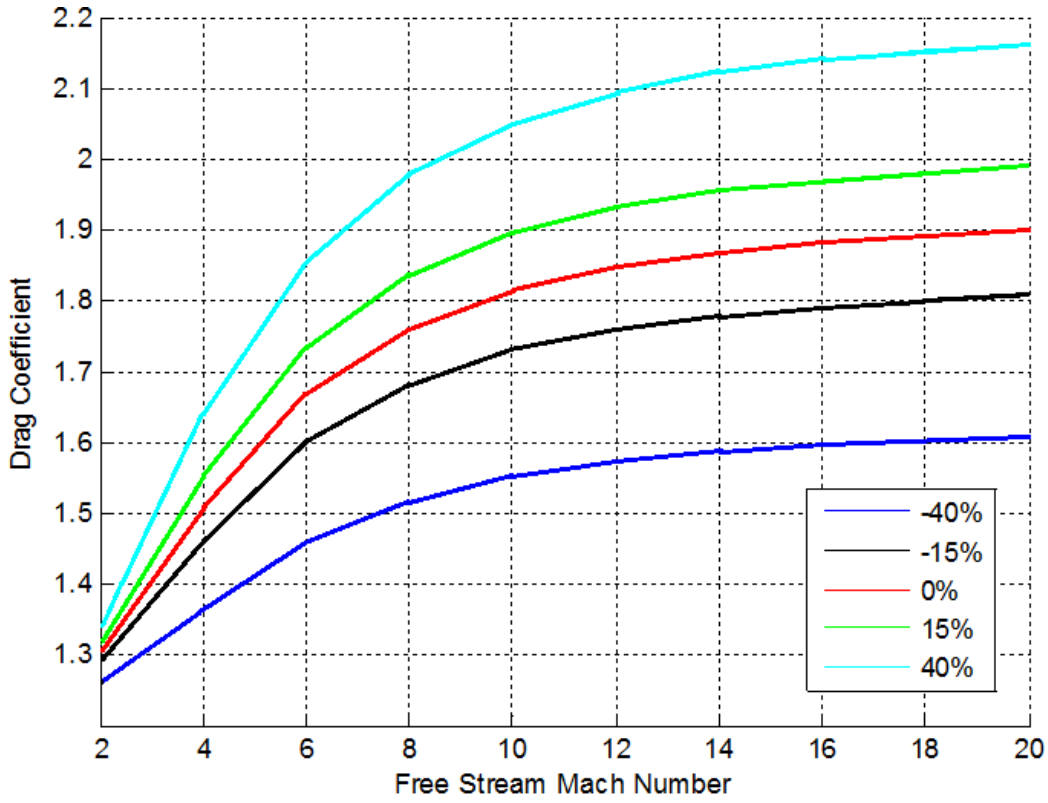

Figure 3.20: C_D sensitivity to flow region 3 size

The drag coefficient has been found to have a significant level of sensitivity to the size of the amount of flow passing through the ON shock cascade, with up to ±15% change in C_D for a ±40% change in area at high Mach numbers. Based on the data validation performed in Section 3.3.4, the area of the aeroshell influenced by this shock cascade appears to be approximately constant with Mach number. However, this sensitivity presents an area for future flow control investigations. If the size of the ON shock cascade interaction region can be increased (for example, by designing the SRP exhaust such that the jet shock

penetration distance from the aeroshell is increased), then the drag augmentation for SRP can be improved further.

The next flow region size studied was the oblique-oblique-normal (OON) shock cascade (region 4), shown in Figure 3.21.

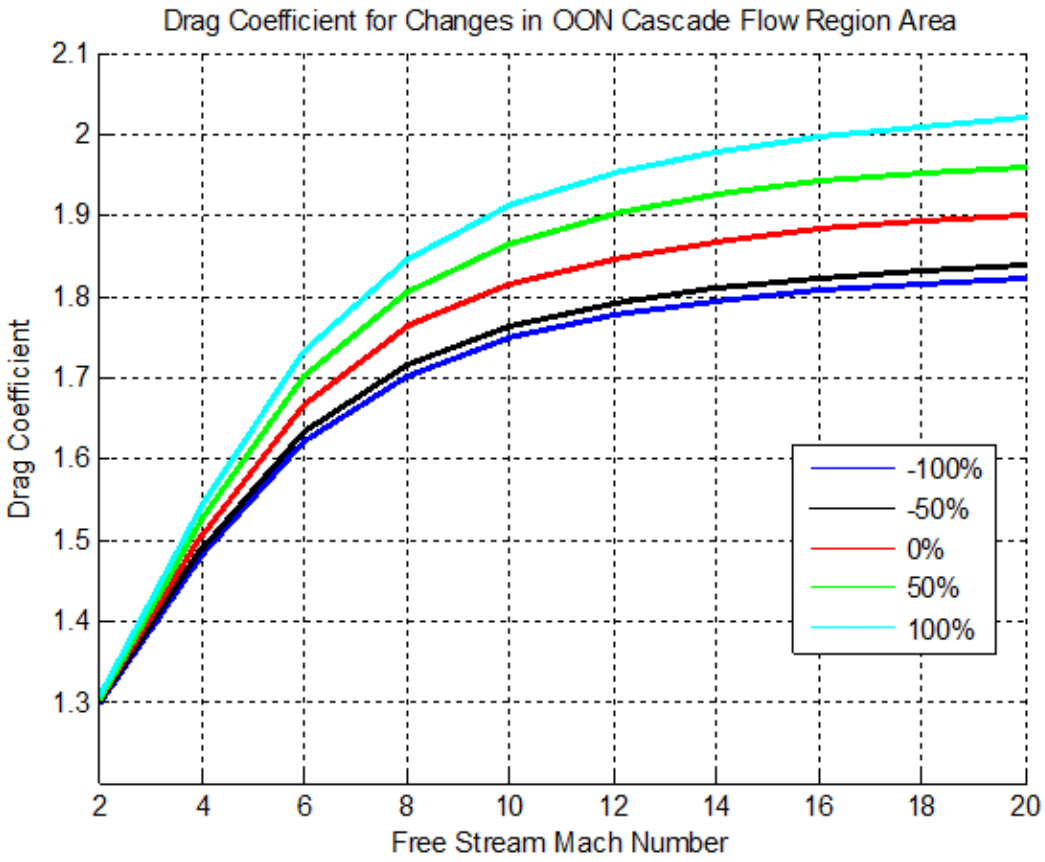

Figure 3.21: C_D sensitivity to flow region 4 size

The effect of changing the area of region 4 once again has the largest impact at high Mach numbers. Since the total pressure conservation is preserved much better for the OON shock cascade than for a normal shock, the area of the pressure distribution influenced by this shock structure can still have a significant impact on the drag coefficient. However, since this flow region is so small, the contribution to the overall drag coefficient is also small.

Completely removing this section only decreases the drag coefficient by less than 5% (at Mach 20).

The influence of the size of the separated flow region downstream of the SRP nozzle (region 5) is shown in Figure 3.22.

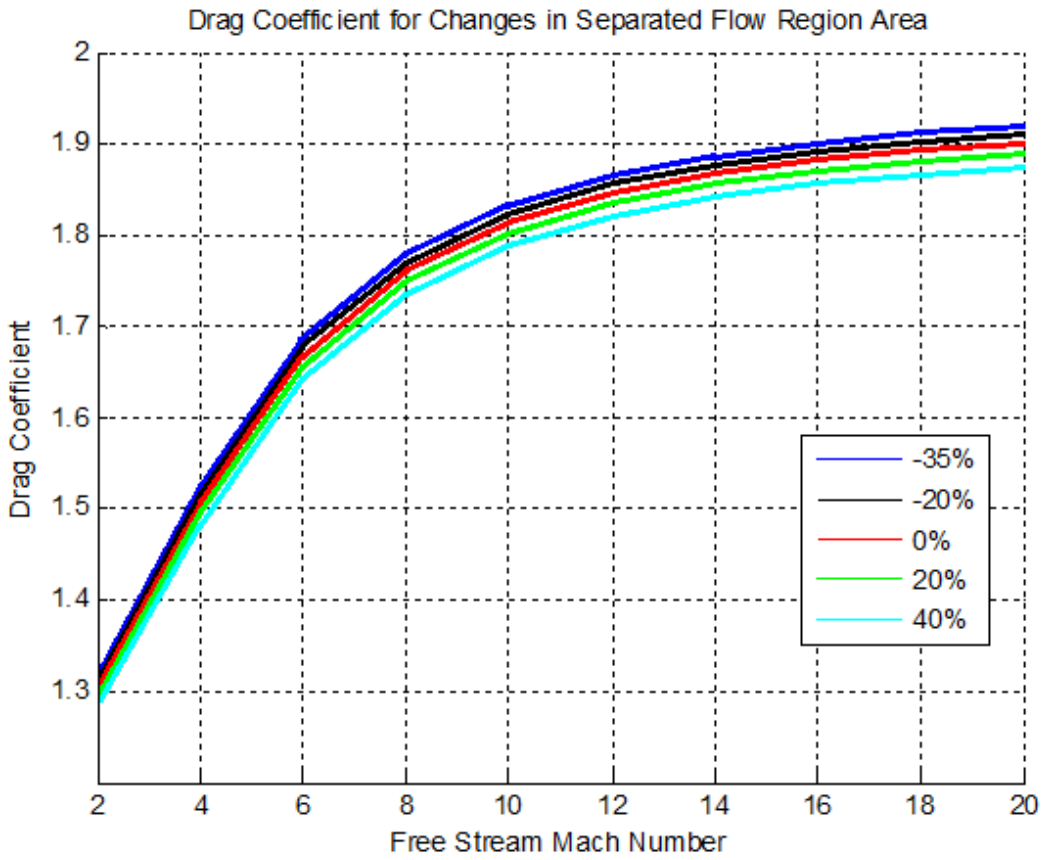

Figure 3.22: C_D sensitivity to flow region 5 size

The separated flow region has little influence on the drag coefficient for this geometry configuration where the SRP nozzles are placed near the periphery of the aeroshell. However, it is important to note that moving the nozzles inboard greatly increases the size of this separated flow region (by several hundred percent), which does cause a significant decrease in drag. This is the reason that some studies such as [23] have reported decreased drag even at high Mach numbers. If the vehicle configuration was modified to place the

nozzles closer to the aeroshell periphery, the drag coefficient should be increased as seen in this model.

The final flow region area modified was the nozzle exit. Modifying the exit pressure of the nozzle follows the same behavior as a corresponding percentage change in the nozzle exit area. The results are shown in Figure 3.23.

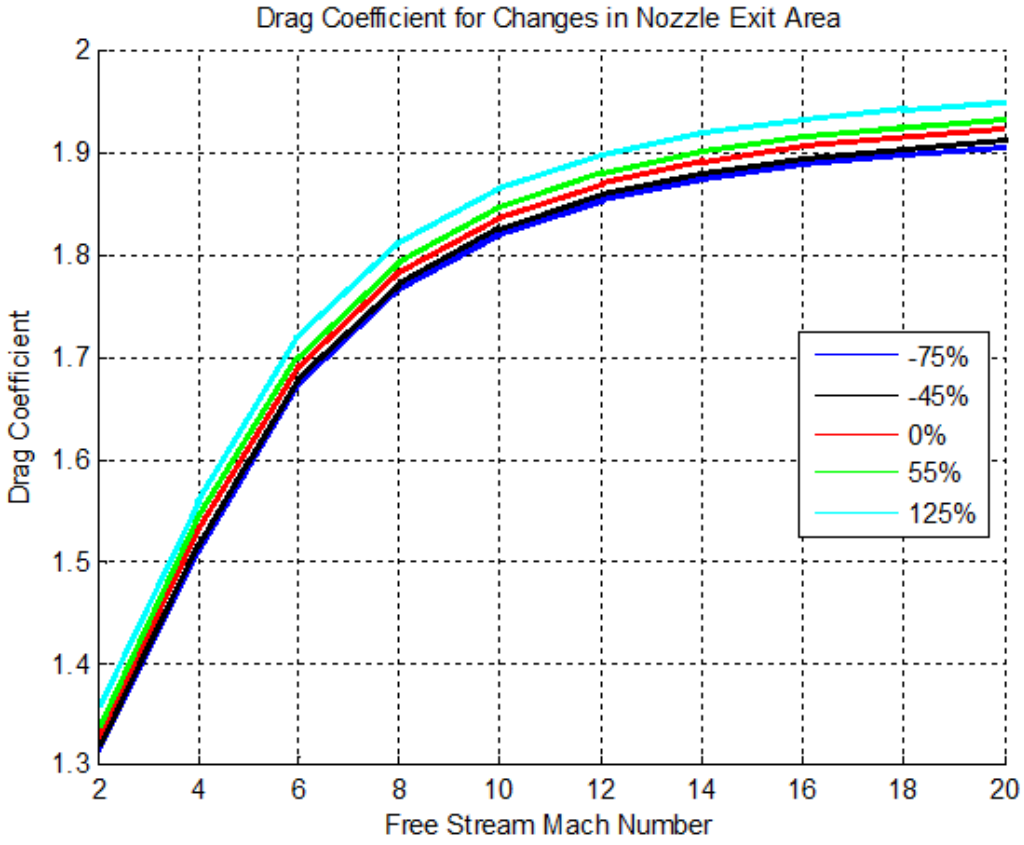

Figure 3.23: C_D sensitivity to flow region 6 size

Due to the small size of the nozzle compared to the overall aeroshell size, the relative change in area of the nozzle does not greatly affect the computed coefficient of drag. The nozzle can thus be tailored for an optimum expansion ratio independently of evaluating the drag on the vehicle. This expansion ratio may be tailored for a desired exit pressure, or it is

possible that an over- or under-expanded nozzle exit flow may be desired for the purposes of shaping the SRP shock structure.

3.4 Summary

This chapter presented the development and validation of a model of the drag coefficient for peripheral-nozzle SRP flows for a sphere cone aeroshell. The model captures the dominant flow behavior caused by the shape of the shock structure in front of the vehicle by calculating the pressures for six types of flow regions over the surface of the aeroshell. These pressures are calculated from the normal and oblique shock relations and isentropic flow relations. The size and location of the flow regions are determined by comparisons to CFD studies in literature. The pressures are integrated along with an assumed backshell pressure to obtain the drag coefficient as a function of Mach number. This model can be run quickly, on the order of minutes, to obtain an estimate of the drag coefficient for a vehicle using SRP for maximum drag augmentation that is appropriate for a systems level analysis. Chapter 4 will use the results of the drag model to analyze various trajectories of EDL vehicles using SRP.

The model was used to calculate the drag coefficient as a function of Mach number. The results show that the drag coefficient is less than the nominal (no SRP) drag coefficient for a 70° sphere-cone aeroshell for Mach numbers below 6. At higher Mach numbers, the drag coefficient can increase over the nominal case by 14% due to the increased pressure conservation through the oblique shock cascade structures.

The drag model was validated against available peripheral-nozzle CFD simulations and wind tunnel data available in literature. The SRP flow at a Mach number of 2 is not consistent, and so the drag model will not be used for a Mach number less than 4. For Mach

numbers greater than 4, the flow model was demonstrated to match the available empirical drag coefficient data to less than 10.2%. Since this model is only intended for use in a conceptual systems-level study, this level of error was deemed acceptable.

Since many of the drag model parameters were set based on CFD results, a sensitivity analysis was performed to compute the effect on the drag coefficient as a function of numerous parameters including the specific heat ratio of the atmosphere, backshell pressure, angle of the oblique SRP jet shocks, and the size of the six flow regions. Most parameters were found to cause a larger change in the drag coefficient at higher Mach numbers. While the drag coefficient was found to vary significantly with many parameters, the comparison to CFD and wind tunnel data over a range of Mach numbers suggests the parameters obtained from CFD results in the model were appropriately set. The drag model is most sensitive to the oblique shock angle and the size of the flow region passing through the oblique-normal shock cascade. These results further suggest that the drag coefficient of the vehicle can be increased by focusing on controlling the oblique shock cascade.

4 TRAJECTORY ANALYSIS

4.1 Entry and Descent Trajectories

The equations of motion for entry vehicles assume two types of forces acting on the object: gravitational forces and aerodynamic forces (including propulsive forces). The vehicle is assumed to be a single rigid body, and thus has 6 degrees of freedom (3 translational and 3 rotational). The 3 degree-of-freedom simplification can be applied for trajectories lying in a single plane. Cross-track velocities and angles are assumed to be zero.

For this study, the 6 degree-of-freedom model is not necessary. Only the velocity as a function of altitude is critical in determining the vehicle mass that can be landed on Mars, which can be computed using a 3 degree-of-freedom model. The deployable and retropropulsion flow fields are assumed to be axisymmetric, which renders the cross-track freedoms in the entry equations of motion unnecessary. This reduces the knowledge of the landing uncertainty ellipse which describes how accurately the vehicle can be landed at the target destination, to a 1-D in-track uncertainty. However, with this high-level systems study, the primary design goal is the payload mass that can be landed while the landing location uncertainty is secondary. Therefore, the 3 degree-of-freedom equations of motion will be used.

4.1.1 Equations of Motion

The primary state variables of the 3 degree-of-freedom entry equations are the velocity V, radial distance to the planet's center R (or alternatively the altitude h assuming a

spherical planet), and flight path angle γ_f. These equations are most simply derived in the 'wind axes' coordinate system, which is a rotating coordinate system aligned with the first axis along the velocity vector, the third axis placed in the trajectory plane [43].

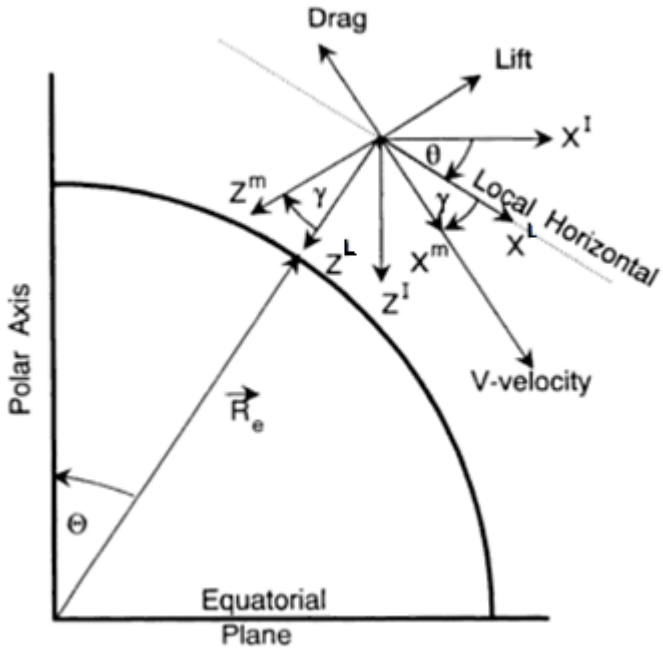

Figure 4.1: Inertial (I), Local (L), and Wind (m) axes (adapted from Ref. [43])

In Eqns. 4.1-4.3 below, a positive flight path angle is defined as the velocity vector below the local horizontal.

$$\frac{dV}{dt} = -\frac{F_A}{m} + g\,\sin(\gamma_f) \tag{4.1}$$

$$\frac{dR}{dt} = \frac{dh}{dt} = -V\,\sin(\gamma_f) \tag{4.2}$$

$$\frac{d\gamma}{dt} = \frac{1}{V}\left[-\frac{F_N}{m} + g\,\cos(\gamma)\right] - \frac{d\theta}{dt} \tag{4.3}$$

The differential term on the right hand side of Eqn. 4.3 can be converted into a single variable differential equation using the following definition for the time rate of change of the local azimuth θ.

$$\frac{d\theta}{dt} = \frac{V\cos(\gamma)}{R} \tag{4.4}$$

The importance of the ballistic parameter β (defined in Eqn. 1.1) can be shown by re-arranging Eqn. 4.1. Assuming no retropropulsion, the aerodynamic axial force F_A is simply equal to the vehicle drag D.

$$\frac{dV}{dt} = -\frac{\rho V^2}{2\beta} + g\sin(\gamma) \tag{4.5}$$

In Eqn. 4.5, the only vehicle parameter is the ballistic coefficient. All other parameters in the equation are based on the atmosphere or trajectory state. Therefore, if the mass of the EDL vehicle is increased, either the drag coefficient or drag area must increase or an additional deceleration force must be applied.

The gravitational acceleration g is modeled simply as a point mass gravity field which changes as a function of altitude.

$$g = \frac{\mu}{R^2} \tag{4.6}$$

A standard atmosphere model of Mars is also required for the trajectory model. A spherically symmetric planet is again assumed. The atmosphere properties (density, temperature, etc.) are required as functions of the altitude alone. The 2010 Mars Global Reference Atmospheric Model (Mars GRAM) [44] provides reference atmospheric data as a function of position and time. This data was averaged together to create a single reference atmosphere that provides density, temperature, and density as a function of altitude.

Numerical integration is employed to solve the trajectory equations of motion as functions of time. The equations of motion are coded in MATLAB and integrated with the `ode45` function. This utilizes a variable-step, explicit Runge-Kutta method to integrate the vehicle's trajectory state in time. The relative error tolerance was set to 10^{-6} to fix issues encountered during the discontinuous changes in operation states (e.g. initiation of SRP).

4.1.2 Entry Initial Conditions

Initial conditions must be provided to solve the trajectory equations of motion. Conditions for the altitude, flight path angle, azimuth, and relative velocity must be specified. All other variables in Eqns. 4.1-4.3 are calculated at each time step based on the current state and vehicle configuration.

The initial conditions for a Mars entry sequence can vary significantly depending on the mission parameters. The Viking spacecraft first entered orbit around Mars using a propulsive burn before the landing vehicle separated and entered the Martian atmosphere. The subsequent US landing vehicles have all employed direct entries from heliocentric orbit. Aerocapture and aerobraking concepts have also been proposed to allow the landing vehicle to enter the atmosphere from a Mars orbit without the need for propulsive orbit insertion, which would result in a lower spacecraft launch and cruise mass from Earth [5]. The design space for atmospheric entry has many options. To simplify results, a single baseline set of initial conditions based on the Mars Science Laboratory mission will be studied. However, the EDL performance reconstruction was not published at the time of analysis. Instead, the entry trajectory tool described in Section 4.1.1 was compared against entry data from the Mars Pathfinder mission. The entry initial conditions are shown in Table 4.1.

Table 4.1: Mars Pathfinder entry initial conditions [45]

Parameter	Value
Radial distance, R	3522.2 km
Flight path angle, γ_f	14.0614°
Velocity, V	7.2642 km/s
Azimuth, θ	253.1481°

The resulting EDL trajectory state history computed using both the Mars GRAM data and an exponential Mars atmosphere [46] was compared to reconstructed data from the Mars Pathfinder mission in Refs. [6, 45, 47]. The velocity versus altitude plot is most relevant to the drag-augmented SRP. Both these pieces of information are required to evaluate the dynamic pressure as a function of time which in turn determines the total magnitude of the thrust (and thus the propellant mass consumption) and the drag acting on the vehicle. This comparison is shown in Figure 4.2.

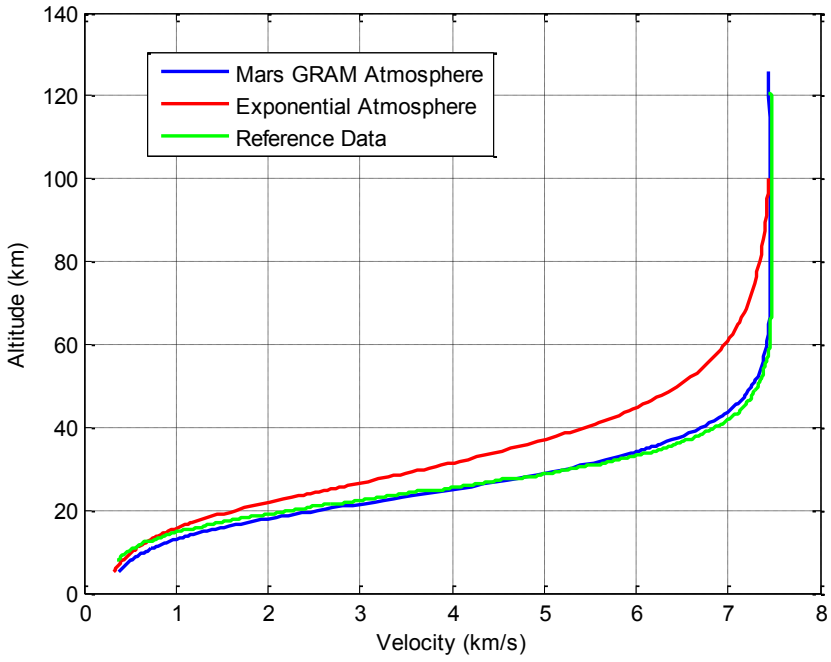

Figure 4.2: Validation of modeled Pathfinder velocity vs. altitude

Figure 4.2 shows good agreement between the Mars GRAM simulation result and the reference Pathfinder trajectory. The trajectory model begins to decelerate more at a higher altitude than the reference data, indicating a higher ballistic coefficient. The higher ballistic coefficient is likely due to a higher hypersonic drag coefficient being calculated using the nominal capsule flow model described in Section 3.2.3. However, Figure 4.2 indicates that the 3 DOF trajectory model is sufficiently accurate for this systems study.

The exponential Martian atmosphere results compare poorly with the reference data. The exponential atmosphere results under-predict the velocity at any given altitude by over 1.5 km/s for altitudes in the 30-35 km range. This effectively reduces the dynamic pressure at any given altitude which in turn underestimates the mass of propellant consumed. For the remainder of the trajectory simulations run in this work, the time and location averaged Mars GRAM atmospheric model will be used.

It is important to also verify the time scale of the EDL sequence. This was performed for the altitude and flight path angle history shown in Figure 4.3.

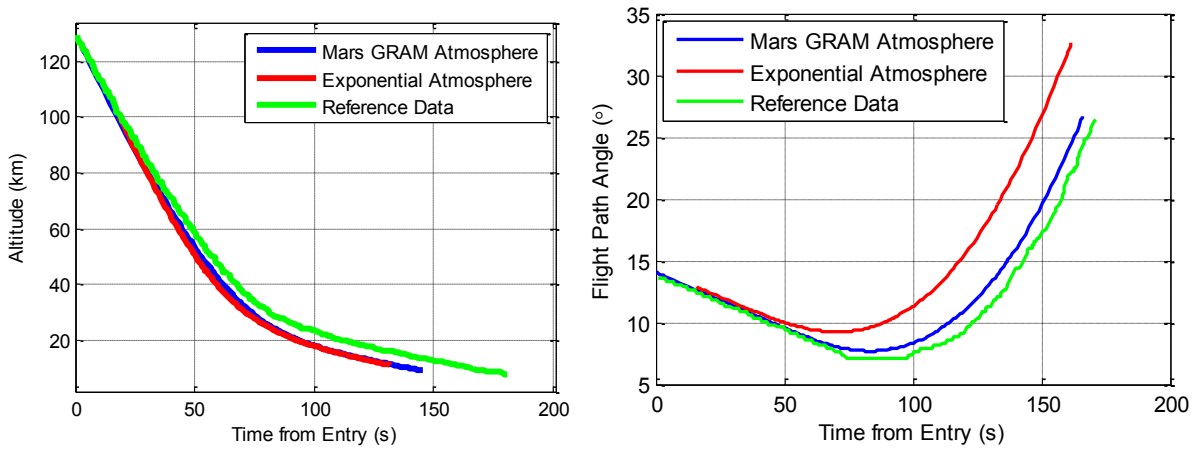

(a) Altitude history (b) Flight path angle history

Figure 4.3: Validation of modeled Pathfinder entry altitude and flight path angle histories

Figure 4.3(a) shows that the difference in the altitude history between the exponential atmosphere and the other results is less significant than the altitude-velocity plot in Figure 4.2. In fact, the vehicle reaches lower altitudes faster than the other models using the exponential atmosphere, even though its velocity at any given altitude is lower. This can be explained by examining the flight path angle history in Figure 4.3(b). If the entry is purely ballistic (i.e. no lift forces acting on the vehicle), then the rate of change in the flight path angle is solely a function of velocity and altitude. For the exponential atmosphere results, the vehicle decelerates more quickly, which increases the flight path angle. This means that the vehicle is moving in a more vertical direction, and so its altitude decreases quickly even while its velocity is lower. This same effect can be seen to a lesser extent between the Pathfinder reconstructed data to the Mars GRAM simulation results. While there are differences in the model results, they can be understood based on the trajectory equations of motion. The trends in Figure 4.3 for the 3 DOF trajectory model results exhibit the same behavior as the reconstructed Pathfinder data, with the differences in modeling parameters causing small errors. As a result of these comparisons, the 3 DOF model is deemed adequate for a systems-level analysis of trajectories utilizing SRP for the remainder of the chapter.

4.1.3 Criteria for Landing Sequence

This study is focused on the use of deceleration systems employed in the entry and descent phases of flight. The supersonic disk-gap-band parachute was used on Viking and all subsequent missions to set up the final descent and landing phases. However, the landing systems have varied greatly depending on mission requirements. Viking and Phoenix used retrorockets, the MPF and MER missions used airbag systems, and MSL used the ‘Skycrane’ system. The analysis and selection of these systems depends greatly on payload-specific

requirements. In addition, the velocity of the vehicle at this stage in the EDL sequence is low, and thus the primary concern in this flight phase is safe delivery to the desired landing site rather than further decelerating the payload. Therefore, this study will not consider various landing system architectures, and instead end the entry and descent trajectory integration at the initial conditions for the landing system to begin operation. The MSL parachute deployment design conditions are shown in Table 4.2.

Table 4.2: MSL parachute deployment conditions [10]

Parameter	Value
Mach number, M	≤ 2.2
Dynamic pressure, q_∞	≤ 850 Pa
Altitude, h	10 km

NASA announced further plans in late 2012 for a 2020 Mars rover, which would again utilize the 'Skycrane' landing system. The required conditions for the supersonic disk-gap-band parachute deployment as defined by the MSL mission will be used to evaluate the success or failure of the entry vehicle trajectory. The vehicle must decelerate to the acceptable Mach number and dynamic pressure constraints required to open the parachute, and this event must occur at a sufficient altitude for the 'Skycrane' landing sequence to occur.

4.2 SRP Activation Regime

The total pressure conservation of oblique shock cascades, and thus the drag coefficient, increases with Mach number as discussed in Section 3.2.2. This phenomenon allows SRP to decelerate the capsule earlier in the EDL timeline. However, there is a practical altitude limit to using SRP due to the exponentially decaying density of the atmosphere. While the value of C_D may be highest during the early part of the descent (due to

the high Mach number), the atmospheric density and thus the free stream dynamic pressure are low. To use drag-augmented SRP (as opposed to high-thrust SRP which eliminates drag) the thrust of the vehicle is assumed to be proportional to the dynamic pressure. As a result, the thrust and drag forces acting on the vehicle are small during the early portion of the EDL timeline. As the vehicle descends, the atmospheric density and dynamic pressure increase, thus increasing the total drag and thrust forces on the vehicle. As the vehicle continues to decelerate and descend, the free stream dynamic pressure begins to decrease due to the slower velocity of the capsule. This once again results in very little drag and thrust forces resulting from drag-augmented SRP operation. The effect of the dynamic pressure during the flight is shown in Figure 4.4.

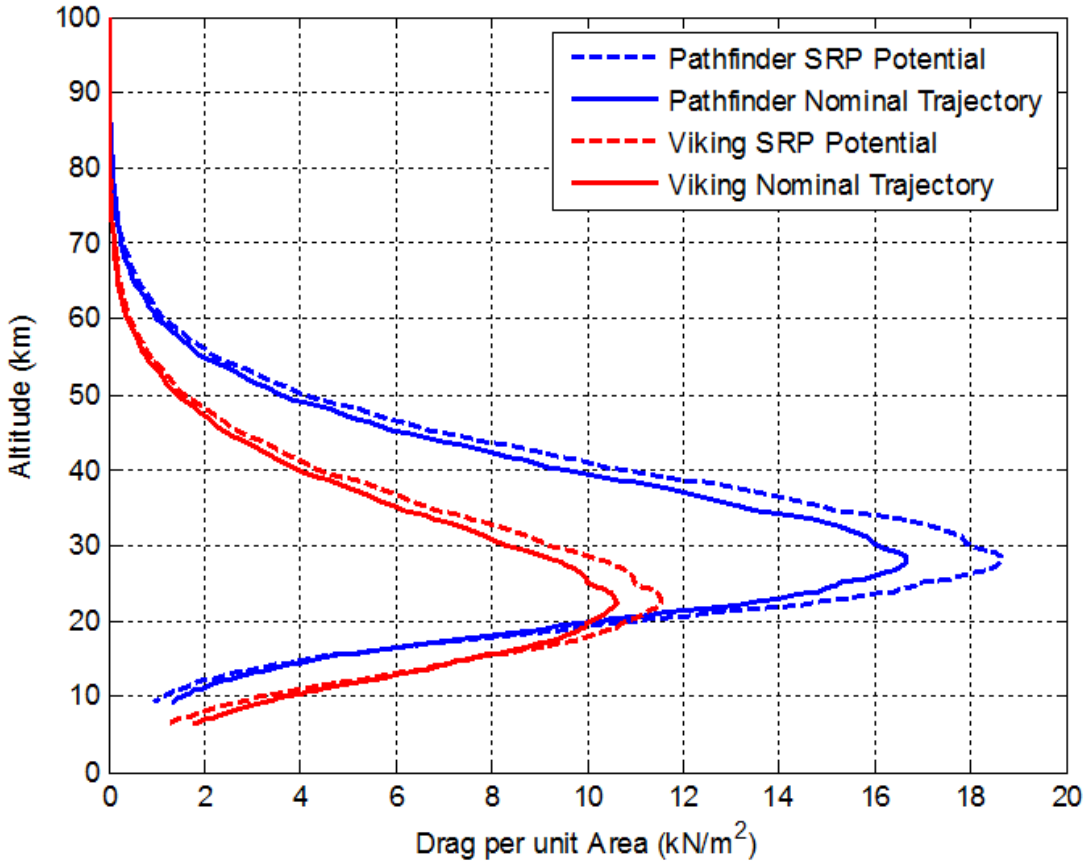

Figure 4.4: Drag augmentation capability for SRP

Figure 4.4 shows the drag force per unit area for the Viking and Pathfinder missions, representing direct insertion and entry from orbit trajectories. The SRP potential curves show how much drag force is possible if the SRP engines were to be turned on at that point in time. The plot does not include the amount of thrust required as a function of time, as it follows the same behavior of the nominal trajectory scaled by a factor of C_T/C_D. The maximum increase in drag occurs at the peak dynamic pressure as expected. This flight regime is somewhat dependent on the entry conditions; however peak dynamic pressure occurs in the 20-40 km altitude range. Since the SRP drag-augmentation is diminished outside of the region of maximum dynamic pressure, is it beneficial to limit the portions of the EDL trajectory when SRP is activated to reduce operational complexity.

It is also important to note that the drag augmentation is low at high altitudes, which corresponds to high Mach numbers. Recall from Section 3.3.5 that the drag model sensitivities were generally the largest at high Mach numbers. Since the actual dynamic pressure at the highest Mach numbers is low, even large sensitivity ranges will only result in a small change in the actual drag force.

Figure 4.5 shows the sensitivity of the maximum allowable mass at parachute deployment using drag-augmented SRP to the modeled drag coefficient from Chapter 3. The SRP is operated during the entire descent for this sensitivity study.

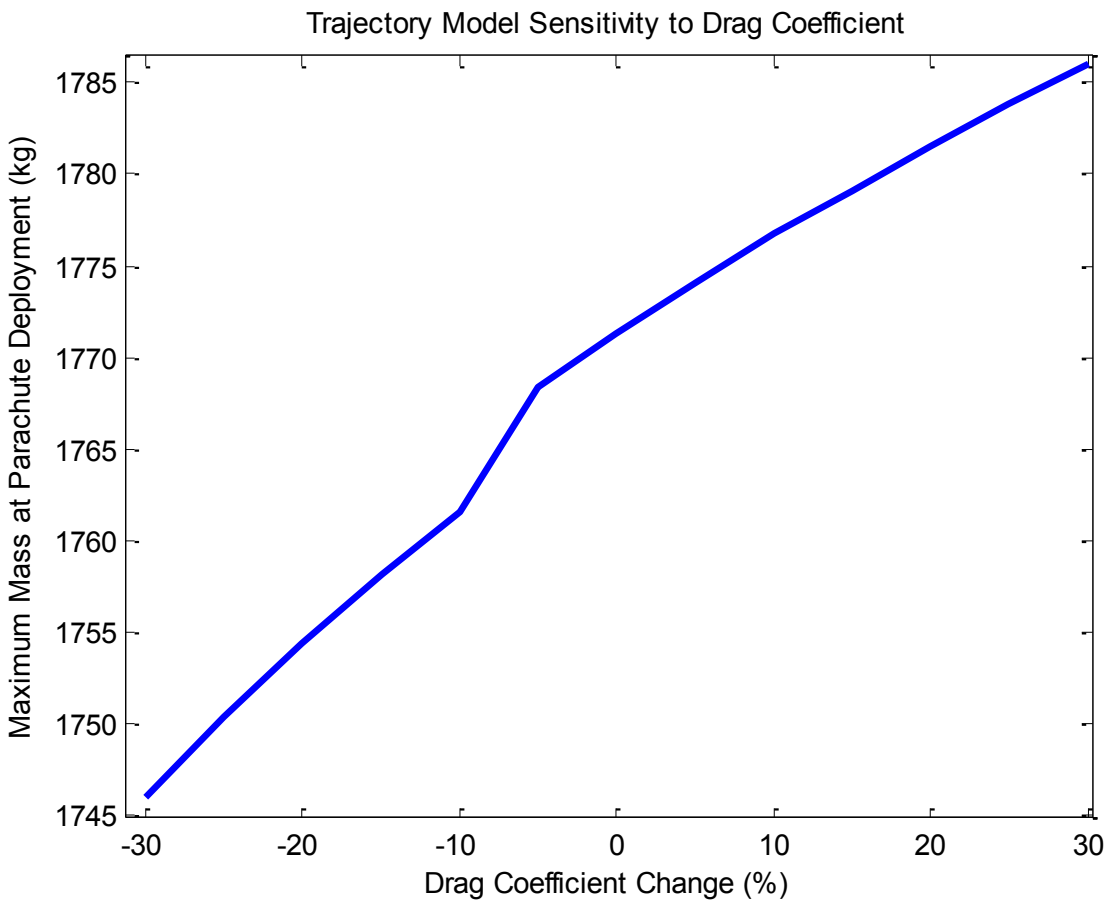

Figure 4.5: Sensitivity of mass at parachute deployment to drag coefficient model

The mass at parachute deployment is shown to not be sensitive to the drag coefficient within the uncertainty and sensitivity ranges observed in Sections 3.3.4 and 3.3.5, as the entry mass changes by less than 2% for +/- 30% variation in the drag coefficient. This result suggests that the exact value of the drag coefficient is not critical, so long as the drag is not eliminated. The increase in mass performance is a result of the total axial force, which is a function of both the thrust coefficient and the drag coefficient. As a result, the uncertainty in the drag model is diminished by the combination of the drag and thrust forces.

To examine the full space of the SRP activation regime, a variety of thrust profiles were examined. The thrust profiles were set based upon an operation 'duration' (the change

in of altitude during which the SRP is operated) and a termination altitude (when the SRP is turned off). The SRP is assumed to be operated at the maximum drag-augmentation level (as modeled in Chapter 3) with perfect engine throttling at a thrust coefficient of 1.0. MATLAB's `fzero` root finding algorithm is implemented to find the maximum entry mass that results in meeting the parachute deployment conditions as described in Section 4.1.3 at an altitude of 10 km. The entry conditions are based on the MSL aeroshell size, velocity, and flight path angle from Refs. [1] and [9]. The MSL mission represents the maximum amount of mass that has been landed on Mars, and so using these initial conditions quantify the increase in landed mass possible using drag-augmented SRP. However, MSL utilized an offset angle of attack during EDL to produce lift, thereby increasing range and the mass of payload that could be landed. MSL also flew an active hypersonic and supersonic control system, and so the lift and drag coefficients produced by the vehicle were not constant during EDL. Without knowing the time history of these parameters, the MSL trajectory cannot be fully reconstructed. Instead, the baseline trajectory used for comparison is a vehicle with the same entry conditions and aeroshell size as MSL, but with the maximum mass that meets the landing conditions for a ballistic entry (1335 kg). Figure 4.6 shows the maximum entry mass that meets the required parachute deployment conditions for various SRP thrust intervals.

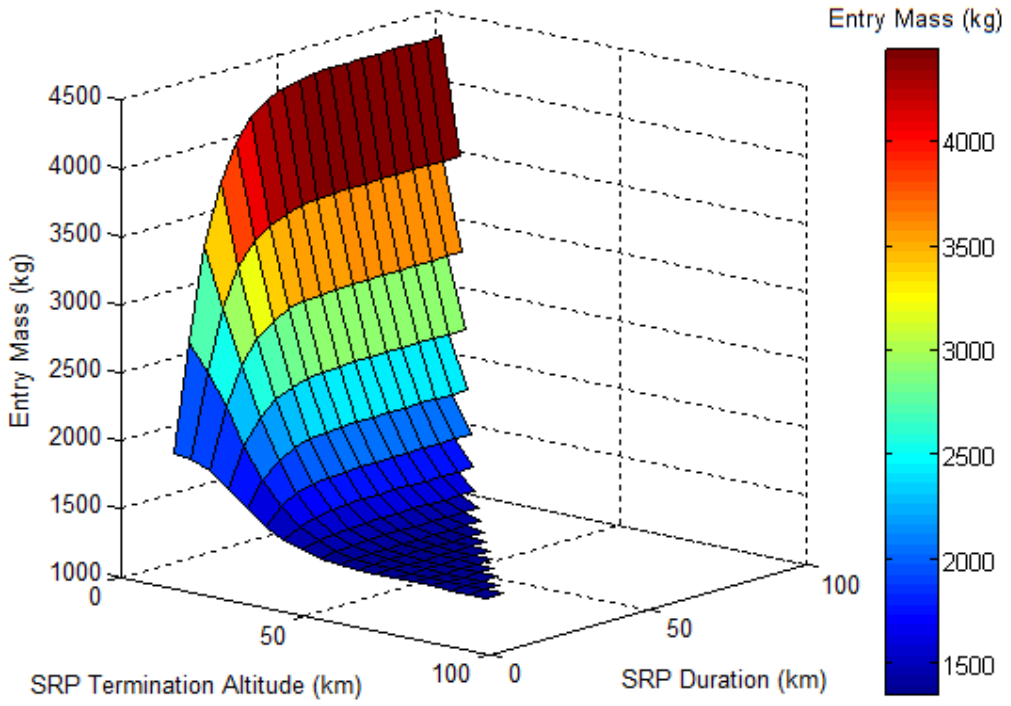

Figure 4.6: Maximum entry vehicle mass using drag-augmented SRP

The results in Figure 4.6 were obtained using only drag-augmentation levels of SRP thrust (a thrust coefficient of 1.0). The maximum entry mass results when the SRP is operated throughout the entire descent. This entry mass is 4433 kg, a 232% increase from the baseline ballistic entry mass. However, operating the SRP engines for a sizeable portion of the descent requires a significant amount of propellant. The propellant mass used for the various SRP operation profiles is shown in Figure 4.7.

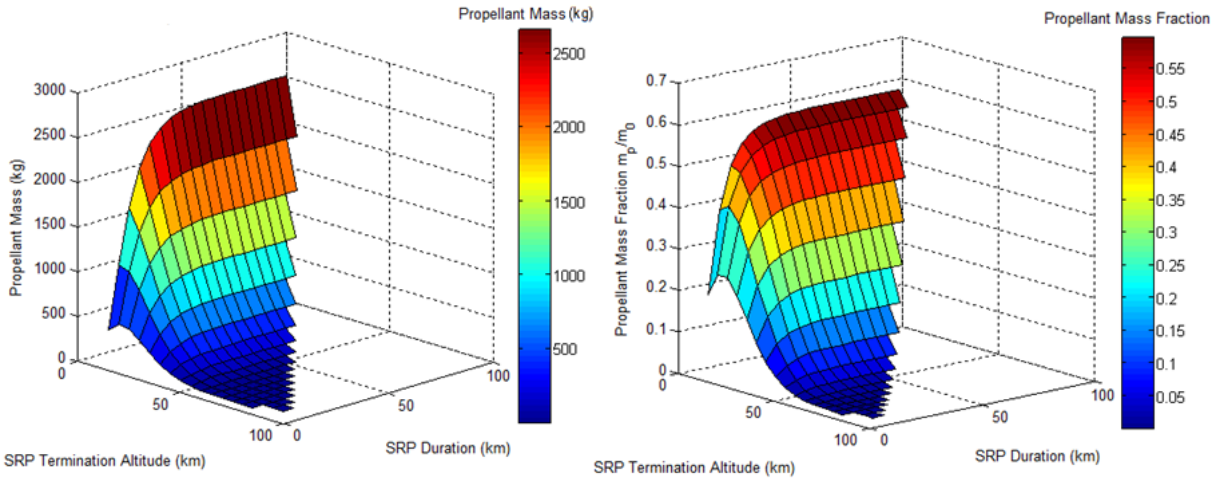

(a) Propellant mass (b) Propellant mass fraction

Figure 4.7: SRP propellant mass results

The propellant mass used follows a similar trend as the entry mass results in Figure 4.6. The highest propellant mass requirements occur for profiles operating through the largest dynamic pressure region since the thrust level is proportional to the dynamic pressure. For small thrust durations, the maximum propellant mass peaks for termination altitudes near 15-20 km. When the SRP duration is increased further it will necessarily encompass the maximum dynamic pressure region, and so the maximum propellant mass consumed occurs for profiles terminating at 10 km (the parachute deployment altitude).

Increasing the propellant mass required is an undesirable consequence of using SRP systems since the propellant mass could otherwise be used for payload mass or to decrease the launch mass, representing a decrease in mass efficiency of the EDL system. However, the primary metric of concern is the amount of payload that can be landed. The payload mass is strongly dependent in part on the performance of the parachute and landing system. Analysis of this part of the EDL system is out of the scope of this work, but since all the results in this section use the same parachute deployment conditions, the mass of the parachute and landing

hardware can be assumed to remain constant. The payload mass of the vehicle for each case would be obtained by a constant offset if the mass of the parachute and landing hardware were known. Thus the results for vehicle mass at parachute deployment will be very similar to the payload mass if the full EDL sequence was simulated. The mass of the vehicle at parachute deployment is shown in Figure 4.8.

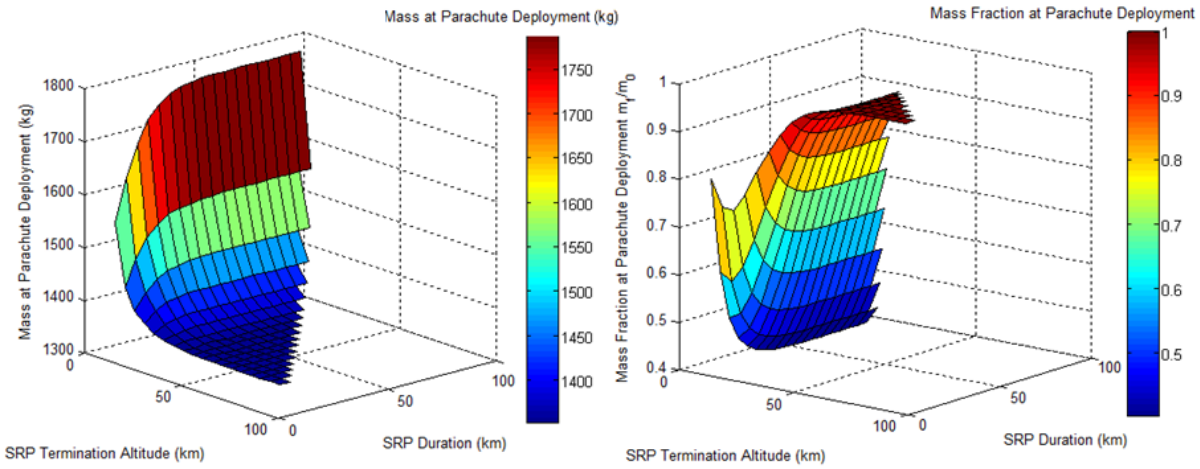

(a) Mass at parachute deployment (b) Mass fraction at parachute deployment

Figure 4.8: Maximum vehicle mass at parachute deployment

For the cases when the SRP is operated at high altitude, the mass at parachute deployment is approximately the same as the entry mass (which is the ballistic entry reference mass). The mass at parachute deployment increases as the SRP is operated in the maximum dynamic pressure region. The maximum mass at parachute deployment attainable is 1786 kg, which is an increase of 451 kg (a 34% increase over the baseline). However, since the hardware mass required for the parachute, aeroshell, landing system, etc. is assumed to remain approximately constant, the increase of 451 kg can be committed to the payload of the vehicle (once the required SRP hardware such as propellant tanks and engines is subtracted), resulting in a much larger percentage increase.

It is interesting to note that the maximum mass at parachute deployment always occurs for a termination altitude of 10 km (the altitude of parachute deployment) for a given operation duration. Due to the increasing propellant mass, the mass fraction of the vehicle at parachute deployment (equivalent to the vehicle's dry mass fraction) shown in Figure 4.8 (b) is generally the smallest for these thrust profiles. The dry mass fraction decreases as the mass at parachute deployment increases since the propellant mass consumed is increasing at a larger rate. While this trend is not desirable, it does maximize the amount of payload that can be landed.

Further insight into the SRP operation design space can be seen in the additional views in Figure 4.9.

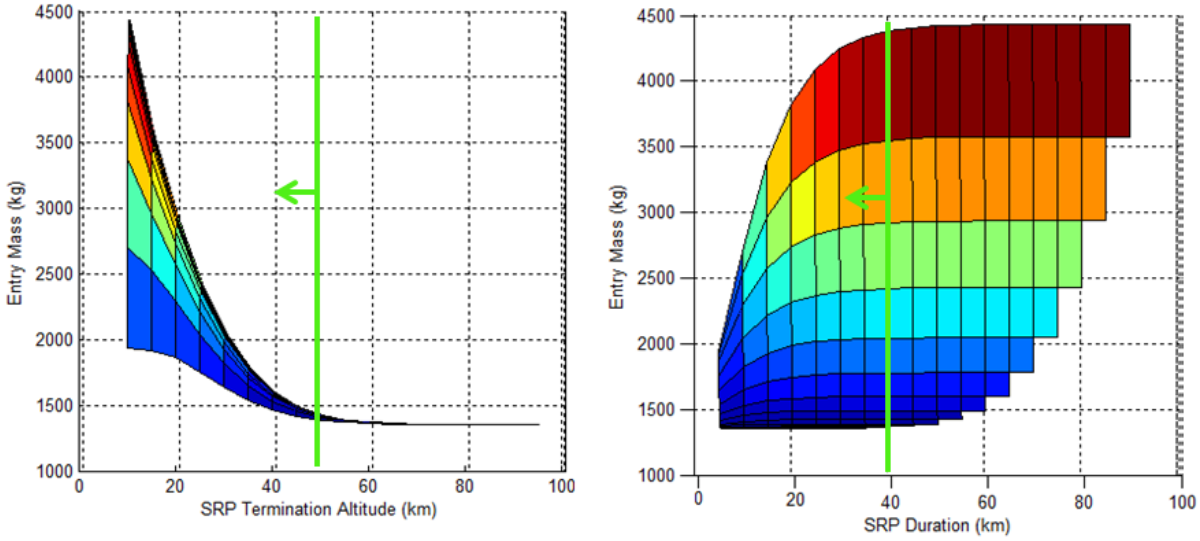

(a) Entry mass vs. termination altitude (b) Entry mass vs. duration

Figure 4.9: Behavior of SRP entry mass design space

Figure 4.9 (a) shows that the entry mass is largely unaffected when the SRP is operated solely above 40 km. This follows from Figure 4.4 because the dynamic pressure at these altitudes is very small. As a result, the drag force, thrust, and mass consumption

resulting from the SRP is small. The entry mass increases as the termination altitude decreases for all SRP operation durations.

Figure 4.9 (b) shows that increasing the duration that the SRP system is operated increases the allowable entry mass, provided the termination altitude is sufficiently low. This is because the longer operation effectively reduces the ballistic coefficient of the vehicle for a longer period, resulting in greater deceleration. However, this only applies up to a certain altitude, where the effect of SRP operation is negligible. This is once again due to the low dynamic pressure of the flow during high altitudes. Operating the SRP system between altitudes of 10 km and 50 km allows 98.8% of the entry mass for SRP operation between 10 km and 100 km (a difference of 51 kg). This focuses the concept of operations for SRP to altitudes between 10 and 50 km.

4.2.1 Maximum Acceleration Limitations

Operating the SRP system at peak dynamic pressure will result in an increase in the maximum axial acceleration experienced by the vehicle during descent. This is simply because the maximum axial force is increased with SRP. While robotic missions can be designed to withstand higher structural loading and peak heating rates from the higher deceleration (at the expense of adding structural mass), crewed missions will have strict limits on peak deceleration during EDL. This is a result of crew safety which is hindered by atrophied health from the weightless cruise to Mars. To decrease the peak deceleration of EDL, the magnitude of the entry path angle can be decreased to create a shallower trajectory through the atmosphere. However, this change in the trajectory results in a longer flight time which increases the total heat load the thermal protection system must be able to absorb. The heating environment for the aeroshell while using SRP has not been examined in detail, and

is out of the scope of this thesis. To analyze the impact of acceleration constraints, the flight path angle is decreased incrementally until the maximum acceleration threshold is not exceeded (numerically solving for the precise flight path angle that results in the maximum acceleration equaling the limit results in a stiff and computationally time-consuming problem due to the discontinuities in the problem space). The resulting entry mass and vehicle mass at parachute deployment for the acceleration limited trajectories are shown in Figure 4.10. The maximum deceleration was limited to 15 Earth g's (147.15 m/s^2), which was based off the peak deceleration observed during the Pathfinder entry data.

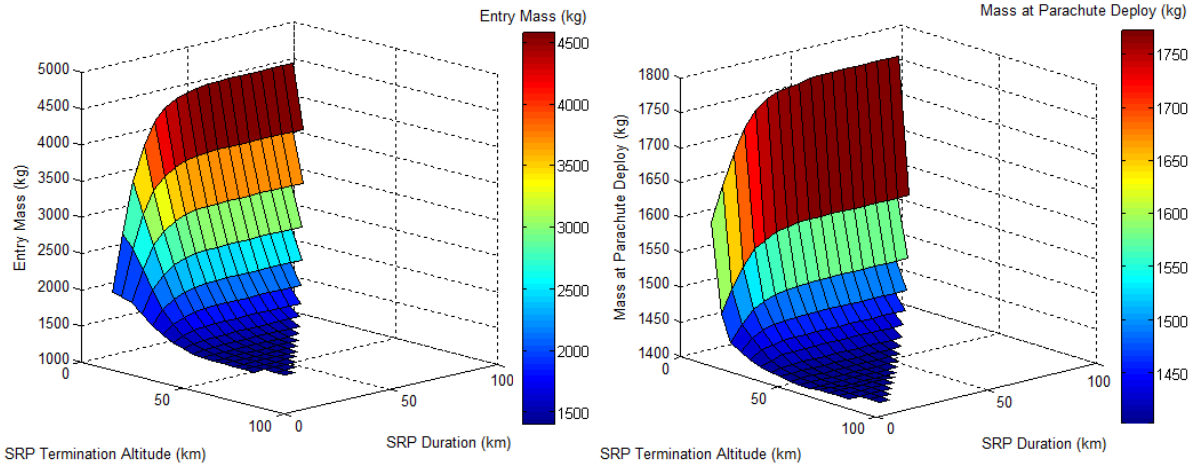

(a) Entry mass (b) Mass at parachute deployment

Figure 4.10: SRP entry and final masses for acceleration constrained trajectories

The maximum possible entry mass and mass at parachute deployment increases when the acceleration constraints are taken into account. This is because the magnitude of the entry flight path angle is decreased to lower the peak acceleration during descent, which results in a longer flight time. The longer flight time allows for a larger amount of mass to be decelerated before reaching the 10 km parachute deployment altitude. While this is a beneficial result for increasing the mass capability of SRP systems, it ignores the thermal heating limitations of entry. Increasing the total flight time also increases the total amount of

heat energy that is absorbed into the vehicle, or heat 'soak'. Since the aerothermodynamics of SRP flows is unknown, analysis of the thermal environment and required thermal protection systems is outside of the scope of this work. A longer flight time will also increase the uncertainty in landing at a desired location due to a longer flight time and traveled distance. The thermal and landing uncertainty components represent significant limitations that must be considered in EDL analysis to properly design the entry flight path angle. This problem will be constrained in further analyses in this chapter by assuming the MSL entry flight path angle of -14.5° which is within the range of previous landed missions.

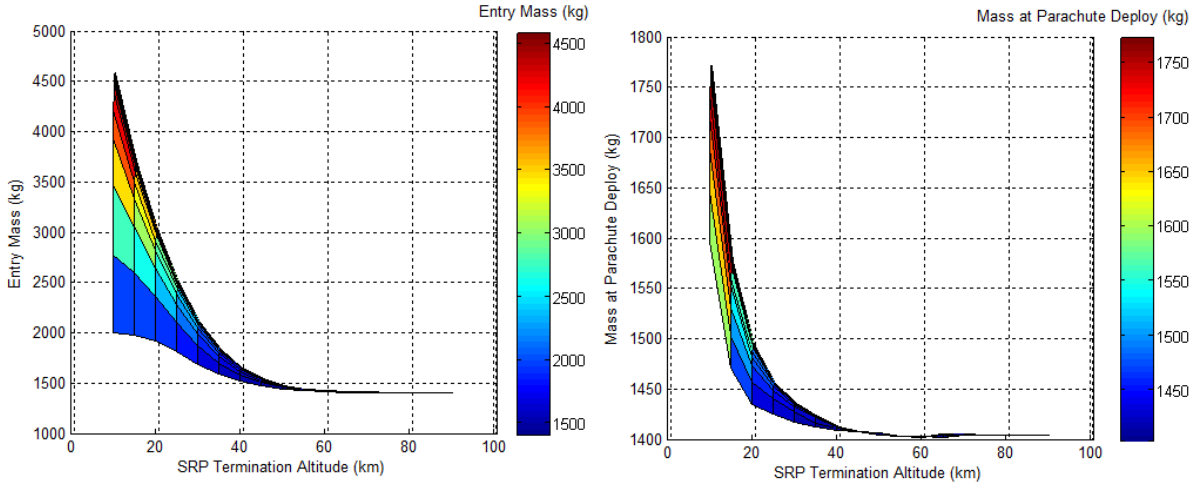

(a) Entry mass (b) Mass at parachute deployment

Figure 4.11: Termination altitude impacts on acceleration constrained trajectories

One interesting result of the acceleration constrained trajectories was that the mass at parachute deployment was unaffected for termination altitudes above approximately 30 km, as shown in Figure 4.11(b). The entry mass shown in Figure 4.11(a) was unaffected for termination altitudes above 50 km which is the same trend observed for the trajectories unconstrained by the peak acceleration. However, the mass at parachute deployment is unaffected above termination altitudes above 30 km in the acceleration constrained case.

4.2.2 Engine Throttling Constraints

Another important consideration for selecting the activation regime for SRP systems is the thrust range the engine must be able to provide. The dynamic pressure ranges from a negligible level at entry to a maximum on the order of kilopascals. Assuming a thrust coefficient of 1 for a MSL-size aeroshell, this means that an engine would have to be capable of throttling from 0 Newtons to hundreds of kilonewtons to operate ideally throughout the EDL timeline. This is not a feasible operation scenario for practical engine systems. It is possible to throttle rocket engines to a limited extent. The desired rocket engine concept of operation for drag-augmented SRP would match its peak thrust level to the maximum dynamic pressure range, and then throttle down around that point in the timeline to the extent possible, depending on the particular engine design. If the engines cannot be throttled, it is desirable to set the thrust to match a thrust coefficient of 1 at the maximum dynamic pressure. As the vehicle passes through this region and the dynamic pressure decreases, the set level of thrust will correspond to higher thrust coefficients. This provides drag-augmentation over the largest time frame during descent. Figure 4.12 shows the maximum allowable entry mass for constant-thrust SRP operation.

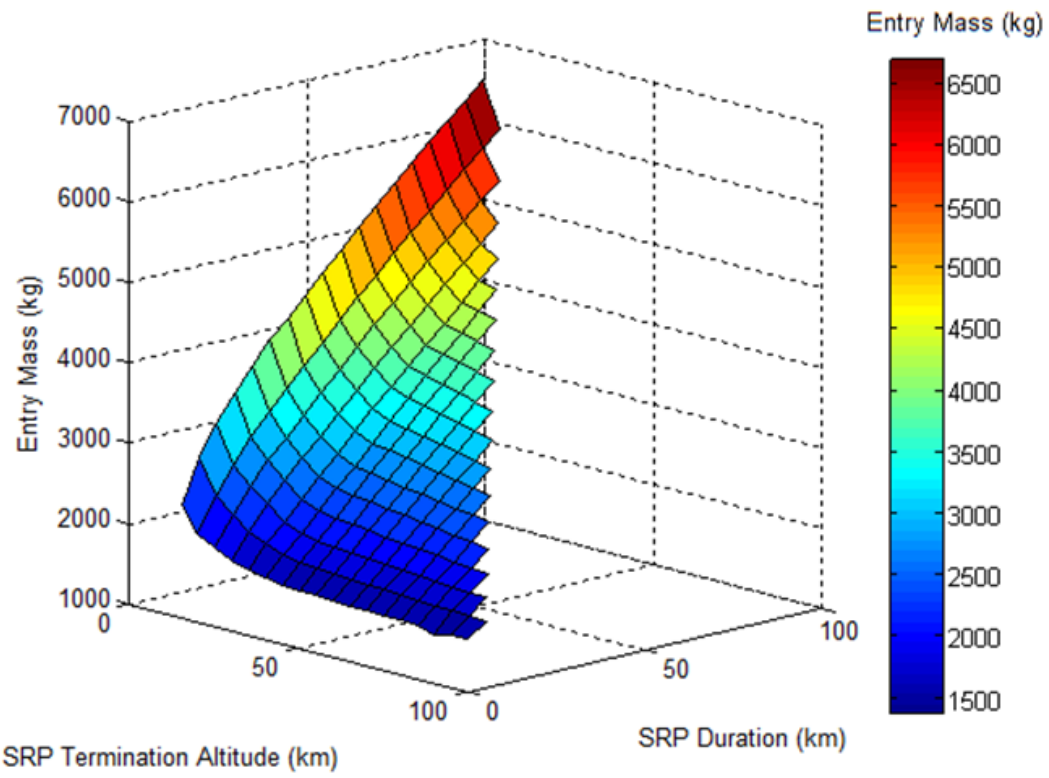

Figure 4.12: Entry vehicle mass for constant thrust SRP operation

The thrust is tuned to match a thrust coefficient of 1.0 at peak dynamic pressure, resulting in a total of approximately 100 kN of thrust (divided evenly between all 4 nozzles). The results in Figure 4.12 resembles the solution for a perfectly throttled engine (Figure 4.6), except that the entry mass increases approximately linearly as the operation duration increases since the time duration of the thrust operation is increasing. However, the solution for the mass at payload deployment shown in Figure 4.13 is significantly different between the two cases.

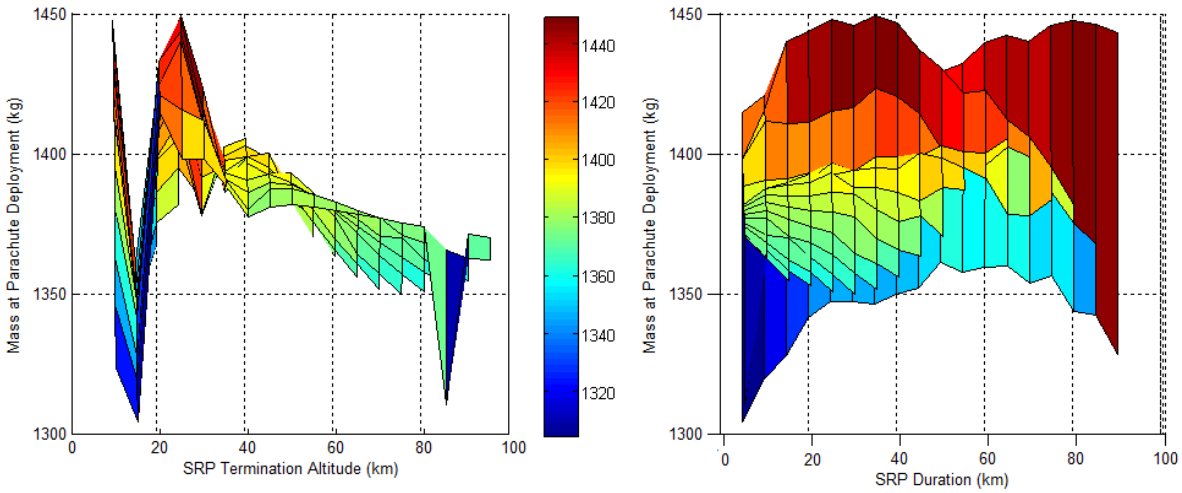

(a) (b)

Figure 4.13: Vehicle mass at parachute deployment for constant thrust SRP operation

There are two interesting characteristics to the results shown in Figure 4.13. The first is the abrupt drop-off in dry mass for termination altitudes near 15 km. This is a result of the thrust coefficient only slightly exceeding 1.5. The aerodynamic-propulsive models in literature indicate that the drag augmentation is eliminated for thrust coefficients above 1.5. The trajectory model assumes the following models for drag as a function of thrust coefficient:

Table 4.3: Drag model for various thrust coefficients

Thrust Level	$0 \leq C_T < 1.0$	$1.0 \leq C_T \leq 1.5$	$C_T > 1.5$
Drag Model	Nominal capsule drag	Drag augmentation model (Chapter 3)	Drag eliminated

If the thrust coefficient just exceeds 1.5, the total axial force coefficient is equal to only the thrust coefficient (1.5). However, if the thrust coefficient is slightly below 1.5 the drag is augmented, and the total axial force coefficient is the sum of the drag and thrust coefficients (approximately 3.0-3.25). The trajectories terminating SRP at 15 km result in the thrust coefficient exceeding 1.5 during the period of large dynamic pressure, which in turn

decreases the maximum dry mass of the vehicle. While the change is abrupt, the actual difference in payload mass is small (less than 10% decrease in dry mass).

The other important result from Figure 4.13 is that the maximum mass occurs for two different operation modes: constant thrust operation through the entire descent and operation focused about the region of maximum dynamic pressure. The maximum dry mass of 1450 kg can be obtained for SRP termination at 25 km and SRP operation 'durations' of 20-40 km. This matches the peak dynamic pressure region observed in Figure 4.4. While both methods can permit a dry mass of approximately 1450 kg, the propellant mass required for the operation at peak dynamic pressure is 65% lower than the propellant required for SRP duration throughout SRP (a decrease of 3407 kg of propellant). This result illustrates how focusing SRP operation at the region of maximum dynamic pressure can drastically reduce the entry vehicle mass. This capability may enable larger mass missions which otherwise would be too heavy to be launched to Mars.

4.3 Combination Decelerator Systems

Since the drag coefficient using drag-augmented SRP increases with Mach number, it is most advantageous to use this technology at high Mach numbers and at peak dynamic pressure. However, the drag-augmented methodology of SRP deceleration has been shown to be less capable than other supersonic decelerators such as IADs in terms of the maximum possible landed mass. This section will investigate two methodologies of combining supersonic decelerator systems into hybrid systems to take advantage of the strengths of two decelerator systems.

4.3.1 Drag-Augmented SRP and High-Thrust SRP Hybrid

The use of drag-augmented SRP is more efficient than high-thrust SRP from a propellant mass standpoint. This is because drag-augmented SRP is able to use the atmosphere to decelerate the vehicle through drag in addition to the thrust force, whereas drag is eliminated for high-thrust SRP operation. These two operation concepts can be combined to make use of drag-augmented SRP's relative efficiency when the vehicle is passing through the region of maximum dynamic pressure and the high-thrust SRP's total deceleration capability during regions of lower dynamic pressure.

Figure 4.14 shows the results of using drag-augmented SRP beginning at 60 km, and then transitioning to high-thrust SRP at various altitudes which is operated until the parachute deployment at 10 km. Figure 4.15 shows the results of using high-thrust SRP beginning at 60 km and transitioning to drag-augmented SRP. These plots show results for four thrust levels.

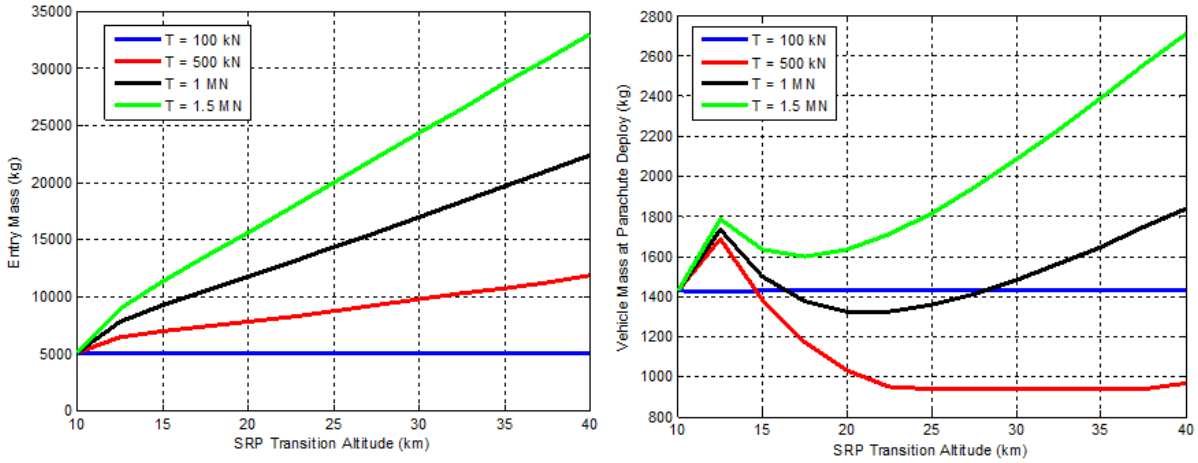

(a) Entry mass (b) Mass at parachute deployment

Figure 4.14: Vehicle mass capability for drag-augmented to high-thrust SRP operation

Figure 4.14 shows that using a combination of SRP methods will increase the vehicle entry mass. The dry mass of the vehicle (equivalent to the mass at parachute deployment,

which is the entry mass minus the propellant mass) increases initially for the highest thrust engines, and then the mass for all thrust levels decrease to a minimum before increasing once again as the transition altitude is increased. The initial increase is due to the low dynamic pressure. This results in low SRP thrust and drag forces while the thrust coefficient for the high-thrust SRP more than makes up for the loss of drag and increased propellant consumption. As the transition altitude continues to increase into the region of maximum dynamic pressure, the thrust coefficient of the high-thrust SRP is not enough to make up for the increased propellant consumption and loss of drag, which decreases the total vehicle mass capability. As the transition altitude continues to increase towards the point at which the descent is mostly using high-thrust SRP, the total impulse provided by the high-thrust engines compensates for the loss of drag force. However, the entry mass of the vehicle for this scenario is significantly greater than for the hybrid operating mostly with drag-augmented SRP. This effect is similar to the observations made for the constant-thrust profiles in Section 4.2.2.

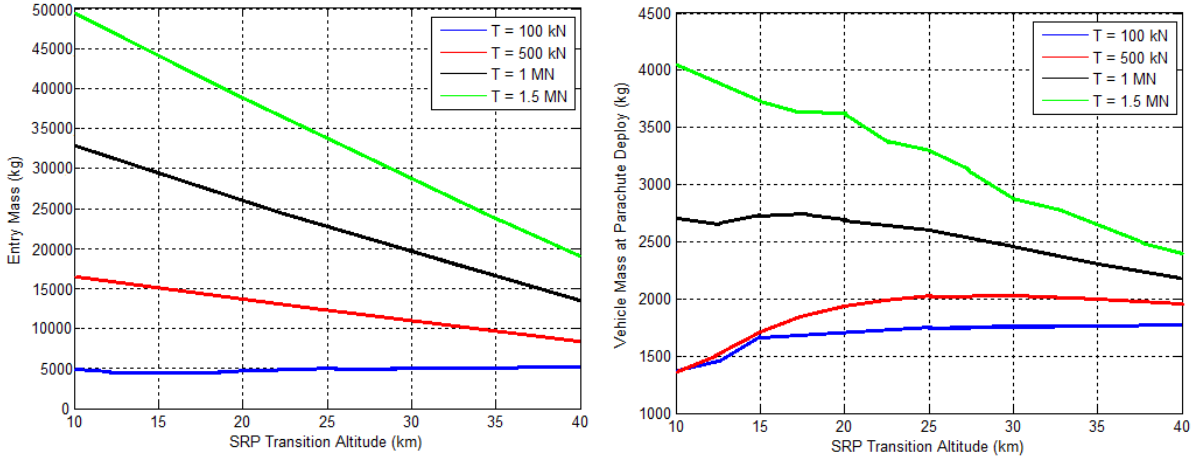

(a) Entry mass (b) Mass at parachute deployment

Figure 4.15: Vehicle mass capability for high-thrust to drag-augmented SRP operation

Figure 4.15 shows the results for a SRP hybrid where the SRP transitions from high-thrust to low-thrust. The vehicle dry masses are larger for this scenario, since the high-thrust operation will consume propellant mass earlier in the EDL timeline which reduces the ballistic coefficient for a longer portion of descent. The use of high-thrust SRP first slows the vehicle earlier in the descent timeline which decreases the dynamic pressure for SRP operation, which in turn decreases the total force available. As a result, the allowable dry mass at higher transition altitudes decreases for the two highest thrust cases. However, the maximum vehicle dry mass for these two cases is higher than the maximum dry mass results when the reverse operation scenarios (Figure 4.14).

4.3.2 Drag-Augmented SRP and IAD Hybrid

IAD systems can provide larger ballistic coefficients than drag-augmented SRP systems while requiring less mass for the decelerator system, as illustrated in Section 3.1.1. However, there are other advantages to using drag-augmented SRP over IADs. The dynamic stability and controllability of IAD systems has not been extensively characterized. These potentially limit the flight regimes in which IADs can be used safely and without degrading the accuracy of landing site predictions. In addition, supersonic IAD systems are limited by their deployment envelope for structural and thermal reasons. Like the disk-gap-band parachute, IAD systems can only be deployed under certain dynamic pressure and Mach number thresholds. For these reasons, it is advantageous to use drag-augmented SRP systems at higher altitudes where the dynamic pressure and Mach numbers are higher (and where drag-augmented SRP is the most effective), and then deploy an IAD at lower altitudes. Operation of SRP at higher altitudes also can potentially provide active trajectory guidance to

improve the landing site accuracy. The results for the mass capabilities of a SRP and IAD hybrid system with four IAD diameter options are shown in Figure 4.16.

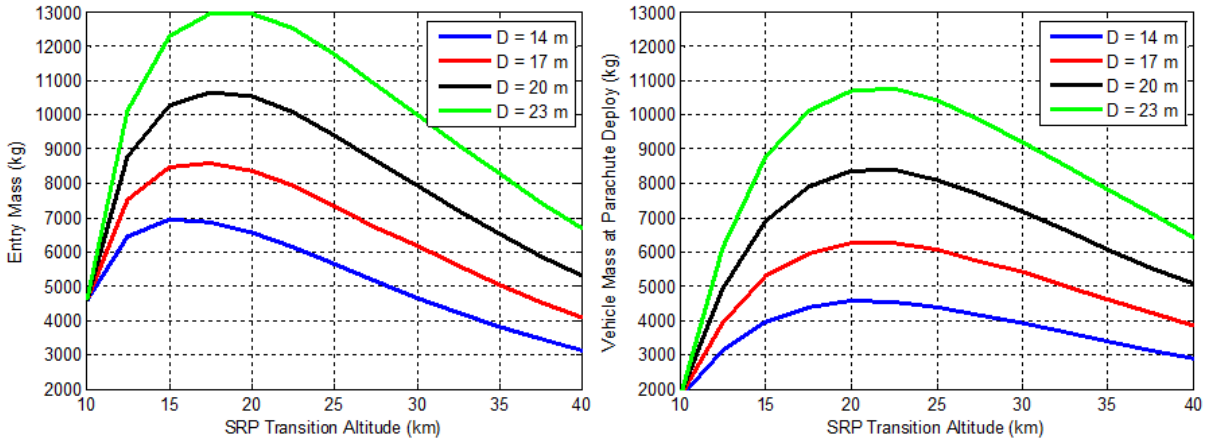

(a) Entry mass (b) Mass at parachute deployment

Figure 4.16: Vehicle mass capability for drag-augmented SRP and IAD hybrid method

The results in Figure 4.16 show a maximum entry mass for IAD deployment altitudes between 15 and 20 km, while the maximum dry mass occurs between approximately 20 and 23 km. The maximum dry mass (defined in this case as the entry mass minus propellant mass and IAD system mass) is 10770 kg for a 23 meter diameter tension-cone IAD, which is a 708% increase (9435 kg) over the reference vehicle. This increase in mass is significantly greater than for methods only using drag-augmented SRP. The resulting maximum mass is also greater than IAD-only options. The maximum mass at parachute deployment occurs for drag-augmented SRP operating through the region of maximum dynamic pressure. The IAD then deploys at lower velocities (though the dynamic pressure is still significant) and the resulting increased drag area continues to slow the vehicle.

The entry mass increases by 11612 kg for the SRP-IAD hybrid (a factor of 8.7 times more massive than the reference trajectory vehicle). This entry mass is a fraction of the entry mass using the SRP hybrid option discussed in Section 4.3.1. However, the dry mass fraction

for the SRP-IAD hybrid design is significantly higher since the propellant usage is much lower. The dry mass fraction for the SRP-IAD hybrid is 83% for the scenario providing the maximum dry mass, while the dry mass fraction for the SRP hybrid solution is approximately 8%. For the drag-augmented only scenario, the dry mass fraction for the maximum mass case is less than 40%. This demonstrates both the significant increase in EDL vehicle mass that the SRP-IAD hybrid can facilitate as well as the increase in efficiency of the decelerator systems.

These results demonstrate the utility of a hybrid decelerator system composed of drag-augmented SRP and a tension cone IAD. The hybrid solution not only provides significantly increased dry mass capability, but it addresses potential weaknesses with IAD systems such as the deployment envelope and control authority. While this option presents strong performance, the use of two supersonic decelerator systems present significant risk and development cost to an EDL mission. IADs and SRP have minimal testing histories in flight conditions. Both technologies have significant operational risks which must be addressed through future research and development. The combination of these two systems would only compound the operational complexity. To develop one technology or the other alone for a Mars EDL mission will require a significant investment; to invest in a combination of both technologies would likely be infeasible.

4.4 Summary

This chapter performed several analyses of Mars entry and descent trajectories using drag-augmented SRP. A 3 degree of freedom trajectory model was validated against data reconstructed from the Mars Pathfinder mission. The drag model developed in Chapter 3 was integrated into the trajectory model to characterize the maximum entry mass and mass at

parachute deployment that drag-augmented SRP can support. The trajectory model was shown to have a low sensitivity to the value of the modeled drag coefficient, which indicates that the model developed in Chapter 3 is sufficient to provide relevant results in this chapter. Drag-augmented SRP was found to be most effective in the region of peak dynamic pressure, between 20 and 40 km in altitude.

The first study performed computed the maximum entry mass and vehicle mass at parachute deployment (equivalent to the EDL vehicle's dry mass and closely related to the vehicle's payload mass) for various SRP thrust intervals. The termination altitude and altitude intervals for SRP operation were varied across the design space and both the maximum entry mass vehicle dry mass were found to occur when the SRP was operated throughout the entire descent. The entry mass increased by 331% over the reference trajectory and the corresponding vehicle dry mass increased by 34%. The increase in vehicle mass is usable for additional payload mass once the required SRP hardware and propellant tanks have been incorporated into the vehicle. Since the dynamic pressure at high altitudes is low and SRP has little effect in this regime, operating the SRP below altitudes of 50 km delivers 98.8% of the vehicle dry mass provided by the entirely propulsive solution.

Constraints due to peak acceleration during descent and non-throttling engines were examined. The SRP operation design space performs similarly for acceleration constrained flight trajectories as for non-constrained trajectories, with the maximum vehicle masses occurring for constant SRP operation. The vehicle mass increases as the entry flight path angle decreases; however this is not desirable from thermal and landing accuracy considerations. The results for constant-thrust engines shows a maximum vehicle dry mass for two operation scenarios: continuous SRP operation throughout the entire descent and SRP

operation focused on the region of maximum dynamic pressure. While both options provide approximately the same vehicle mass to the point of parachute deployment, the latter requires 65% less propellant mass to achieve.

Two hybrid supersonic decelerator concepts were also analyzed. The first was a combination of SRP operation methodologies: low-thrust SRP that augments the aerodynamic drag, and high-thrust SRP which eliminates drag. The high- and low-thrust SRP hybrids demonstrated increased mass capability due mainly to high-thrust SRP operation. There is a minimum dry mass solution for a given thrust level which occurs for low-thrust SRP transitioning to high-thrust SRP. This minimum result is a function of the loss in aerodynamic drag and the increase in propellant consumption as a result of the SRP operation transition.

A hybrid SRP and IAD solution was also examined. This solution significantly increased the vehicle's dry mass (by over 700%) while also achieving a dry mass fraction of 83% by consuming significantly less propellant. The hybrid solution achieves a maximum dry mass for IAD deployment altitudes between 20 and 23 km. This allows the drag-augmented SRP to operate through the region of maximum dynamic pressure. The IAD is deployed at lower altitudes where the velocity is lower, which results in less stringent requirements for the IAD's thermal and structural design. While this option significantly increases operational complexity by using two new forms of supersonic decelerators, there is a significant potential to increase the payload mass capability of EDL vehicles.

5 CONCLUSION

The development of new and more capable robotic and potential crewed missions to Mars will require the development of new entry, descent, and landing technologies to safely land high-mass payloads. The state-of-the-art Mars Science Laboratory still relies on Viking-era technology for entry and descent. The mass limit for such technologies is being approached, and as a result new decelerator technologies must be developed.

Current research has investigated the application of additional decelerators in the hypersonic and supersonic phases of descent. Supersonic retropropulsion uses rocket engines directed into the oncoming flow to decelerate the vehicle. Previous research has been performed to characterize the systems level applicability of high thrust operation of SRP during EDL. In addition, limited wind tunnel testing and CFD simulations have been performed to analyze the flow physics for the SRP aerodynamic-interactions. When operated at the proper thrust levels and flow conditions, vehicles with SRP nozzles placed at the periphery of the aeroshell have been shown to increase the aerodynamic drag force in addition to providing a thrust force. This operation methodology provides increased deceleration forces without increasing propellant consumption.

5.1 Contributions

The major contributions of this thesis are:

Aerodynamic Modeling

- IAD systems demonstrated to provide lower ballistic coefficient than SRP systems.
- Drag coefficient model developed for drag-augmented SRP.

- Performed validation of drag model to within 10% of CFD and test data in literature.
- Performed sensitivity analysis of drag model input parameters.

Trajectory Modeling

- Ideally throttled drag-augmented SRP increases vehicle mass at parachute deployment.
    - Largest mass at parachute deployment obtained with SRP operation through entire descent, resulting in 34% increase over baseline vehicle.
- Operation in maximum dynamic pressure regime critical to efficacy.
    - Results in 65% reduction in propellant mass with constant-thrust operation.
- Hybrid decelerator systems take advantage of appropriate flight regimes.
    - SRP hybrid system increases total vehicle mass but requires larger propellant mass fraction.
    - SRP-IAD hybrid increases mass at parachute deployment by 708% over baseline vehicle with a propellant mass fraction of 17%.

Drag-augmented supersonic retropropulsion is dependent on the complex aerodynamic-propulsive interactions between the free stream flow around an entry vehicle and the rocket exhaust plumes of the SRP system. The SRP operation space has only been partially explored with a combination of wind tunnel testing and CFD simulations. However, these research methods are time and labor intensive, and thus not suited for use in conceptual system design studies over a wide range of operation parameters.

To address the need for data outside of the current peripheral-nozzle data sets published in literature, a drag model was created. This model combines results from CFD simulations in literature with quasi-one-dimensional flow to estimate the drag coefficient of a 70° sphere-cone aeroshell as a function of free stream Mach number. The model assumes 0°

angle of attack and flow symmetry in any 90° quadrant. This model can be run in a matter of minutes for all relevant flight Mach numbers to estimate the performance of the drag-augmented SRP system. While this model must neglect a significant amount of flow physics, it is shown to capture the dominant flow mechanisms resulting in the increased aerodynamic drag acting on the vehicle. The drag coefficient for peripheral-nozzle SRP flows was found to increase the drag coefficient over the nominal drag coefficient of a 70° sphere-cone aeroshell by 14% at high Mach numbers. However, for Mach numbers less than 6, the SRP drag coefficient is lower than the nominal aeroshell drag coefficient. The drag coefficient was compared to CFD and wind tunnel simulations and shown to match the available data to within 10% for the relevant free stream Mach numbers.

The drag model was also explored to determine sensitivity to the parameters set from CFD results. Since the drag preservation effects of the oblique shock cascades increase with the free stream Mach numbers, model was shown to be most sensitive to the input parameters from CFD results at high Mach numbers. However, at high Mach numbers and altitudes, the dynamic pressure on the vehicle is low due to the low atmospheric density. Therefore, the impact of the model sensitivity is diminished in this regime. The drag model was found to be most sensitive to the oblique shock wave angle and the size of the flow region passing through the oblique-normal shock cascade. However, a good level of agreement between the model presented in this work and the data available in literature suggests that the model captures the dominant physics of SRP flow, and the parameters set from CFD results were well set to provide accurate results over a range of Mach numbers.

A 3 degree of freedom entry trajectory model was created to analyze the impacts of drag-augmented SRP for Mars EDL. The model simulates the flight of an EDL vehicle from

entry until parachute deployment, which occurs at the same conditions as the Mars Science Laboratory mission requirements. The flight is ballistic as the SRP system is assumed to produce no lift in the modeled configuration. This trajectory model was validated against data reconstructed from the Mars Pathfinder mission.

The SRP drag model was incorporated into the entry trajectory model to study the increase in entry and payload mass from using SRP. An analysis of the maximum entry mass as a function of the SRP operation altitude and the termination altitude was performed to determine the best regime of applicability for the technology. The maximum entry mass and mass at parachute deployment was obtained for continuous SRP operation throughout the descent. The vehicle mass at payload deployment (which is composed of the payload mass and the non-consumable EDL hardware such as the aeroshell and landing equipment) was increased by 451 kg, which is a 34% increase over the reference ballistic trajectory. Drag-augmented SRP operation above 50 km was shown to have a negligible impact, contributing less than 2% to the increase in vehicle mass.

A constant-thrust scenario was also analyzed. The results show that focusing SRP operation on the region of maximum dynamic pressure results in the same increase in vehicle dry mass as SRP operation throughout the entire descent while requiring 65% less propellant. A hybrid SRP method involving both high-and low-thrust SRP was demonstrated to behave conceptually similar to the constant-thrust results and provided increased dry mass. The increase in dry mass was predominantly due to the high thrust level and operation duration compared to the variable-thrust SRP scenario.

The final design analyzed was a hybrid system using drag-augmented SRP and a tension cone IAD. The resulting system was able to provide vehicle dry masses that are

708% larger than the baseline vehicle. This solution also achieved a dry mass fraction of 83%, since significantly less propellant is consumed than the high-thrust SRP options. The hybrid solution achieves a maximum dry mass for IAD deployment altitudes between 20 and 23 km. This operation allows the SRP system to operate earlier in the EDL timeline, where IAD deployment is limited by thermal and structural constraints. The IAD can then deploy at lower altitudes, where the resulting larger drag area increases the total drag force on the vehicle without consuming propellant. Although this hybrid system presents significantly increased operational complexity over a single type of supersonic decelerator, it does provide the ability to considerably increase the payload mass that can be landed on Mars.

5.2 Further Work

The recommendations for future work on this topic are:

SRP Modeling

- Expand SRP aerodynamics database through wind tunnel testing or CFD.
- Analytic or semi-analytic modeling of SRP shock structure.
- Correlation of drag coefficient with thrust coefficient across relevant Mach numbers.
- Angle-of-attack model development
- Asymmetric thrust operation model development

Systems Analysis

- Sensitivity to additional performance parameters (C_T, I_{sp}, angle of attack, entry conditions, aeroshell size, etc.)
- Maneuvering flight and landing uncertainty analysis
- Conceptual vehicle design (aeroshell design, thermal environment, hardware system selection, component sizing, etc.)

The drag model developed in this study approximated the highly complex aerodynamic-propulsive flow interactions through quasi-1D flow relations and parameters estimated from CFD results. While this model matched the available data in literature for peripheral-nozzle SRP flows, it is limited to modeling the change in drag coefficient as a function of Mach number only. The SRP design space is much larger, and a drag model would ideally be able to characterize the vehicle's drag coefficient continuously for varying many relevant parameters such as the thrust coefficient, angle of attack, asymmetric thrust operation, etc. Such a model could be created by greatly extending the test conditions for wind tunnel experiments and/or CFD simulations to cover the entire design space. This would create an aerodynamic database for SRP flows, similar to the databases collected for the 70° sphere cone aeroshell vehicles. However, such an effort would likely require significant investments of labor and facilities.

The model developed in this thesis could be expanded to predict the shock structure in front of the vehicle to increase the utility of the model. With knowledge of the shock structure, the pressure distribution on the aeroshell face can be better determined. The shock structure can also be used to determine the changes in behavior for changes in angle of attack, thrust operation, etc. In addition, the thermal environment for the aeroshell is an important model to create to estimate the thermal protection system requirements. If the shock structure can be reasonably approximated through a combination of analytic methods and parameters set from CFD results, the full SRP design space can be explored much more quickly and at a lower cost than full CFD or wind tunnel testing.

The trajectory analyses performed in this thesis present a general overview of the impacts of various operation concepts for drag-augmented SRP. The analyses performed can

be extended to study the effects of the SRP flow field parameters discussed above, such as the thrust coefficient. Once models have been created for SRP flows at angle of attack or under asymmetric engine thrust levels, a full 6 degree of freedom trajectory model could be employed to analyze maneuvering flight during EDL and the landing uncertainty ellipse.

The vehicle data used in the trajectory analyses was kept constant to study the effect of SRP operation. Future work on the EDL vehicle design would include studies on the specific SRP hardware, such as propellant types and available rocket engines, and sizing of the relevant hardware, such as propellant tanks and the required structure mass and aeroshell size. This work would apply further practical design constraints to research and development efforts. In addition, the entry parameters were not varied. The entry flight path angle and velocity can be varied to examine direct entry, entry from orbit, and aerobraking concepts. These entry conditions will also have impacts on the thermal protection system design and the landing site uncertainty.

The design space for entry, descent, and landing vehicles is very large with a myriad of parameters contributing to the vehicle's performance. The work presented in thesis has developed aerodynamic models suited for conceptual EDL analysis and identified several regions of best applicability for SRP systems. The future work on SRP systems must be focused on the systems-level, conceptual design of EDL vehicles to bound the most promising design spaces. Future work must also be done to study the detailed physics relevant to SRP flows so that the performance of such vehicles can be accurately predicted across the relevant design spaces. The combination of these two efforts will develop SRP systems and increase the readiness level of the technology for test flights and future use on entry, descent, and landing vehicles.

REFERENCES

[1] A. D. Stelzner, P. D. Burkhart,, A. Chen, K. A. Comeaux, C. S. Guernsey, D. M. Kipp, L. V. Lorenzoni, G. F. Mendeck, R. W. Powell, T. P. Rivellini, A. M. San Martin, S. W. Sell, R. Prakash and D. W. Way, "Mars Science Laboratory Entry, Descent, and Landing System Overview," *International Planetary Probe Workshop*, Barcelona, 2010.

[2] "National Space Science Data Center," Goddard Spaceflight Center, 3 July 2012. http://nssdc.gsfc.nasa.gov/image/spacecraft/mars3_lander_vsm.jpg. [Accessed 30 11 2012].

[3] "Solar System Exploration Multimedia," Jet Propulsion Laboratory, 29 November 2011. http://solarsystem.nasa.gov/multimedia/display.cfm?IM_ID=244. [Accessed 30 11 2012].

[4] K. T. Edquist, A. A. Dyakonov, M. J. Wright and T. Y. Chun, "Aerothermodynamic Environments Definition for the Mars Science Laboratory Entry Capsule," *45th AIAA Aerospace Sciences Meeting and Exhibit Meeting*, AIAA Paper 2007-1206, Reno, 2007.

[5] R. Braun and R. Manning, "Mars Exploration Entry, Descent and Landing Challenges," *AIAA Journal of Spacecraft and Rockets,* Vol. 44, No. 2, pp. 310-323, 2007.

[6] C. Davies and M. Arcadi, "Planetary Mission Entry Vehicles Quick Reference Guide, Version 3.0," NASA Center for Aerospace Information, Hanover.

[7] M. R. Grover III, B. D. Cichy and P. N. Desai, "Overview of the Phoenix Entry, Descent and Landing System Architecture," *AIAA/AAS Astrodynamics Specialist Conference and Exhibit*, AIAA Paper 2008-7218, Honolulu, 2008.

[8] P. N. Desai, J. L. Prince, E. M. Queen, J. R. Cruz and M. R. Grover, "Entry, Descent, and Landing Performance of the Mars Phoenix Lander," *AIAA/AAS Astrodynamics Specialist Conference and Exhibit*, AIAA Paper 2008-7346, Honolulu, 2008.

[9] C. D. Karlgaard, P. Kutty, M. Schoenenberger, J. Shidner and M. Munk, "Mars Entry Atmospheric Data System Trajectory Reconstruction Algorithms and Flight Results," *51st AIAA Aerospace Sciences Meeting including the New Horizons Forum and Aerospace Exposition*, AIAA Paper 2013-0028, Grapevine, 2013.

[10] M. K. Lockwood, "Introduction: Mars Science Laboratory: The Next Generation of Mars Landers," *Journal of Spacecraft and Rockets,* vol. 43, no. 2, p. 257, 2006.

[11] A. D. Cianciolo, J. L. Davis, J. D. Shidner and R. W. Powell, "Entry, Descent and Landing Systems Analysis: Exploration Class Simulation Overview and Results," *AIAA/AAS Astrodynamics Specialist Conference*, AIAA Paper 2010-7970, Toronto, 2010.

[12] I. Clark, A. Hutchings, C. Tanner and R. Braun, "Supersonic Inflatable Aerodynamic Decelerators For Use On Future Robotic Missions to Mars," *IEEE Aerospace Conference*, IEEEAC Paper 1419, Big Sky, 2008.

[13] M. Adler, M. Wright, I. Clark, W. Engelund and T. Rivellini, "Entry, Descent, and Landing Roadmap," National Aeronautics and Space Administration, 2012.

[14] T. A. Zang, A. M. Dwyer Cianciolo, M. C. Ivanov, R. R. Sostaric and D. J. Kinney, "Overview of the NASA Entry, Descent and Landing Systems Analysis Studies for Large Robotic-class Missions," *AIAA SPACE 2011 Conference & Exposition*, AIAA Paper 2011-7294, Long Beach, 2011.

[15] P. O. Jarvinen and R. H. Adams, "The Aerodynamic Characteristics of Large Angled Cones with Retrorockets," National Aeronautics and Space Administration, NASA Contract No. NAS7-576, Cambridge, 1970.

[16] A. M. Korzun and R. D. Braun, "Performance Characterization of Supersonic Retropropulsion for Application to High Mass Mars Entry, Descent, and Landing," *AIAA Atmospheric Flight Mechanics Conference*, AIAA Paper 2009-5613, Chicago, 2009.

[17] A. M. Korzun, J. R. Cruz and R. D. Braun, "A Survey of Supersonic Retropropulsion Technology for Mars Entry, Descent, and Landing," *AIAA Journal of Spacecraft and Rockets,* Vol. 46, No. 5, pp. 929-937, 2009.

[18] C. L. Marsh and R. D. Braun, "Fully-Propulsive Mars Atmospheric Transit Strategies for High-Mass Payload Missions," *IEEE Aerospace Conference*, IEEEAC Paper 1219, Big Sky, 2009.

[19] N. M. Bakhtian and M. J. Aftosmis, "Parametric Study of Peripheral Nozzle Configurations for Supersonic Retropropulsion," *AIAA Journal of Spacecraft and Rockets,* Vol. 47, No. 6, pp. 935-950, 2010.

[20] N. M. Bakhtian and M. J. Aftosmis, "Maximum Attainable Drag Limits for Atmospheric Entry via Supersonic Retropropulsion," *8th International Planetary Probe Workshop*, Portsmouth, 2011.

[21] N. M. Bakhtian and M. J. Aftosmis, "Analysis of Inviscid Simulations for the Study of Supersonic Retropropulsion," *29th AIAA Applied Aerodynamics Conference*, AIAA Paper 2011-3194, Honolulu, 2011.

[22] B. Kleb, D. G. Schauerhamer, K. Trumble, E. Sozer, M. Barnhardt, J.-R. Carlson and K. Edquist, "Toward Supersonic Retropropulsion CFD Validation," *42nd AIAA Thermophysics Conference*, AIAA Paper 2011-3490, Honolulu, 2011.

[23] J. R. Codoni, E. M. Reed, J. C. McDaniel, H. Alkandry and I. D. Boyd, "Investigations of Peripheral 4-jet Sonic and Supersonic Propulsive Deceleration Jets on a Mars Science Laboratory Aeroshell," *49th AIAA Aerospace Sciences Meeting*, AIAA Paper 2011-1036, Orlando, 2011.

[24] A. M. Korzun, "Aerodynamic and Performance Characterization of Supersonic Retropropulsion for Application to Planetary Entry and Descent," Ph.D. Dissertation, School of Aerospace Engineering, Georgia Institute of Technology, Atlanta, 2012.

[25] D. G. Schauerhamer and K. A. Trumble, "Continuing Validation of Computational Fluid

Dynamics For Supersonic Retropropulsion," *50th AIAA Aerospace Sciences Meeting*, AIAA Paper 2012-0864, Nashville, 2012.

[26] K. A. Zarchi, D. G. Schauerhamer, W. Kleb, J.-R. Carlson and K. Edquist, "Computational Fluid Dynamics Validation and Post-test Analysis of Supersonic Retropropulsion in the Ames 9×7 Unitary Tunnel," *42nd AIAA Fluid Dynamics Conference and Exhibit*, AIAA Paper 2012-2705, New Orleans, 2012.

[27] B. P. Smith, C. L. Tanner, M. Mahzari, I. G. Clark, R. D. Braun and F. M. Cheatwood, "A Historical Review of Inflatable Aerodynamic Decelerator Technology Development," in *IEEE Aerospace Conference*, IEEEAC Paper 1276, Big Sky, 2010.

[28] I. G. Clark, "Aerodynamic Design, Analysis, and Validation of a Supersonic Inflatable Decelerator," Ph.D. Dissertation, School of Aerospace Engineering, Georgia Institute of Technology, Atlanta, 2009.

[29] L. M. Bermudez and K. M. Langone, "Parametric Characterization of the Embedded Shock Phenomenon in Tension Cone Inflatable Aerodynamic Decelerators," *21st AIAA Aerodynamic Decelerator Systems Technology Conference and Seminar*, AIAA Paper 2011-2581, Dublin, 2011.

[30] I. G. Clark, A. L. Hutchings, C. L. Tanner and R. D. Braun, "Supersonic Inflatable Aerodynamic Decelerators For Use On Future Robotic Missions to Mars," in *IEEE Aerospace Conference*, IEEEAC Paper 1419, Big Sky, 2008.

[31] V. Gidzak, I. Nompelis, G. Candler and K. Stein, "Flow Simulation of a Tension Cone Inflatable Aeroshell with Fluid-Structure Interaction," *48th AIAA Aerospace Sciences Meeting*, AIAA Paper 2010-506, Orlando, 2010.

[32] S. J. Hughes, F. M. Cheatwood, R. A. Dillman, H. S. Wright, J. A. DelCorso and A. M. Calomino, "Hypersonic Inflatable Aerodynamic Decelerator (HIAD) Technology Development Overview," *21st AIAA Aerodynamic Decelerator Systems Technology Conference and Seminar*, AIAA Paper 2011-2524, Dublin, 2011.

[33] M. K. McGuire, J. O. Arnold, M. A. Covington and I. C. Dupzyk, "Flexible Ablative Thermal Protection Sizing on Inflatable Aerodynamic Decelerator for Human Mars Entry Descent and Landing," *49th AIAA Aerospace Sciences Meeting*, AIAA Paper 2011-344, Orlando, 2011.

[34] F. Baginski and K. Brakke, "Deployment Analysis of Pneumatic Envelopes Including Ascending Balloons and Inflatable Aerodynamic Decelerators," *AIAA Journal of Spacecraft and Rockets,* vol. 49, no. 2, pp. 413-421, 2012.

[35] J. A. Christian, G. Wells, J. Lafleur, A. Verges and R. D. Braun, "Extension of Traditional Entry, Descent, and Landing Technologies for Human Mars Exploration," *AIAA Journal of Spacecraft and Rockets,* vol. 45, no. 1, pp. 130-141, 2008.

[36] A. M. Kuethe and C.-Y. Chow, Foundations of Aerodynamics, New York: John Wiley & Sons, Inc., 1998.

[37] P. K. Kundu and I. M. Cohen, Fluid Mechanics, Oxford: Elsevier, 2008.

[38] J. H. Keenan and J. Kaye, Gas Tables, New York: John Wiley & Sons, Inc., 1948.

[39] B. Edney, "Anomalous Heat Transfer and Pressure Distributions on Blunt Bodies at Hypersonic Speeds in the Presence of an Impinging Shock," The Aeronautical Research Institute of Sweeden, Stockholm, 1968.

[40] J. J. Bertin, Hypersonic Aerothermodynamics, Washington: American Institute of Aeronautics and Astronautics, 1994.

[41] P. Wells and P. Thornley, "Blunt Cone Pressure Correlations for Supersonic and Hypersonic Flow," *AIAA 14th Applied Aerodynamics Conference*, AIAA-96-2447-CP, New Orleans, 1996.

[42] C. B. Moyer, L. W. Anderson and T. J. Dahm, "A Coupled Computer Code for the Transient Thermal Response and Ablation for Non-Charring Heat Shields and Nose Tips," NASA CR-1630, Aerotherm Corporation, Mountain View, 1970.

[43] F. J. Regan and S. M. Anandakrishnan, Dynamics of Atmospheric Re-Entry, Washington: American Institute of Aeronautics and Astronautics, 1993.

[44] NASA Space Environments and Effects Program, *Mars Global Reference Atmospheric Model,* Software Package, 2010 v1.0, National Aeronautics and Space Administration, Marshall, AL, 2010.

[45] D. A. Spencer, R. C. Blanchard, R. D. Braun, P. H. Kallemeyn and S. W. Thurman, "Mars Pathfinder Entry, Descent, and Landing Reconstruction," *AIAA Journal of Spacecraft and Rockets,* vol. 36, no. 3, pp. 357-366, 1999.

[46] National Aeronautics and Space Administration, "Mars Atmosphere Model," Glenn Research Center, 8 September 2010. http://www.grc.nasa.gov/WWW/k-12/airplane/atmosmrm.html. [Accessed 21 10 2012].

[47] K. T. Edquist, P. N. Desai and M. Schoenenberger, "Aerodynamics for Mars Phoenix Entry Capsule," *AIAA Journal of Spacecraft and Rockets,* vol. 48, no. 5, pp. 713-726, 2011.

APPENDIX A – ISENTROPIC RELATIONS

The isentropic equations are derived from the energy equation [36], where the subscript *0* indicates stagnation properties and *C* is a constant:

$$\frac{T}{\rho^{\gamma-1}} = C_1 \tag{A.1}$$

$$\frac{P}{\rho^{\gamma}} = C_2 \tag{A.2}$$

$$\frac{T}{P^{\frac{\gamma-1}{\gamma}}} = C_3 \tag{A.3}$$

Relations between static and stagnation temperature:

$$\frac{T_0}{T} = 1 + \frac{\gamma - 1}{2} M^2 \tag{A.4}$$

The isentropic flow relations (Eqn. A.1-A.3) can then be used to obtain similar relations for pressure and density:

$$\frac{P_0}{P} = \left(\frac{T_0}{T}\right)^{\frac{\gamma}{\gamma-1}} = \left[1 + \frac{\gamma - 1}{2} M^2\right]^{\frac{\gamma}{\gamma-1}} \tag{A.5}$$

$$\frac{\rho_0}{\rho} = \left(\frac{T_0}{T}\right)^{\frac{1}{\gamma-1}} = \left[1 + \frac{\gamma - 1}{2} M^2\right]^{\frac{1}{\gamma-1}} \tag{A.6}$$

APPENDIX B – SHOCK WAVE RELATIONS

The Mach number of the normal flow component across a shock is:

$$M_n = M \sin \beta_w \tag{B.1}$$

The deflection angle θ describes the amount the flow is turned after moving through the shock. These parameters can be related by equating the tangential flow velocities [36]:

$$\theta_d = \beta_w - \tan^{-1}\left[\frac{1}{\sin\beta_w \cos\beta_w}\left(\frac{\gamma-1}{\gamma+1}\sin^2\beta_w + \frac{2}{\gamma+1}1/M_1^2\right)\right] \tag{B.2}$$

The continuity equation and velocity component relations can be used to derive the pressure ratio across any shock [36].

$$\frac{P_2}{P_1} = \frac{2\gamma}{\gamma+1}M_{1n}^2 - \frac{\gamma-1}{\gamma+1} \tag{B.3}$$

The density ratio across the shock is:

$$\frac{\rho_2}{\rho_1} = \frac{\frac{\gamma+1}{\gamma-1} + \frac{P_2}{P_1}}{1 + \frac{\gamma+1}{\gamma-1}\frac{P_2}{P_1}} \tag{B.4}$$

The temperature ratio can be simply calculated from the equation of state:

$$\frac{T_2}{T_1} = \frac{P_2}{P_1}\frac{\rho_1}{\rho_2} \tag{B.5}$$

By examining the flow velocity components normal to the shock wave, a relation for the normal Mach number behind the shock is obtained [36].

$$M_{2n} = \left[\frac{(\gamma-1)M_{1n}^2 + 2}{2\gamma M_{1n}^2 - (\gamma-1)}\right]^{1/2} \tag{B.6}$$